Real-time Signal Processing for Coherent Optical OFDM Systems

by

Simin Chen

Submitted in total fulfillment of

the requirements for the degree of

Doctor of Philosophy

Department of Electrical & Electronic Engineering

The University of Melbourne

Australia

March, 2011

Produced on acid-free paper

Abstract

Real-time Signal Processing for Coherent Optical OFDM Systems

by **Simin Chen**

The principle of Orthogonal Frequency-Division Multiplexing (OFDM) modulation has been proposed for several decades. OFDM technology has moved out of laboratories into practice in modern wireless communication systems since early 1990s. Recently, OFDM is applied to the optical domain, which has shown a multitude of benefits such as immunity to chromatic dispersion, polarization-mode dispersion and high spectral efficiency. However, most of these research works are conducted in off-line processing where only a limited length of received signal is sampled and processed. This is useful to verify signal processing algorithms, but does not allow long-term performance verification. To solve this problem, real-time experiments are imperative. In this thesis, we conduct experiments on real-time implementation of coherent optical OFDM (CO-OFDM) systems, demonstrate up to 110-Gb/s real-time reception for over 600-km standard single mode fibre (SSMF) transmission, and perform real-time I/Q imbalance calibration for CO-OFDM transmission.

We investigate the optimum design of real-time signal processing algorithms for both single-input single-output (SISO) and multiple-input multiple-output (MIMO) CO-OFDM receivers. By using high-speed Analog-to-Digital Convertors (ADCs), Field-Programmable Gate Arrays (FPGAs) and efficient OFDM signal processing at the receiver, we have achieved record data rates for both single-band and multi-band CO-OFDM transmissions. In particular, the first multi-gigabit real-time CO-OFDM reception at 3.1 Gb/s is successfully demonstrated. A 110-Gb/s multi-band real-time receiver after 400-ps Differential-Group-Delay (DGD) and 600-km transmission

through SSMF without optical dispersion compensation is also provided. Several experiments on real-time signal processing confirm the feasibility of applying CO-OFDM to practical communication applications.

We also carry out experiments to demonstrate the effect of hybrid in-phase/quadrature (I/Q) imbalance compensation for CO-OFDM transmission. Since direct up/down conversion is applied, I/Q imbalance at the transmitter and receiver need to be compensated. We demonstrate the effectiveness of the adopted compensation algorithms by applying them both in off-line and real-time experiments. They perform well under a wide range of conditions in the presence of carrier frequency offset. The hybrid scheme mitigates the transmitter and the receiver I/Q imbalance in optical OFDM transmission.

This is to certify that

(i) the thesis comprises only my original work,

(ii) due acknowledgement has been made in the text to all other material used,

(iii) the thesis is less than 100,000 words in length, exclusive of table, maps, bibliographies, appendices and footnotes.

Signature_____

Date_____

Declaration

I hereby declare that this thesis comprises only my original work. No material in this thesis has been previously published and written by another person, except where due reference is made in the text of the thesis. I further declare that this thesis contains no material which has been submitted for a degree or diploma or other qualifications at any other university. Finally, I declare that the thesis is less than 100,000 words in length, exclusive of tables, figures, bibliographies, appendices and footnotes.

Acknowledgments

The work illustrated in this thesis was conducted with the kind instruction, help and support from many people who I would express my thanks.

First, I would like to express my deepest appreciation to my supervisor Associate Professor William Shieh, and co-supervisor Professor Stan Skafidas for their high quality academic advices and direction, and for their generous help and constant support throughout my PhD study. I would also like to acknowledge Dr. Fred Buchali at Alcatel-Lucent Research and Innovation in Germany, for giving me the opportunity to undertake an internship and broaden the view of my research.

I am also grateful to the University of Melbourne and the Department of Electrical and Electronic Engineering for providing my PhD scholarships and internship travel expenses. I would like to extend thanks to my supervisor William Shieh for providing my conference expenditures, and to all the colleagues around me in the department for providing a friendly and entertaining work environment.

Specifically I would like to thank all my group members under the supervision of Associate Professor William Shieh. We had many productive and insightful discussions. I am grateful to Dr. Abdullah Al Amin for his guidance and helpful work. I appreciate the collaboration opportunity with Dr. Yan Tang, Dr. Qi Yang and Dr. Yiran Ma on several projects.

On a personal level, I appreciate my wife Jie Yang for her constant support in my life and research work. I am also indebted to my parents and parents-in-law for the support they provide me through my entire life. It is their love and encouragement that make my research interesting and meaningful.

Contents

List of Figures

List of Tables

Chapter 1

Introduction

1.1 Overview

The demand for high-capacity, long-haul communication systems is increasing. Annual global traffic is expected to exceed three-quarters of a zettabyte in three years [1]. To satisfy these requirements the communication channel must have a very low loss and wide bandwidth [2]. The optical fibre has been proven to be the most promising in many different types of available communication channels [3-4].

Optical communication systems became possible due to the development of low-loss silica fibre and efficient double-heterostructure semiconductor lasers in the 1970s. The earliest optical systems were operated at around 0.8-μm wavelength at a bit rate of 45 Mb/s and the optical signal was repeated every 10 km [5]. Operation wavelength was shifted to 1.3 μm by the end of the 1980s for the purpose of low dispersion requirements when the Single Mode Fibre (SMF) was introduced. The invention of EDFA operated at 1.5 μm led to rapid advances in Wavelength-Division Multiplexing (WDM) transmission systems. Nowadays, 100-Gb/s Dense WDM (DWDM) networks are being deployed [6]. A 69.1-Tb/s (432×171-Gb/s) transmission over 240-km low-loss and low-nonlinear Pure Silica Core Fibre (PSCF) and a 12.5-Tb/s (112×112-Gb/s) transmission over 9360 km large effective area fibre have been demonstrated in research laboratories [7-8].

Optical communication is generally categorized into single-carrier and multi-carrier systems. The single-carrier scheme is relatively “conventional” and has been the mainstay of the modulation format in optical communications for three decades. It uses one frequency to carry all the data. This scheme has the advantage of low signal Peak-to-Average Power Ratio (PAPR). However, as the signal data rate per channel rapidly reaches 100 Gb/s and beyond, the single-carrier signal is extremely sensitive

to the Chromatic Dispersion (CD), Polarization Mode Dispersion (PMD), and the imperfection of the electro-optic components. As a result, relying on pure optical dispersion compensation becomes more and more difficult and complicated.

Multi-Carrier Modulation (MCM) is a scheme of modulation in which transmitting data are divided into many lower rate parallel streams [9]. Orthogonal Frequency-Division Multiplexing (OFDM), a particular form of MCM with densely spaced subcarriers and overlapping spectra was patented in the U.S. in 1970 [10]. OFDM waveforms are chosen such that the mutual orthogonality is ensured even though subcarrier spectrums overlap. It is shown that such waveforms can be generated by using an Inverse Fast Fourier Transform (IFFT) at the transmitter and a Fast Fourier Transform (FFT) at the receiver, respectively [11-12]. For a long period of time after the invention of OFDM, the practicality of the concept appeared limited. Implementation of a real-time Fourier transform was too complex and cost-prohibitive. OFDM was not considered as a communication standard until the 1990s.

Coherent Optical OFDM (CO-OFDM) was first proposed in 2006 [13]. It combines the advantages of "coherent detection" and "OFDM modulation" and exhibits numerous advantages over traditional single-carrier systems that are critical for future high-speed fibre transmission systems. Firstly, it is robust to CD and PMD with the introduction of cyclic-prefix. Secondly, it possesses ease of channel equalization because the channel response can be equalized on a subcarrier basis. Thirdly, OFDM systems have high spectral efficiency due to subcarriers overlapping in the frequency domain. Another benefit of this scheme is that the required electrical bandwidth is reduced by using direct up/down conversion. This is attractive for high-speed transmission since increasing electrical bandwidth indicates increasing cost. Last but not least, OFDM is computation efficient as the OFDM signal can be modulated and demodulated by using high-efficient FFT and IFFT.

The real-time CO-OFDM system is critical to validate the CO-OFDM technique and establish a solid platform for evaluating the feasibility of the technique for practical implementation. To implement real-time CO-OFDM reception, highly complex and computationally intense signal processing algorithms must be performed

in real-time. Although OFDM has already been adopted widely in wired and wireless transmission systems, these systems operate at signal bit rates of several tens of Mb/s [14], which are approximately one thousand times lower than the target of optical OFDM. Thus, it is apparent that the real-time signal processing power of a CO-OFDM system must be three orders of magnitude higher compared to the existing OFDM-based electrical systems.

1.2 Thesis Motivation

As we mentioned earlier, CO-OFDM has emerged as an attractive modulation format for high-speed optical transparent networks and has been considered as an upgrade solution to 100-Gb/s systems. Optical OFDM experiments at 1-Tb/s or beyond have been demonstrated [7-8, 15-16]. However, the signal reception in those reports is processed off-line. In other words, during each measurement the OFDM signal is sampled by a high-speed Digital Storage Oscilloscope (DSO) and stored in memory or a hard drive. The data are then transported to a computer and analysed by software at a relatively slow pace. In this whole time span, only the signal during the sampling window is collected while the rest between sampling intervals is discarded. In addition, to implement this technology in practical application, OFDM signal processing algorithms should be implemented by Integrated Chips (ICs). From the two viewpoints, research on real-time implementation of CO-OFDM reception is necessary to bring this technology to practical applications.

Modern silicon technology has made real-time CO-OFDM signal processing feasible. The Analog-to-Digital Converter (ADC) is a critical component in OFDM communications. Since the OFDM signal is naturally analog, the first step is to convert it to a digital form by sampling it using an ADC, which turns the analog signal into a stream of numbers. In the CO-OFDM receiver, the efficiency and speed at which analog information can be converted to digital signals profoundly affects system architectures and their performance. Modern semiconductor process is able to produce high-speed 6-bit ADCs with sampling rates exceeding 20 Giga-Samples-per-

Second (GSa/s) [17-18].

Another key component of real-time CO-OFDM reception is the high-speed digital signal processor. Digital signal processing algorithms have long been run on standard computers, specialized processors called Digital Signal Processors (DSPs), or purpose-built hardware such as Application-Specific Integrated Circuits (ASICs). Today, there are advanced technologies used for digital signal processing including more powerful general purpose Field-Programmable Gate Arrays (FPGAs). Latest high-end DSP offers 10-GHz cumulative clock rate with peak 320-Giga-Multiply-Accumulate-operations-per-Second (GMACS) and 160-Giga-Floating-point-OPerations-per-Second (GFLOPS) of combined fixed- and floating-point performance on a single device [19]. With respect to ASIC, the fastest Graphics Processing Unit (GPU) has a theoretical peak performance of 1,200-GFLOPS in single precision calculations [20]. High-performance FPGA achieves more than 1,755-GMACS performance using embedded digital signal processing slices [21]. All of these devices are designed to maximize the throughput of on-chip data flows and eliminate the possibility of bottlenecks, which are suitable for the high data rate optical OFDM transmission systems.

Direct down-conversion architecture is widely used in coherent optical receivers since it eliminates the need of image rejection filters and significantly reduces the required electrical bandwidth. However, it has well-known disadvantages of in-phase (I) and quadrature (Q) imbalance, caused by unequal analog response of electrical/optical components between I- and Q-branch. Although many I/Q imbalance compensation algorithms have been studied in wireless OFDM transmissions, the application of I/Q imbalance compensation in optical OFDM has seldom been reported.

In Chapters 4 and 5 of this thesis we will focus on the analysis of hardware implementation of real-time CO-OFDM reception and its relevant signal processing algorithms. In Chapter 6, we will concentrate on the impact of I/Q imbalance and its compensation both in off-line processing mode and real-time mode.

1.2.1 Multi-gigabit Real-time CO-OFDM Reception

The rapid advancement in semiconductor technology has spurred growing interest on applying digital signal processing for optical communications. Recently, a 40-Gb/s coherent QPSK transceiver implemented in 90-nm CMOS ASICs has been demonstrated in real-time [22]. Compared with the single-carrier coherent QPSK modulation [22-23], the CO-OFDM system entails some unique signal processing in OFDM frame synchronization, channel estimation and phase estimation. It is thus imperative that CO-OFDM signal processing be implemented in real-time mode to verify its feasibility. ADC is one of the crucial devices for the OFDM real-time implementation. Currently, high-speed ADCs at multi-GSa/s are commercially available. After sampling, the data are transported into a digital signal processor through high-speed Input/Output (I/O) interfaces for real-time signal processing. The up-to-date digital signal processors have sufficient resource to process the digital signal in multiple parallel channels.

Single mode fibre in essence can be represented as a 2×2 Multiple-Input Multiple-Output (MIMO) channel, and some sort of polarization diversity, either transmit or receive diversity can be employed for practical implementation. In such a scheme the capacity of an optical system is doubled because the transmitted OFDM signal can be considered as polarization modulation or polarization multiplexing. As the impact of PMD is to simply rotate the signal polarization, it can be treated with channel estimation and constellation reconstruction. Therefore the doubling of the channel capacity will not be affected by PMD. In addition, due to the polarization-diversity receiver employed at the receiver end, the 2×2 MIMO scheme does not need polarization tracking. Introducing the MIMO scheme into the real-time CO-OFDM receiver is an attractive subject since the data throughput can be doubled without increasing the ADC sampling rate.

Because of the bandwidth limit of state-of-art silicon technology, it is difficult to improve data rate by simply increasing the sampling rate of ADC beyond 100 GSa/s [22]. To alleviate the bandwidth constraint of ADC, the concept of Orthogonal Band

Multiplexing (OBM) to divide the entire OFDM spectrum into multiple orthogonal bands is proposed. It has been demonstrated that one part of the OFDM spectrum can be carved out and detected at a fraction of the whole band [24-25]. These multiple OFDM bands with small or zero frequency guard band can be multiplexed and de-multiplexed without inter-band interference due to inter-band orthogonality.

Therefore, we are interested about the following questions relating to the real-time CO-OFDM reception:

- How to transplant the off-line signal processing algorithms to the real-time mode under the restrictions of complexity, speed and hardware cost?
- How much impact is caused by quantizing signal to a fixed-point format in a digital signal processor?

1.2.2 In-phase/Quadrature Imbalance Compensation

Direct-conversion architecture has been widely used in telecommunication because of its low complexity and cost [26]. Nevertheless, it introduces impairments such as I/Q imbalance and frequency offset, incurring severe degradation in communication performance. Estimation and compensation of the impairments in direct-conversion architecture has become a topic of extensive research works in the wireless domain [27-29]. However, only a few experiments have been reported for optical OFDM transmissions [30-32].

Owing to the overlapped spectrum, OFDM is vulnerable to Carrier Frequency Offset (CFO) which will cause severe performance degradation [33]. An effective compensation scheme which is robust to CFO is necessary for I/Q imbalance calibration.

Although a few I/Q imbalance compensation experiments in optical OFDM have been reported [30-32], they are all processed off-line and the algorithm complexity and hardware implementation are not considered. Online I/Q imbalance compensation not only reduces the stringent requirement on electrical components but also alleviates the impact of I/Q mismatch by employing a certain number of training sequences to compensate for the impairments automatically.

Consequently, for I/Q imbalance compensation in real-time processing, the following questions need to be answered:

- How to design a compensation scheme that performs well in the presence of CFO?
- How to implement the compensation algorithms in hardware since lots of complex divisions and matrix operations are needed?
- To get a balance between system performance and processing speed, algorithm simplification and data resolution reduction are required. What is the impact of them?

1.3 Thesis Outline

The remainder of this thesis is laid out as follows:

Chapter 1: Introduction

This chapter provides an overview on the thesis and research motivation.

Chapter 2: Literature Review

This chapter reviews the relevant literature on high-speed optical transmission technologies, real-time demonstrations of optical transmissions as well as I/Q imbalance compensation techniques.

Chapter 3: Fundamentals of Real-time CO-OFDM Systems

This chapter illustrates OFDM principles including basic mathematical formulas and models. Then coherent optical OFDM fundamentals such as the system architecture, optical MIMO-OFDM models and signal processing algorithms are discussed. The modern silicon technologies to build up real-time signal processing setup are surveyed. Finally the principle of I/Q imbalance is discussed.

Chapter 4: Real-time Single-Input Single-Output CO-OFDM Reception

This chapter conducts analysis on real-time signal processing algorithms for CO-OFDM systems. Firstly, major signal processing modules are discussed concerning the principles, differences from off-line algorithms and the optimization for hardware implementation. Secondly, three real-time experiments are demonstrated to show the system architecture and performance. The first real-time CO-OFDM reception and the record real-time single-channel data rate of 12.1 Gb/s are achieved. In the last experiment a novel setup named recirculated frequency shifter (RFS) which is used for multi-band optical OFDM signal generation is investigated thoroughly. A 22 bands wide spectrum OFDM signal is successfully generated and received.

Chapter 5: Real-time Multiple-Input Multiple-Output CO-OFDM Reception

This chapter conducts experimental works on high-speed coherent optical MIMO-OFDM transmissions from 6.67 Gb/s to 110 Gb/s. Firstly, real-time MIMO-OFDM specific signal processing algorithm--Jones matrix estimation is discussed. Then the first 6.67-Gb/s single-band real-time CO-MIMO-OFDM experiment is shown. The optical recirculation loop is investigated thoroughly in the following section to achieve a long-haul transmission in laboratory. A RFS is employed to generate 11 uncorrelated optical OFDM bands for the record 110-Gb/s real-time MIMO reception.

Chapter 6: I/Q Imbalance Compensation for CO-OFDM Systems

This chapter investigates the cause and solution of I/Q imbalance for CO-OFDM signal. The two experiments, one with off-line signal processing and the other with real-time signal processing, are demonstrated to prove the feasibility and effectiveness of I/Q imbalance compensation for coherent optical OFDM transmissions.

Chapter 7: Conclusions

This chapter summarize the conclusions of this thesis.

1.4 Contribution of the Thesis

The contributions of the thesis are listed as follows.

Chapter 3

- We propose CO-OFDM system architectures such as direct up/down conversion and intermediate frequency architecture.
- We propose the MIMO-OFDM model in the optical domain and adopt algorithms to recover two polarization signals.
- We proposed a system setup for real-time CO-OFDM reception and analysis the restrictions of critical components to system performance.

Chapter 4

- A numerical simulation is carried out to investigate the OFDM frame synchronization algorithms in the optical channel.
- We demonstrate the first multi-gigabit real-time CO-OFDM receiver up to 3.1 Gb/s for 16-QAM modulation format.
- We demonstrate the record data rate of 12.1 Gb/s for real-time single-band CO-OFDM reception.
- We propose a setup named recirculating frequency shifter (RFS) for the purpose of optical multi-band generation and performance investigation.

Chapter 5

- We deploy the polarization multiplexing in real-time CO-OFDM systems. The data throughput capacity of the single mode fibre is doubled.
- We develop the first real-time CO-MIMO-OFDM reception up to 6.67 Gb/s.

- We experimentally demonstrate a 110-Gb/s real-time CO-MIMO-OFDM reception with 600-km SMF transmission and 400-ps Differential-Group-Delay (DGD).

Chapter 6

- We develop a scheme to compensate I/Q imbalance at the transmitter and the receiver for direct up/down conversion architecture.

- We demonstrate an I/Q imbalance calibration with off-line signal processing for the 10.8-Gb/s CO-OFDM transmission.

- We achieve the first real-time I/Q imbalance compensation for CO-OFDM transmission.

1.5 Publications and Awards

Journal Papers

[1] Simin Chen, Yiran Ma, Qi Yang, Xi Chen, Abdullah Al Amin and William Shieh, "Ultra-broadband OFDM signal generation for 1-Tb/s super-channel coherent optical OFDM transmission," Accepted by Optics Communications (invited).

[2] Simin Chen, Yiran Ma and William Shieh, "Multiband Real-Time Coherent Optical OFDM Reception up to 110 Gb/s with 600-km Transmission," IEEE Photonics Journal, Volume 2, Number 3, June 2010.

[3] Simin Chen, Qi Yang, Yiran Ma and William Shieh, "A Multi-gigabit Real-time Receiver for Coherent Optical MIMO-OFDM Signals," J. Lightwave Technology, Vol. 27, 3699-3704, 2009.

[4] Qi Yang, Simin Chen, Yiran Ma and William Shieh, "Real-time reception of multi-gigabit coherent optical OFDM signals," Opt. Express, Vol. 17, 7985-7992, 2009.

[5] Yiran Ma, Qi Yang, Yan Tang, Simin Chen and William Shieh, "1-Tb/s single-channel coherent optical OFDM transmission over 600-km SSMF fiber with subwavelength bandwidth access," Opt. Express Vol. 17, 9421-9427, 2009.

[6] Yiran Ma, Qi Yang, Yan Tang, Simin Chen, and William Shieh, "1-Tb/s Single-Channel Coherent Optical OFDM Transmission With Orthogonal-Band Multiplexing and Subwavelength Bandwidth Access," J. Lightwave Technol. 28, 308-315, 2010.

[7] Qi Yang, Abdullah Al Amin, Xi Chen, Yiran Ma, Simin Chen and William Shieh, "428-Gb/s single-channel coherent optical OFDM transmission over 960-km SSMF with constellation expansion and LDPC coding," Opt. Express 18, 16883-16889, 2010.

Conference Papers

[1] Simin Chen, Abdullah Al Amin and William Shieh, "Real-time IQ Imbalance Compensation for Coherent Optical OFDM Transmission," OFC'2011, OWE2.

[2] Simin Chen, Abdullah Al Amin and William Shieh, "Hybrid Frequency-Time Domain Tx and Rx IQ Imbalance Compensation for Coherent Optical OFDM Transmission," ACP'2010, FO6.

[3] Simin Chen, Qi Yang, Yiran Ma and William Shieh, "110-Gb/s Multi-Band Real-Time Coherent Optical OFDM Reception after 600-km Transmission over SSMF Fiber," OFC'2010, OMS2.

[4] Simin Chen, Qi Yang, Yiran Ma and William Shieh, "Multi-gigabit Real-time Coherent Optical OFDM Receiver," OFC'2009, OTuO4.

[5] Simin Chen, Qi Yang and William Shieh, “Demonstration of 12.1-Gb/s Single-band Real-time Coherent Optical OFDM Reception,” OECC’2010, 8B4-2.

[6] Simin Chen, Qi Yang, Yiran Ma and William Shieh, “Real-time Coherent Optical MIMO-OFDM Reception up to 6.67 Gbps,” OECC’2009, ThJ2.

[7] Yiran Ma, Qi Yang, Simin Chen and William Shieh, “Multi-tone Generation using a Recirculating Frequency Shifter and Its Application to 1-Tb/s Coherent Optical OFDM Signal,” OECC’2009, ThLP75.

[8] Yiran Ma, Qi Yang, Yan Tang, Simin Chen and William Shieh, “1-Tb/s per Channel Coherent Optical OFDM Transmission with Subwavelength Bandwidth Access,” OFC’2009, PDP C1.

[9] William Shieh, Yiran Ma, Qi Yang, Yan Tang and Simin Chen, “Transmission channel rate for coherent optical OFDM - is the sky the limit?” LEOS’2009, ThM4 (Invited).

Awards

ACP 2010 Best Student Presentation Award Runner-up

OECC 2009 IEEE Best Student Paper Award

Chapter 2

Literature Review

2.1 Introduction

OFDM is an attractive multiplexing technique that has received a lot of attention in the fibre-optic community [13, 15-16, 24, 30]. It is a multi-carrier transmission technique which divides the whole spectrum into several subcarriers. Each subcarrier is modulated by a lower data rate stream. Optical OFDM has the following advantages [34]:

- It reduces the symbol rate, which makes optical OFDM robust to CD and PMD.
- It transfers the complexity of transmitters and receivers to the digital domain. The implementation of IFFT and FFT greatly simplifies OFDM modulation and demodulation.
- The subcarriers are mathematically orthogonal over one OFDM frame period. The spectra of subcarriers are partially overlapped, resulting in high spectral efficiency.

There are two main architectures for optical OFDM receivers: direct detection and coherent detection. Direct detection receivers are simpler than their coherent detection counterparts. They only deal with the square of the received optical intensity and, as a consequence, lose all the phase information of an optical signal. Direct detection optical OFDM (DDO-OFDM) is realized by using a single-end photodiode to convert the optical signal back to the electrical domain, while coherent optical OFDM requires a local oscillator, an optical hybrid and a balanced photo detector to beat the OFDM signal to baseband. The main advantages of DDO-OFDM are that it is a cost-effective solution and very tolerant to laser phase noise, which is more suitable for short reach applications. On the other hand, CO-OFDM has more spectrally

efficiency, PMD tolerance and less Optical Signal-to-Noise Ratio (OSNR) requirements, which makes it an excellent candidate for long-haul transmission systems. The major drawbacks of CO-OFDM are that the coherent detection is polarization dependent and sensitive to phase noise from the local oscillator [13].

Driven by more and more complex algorithms, the need for higher digital signal processing ability is escalating rapidly. Traditionally, coherent receivers are equipped with complicated phase-locked local oscillators to obtain signal phase and polarization information. But recent advances in silicon technology make it possible to use digital signal processing techniques to demodulate high-speed optically modulated signals. Pairing digital signal processing with coherent optical receivers has attracted more and more attention recently due to the potential of demodulating advanced formats without the increased complexity and cost.

Within direct conversion architecture, I/Q imbalance leads to a distortion to the I- and Q-branch. This spurious effect occurs mainly due to amplitude and phase impairments between the local oscillator paths as well as the I/Q branches after down conversion.

This chapter undertakes the literature review on the topics of (i) optical OFDM, (ii) real-time optical transmission systems, and (iii) I/Q imbalance compensation algorithms.

2.2 Optical OFDM

OFDM is a special case of frequency-division multiplexing (FDM) scheme used as a digital multi-carrier modulation method. A large number of orthogonal subcarriers are used to carry data. The transmitting data are divided into several parallel streams, one for each subcarrier. Each subcarrier is modulated with a conventional modulation scheme at a relatively low symbol rate, while maintaining the total data rates similar to conventional single-carrier modulation schemes in the same bandwidth. OFDM has been developed for wideband digital communications, whether wired, wireless or optical channel, used in applications such as the digital television and the audio

broadcasting, wireless networks and broadband optical backbones.

The major advantage of OFDM over single-carrier scheme [35-38] is the ability to deal with severe channel conditions without complex equalization filters. The channel equalization is simplified since OFDM can be viewed as many slowly-modulated narrowband signals rather than one fastly-modulated wideband signal. The low symbol rate makes the use of Guard-Intervals (GIs) or Cyclic-Prefixes (CPs) between symbols affordable, making OFDM possible to handle time-spreading phenomenon and eliminate Inter-Symbol Interference (ISI).

The history of orthogonal multicarrier transmission dates back to the mid-1960s, when Chang firstly proposed his concept on the synthesis of band-limited signals for the multi-channel transmission to combat the multi-path fading [39 - 40]. He introduced the principle of transmitting data through a band-limited channel simultaneously without interference between sub-carriers and consecutive data sequences in the time domain. Later, Saltzberg performed further analysis on this issue [41]. The employment of Fourier transform for base-band processing instead of a bank of sub-carrier oscillators was suggested by Weinstein and Ebert [42]. OFDM started to be considered as a practical technology in wireless communication in 1980s. At that time, Cimini in Bell Labs published early experimental results on the performance of OFDM modems and developed the first proof-of-concept OFDM system [43]. In mid-1990s, OFDM was proved to have better performance than conventional single-carrier systems in several field experiments. Since 1999, OFDM was accepted by the IEEE committee for many wireless standards such as 802.11, 802.16, etc.

OFDM in optical communications was first proposed on 2006 by Shieh et al. with coherent detection [13] and Lowery et al. with direct detection [44-45]. After that, there had been rapid progress on optical OFDM research. 100-Gb/s [46-48] and 1-Tb/s [49-50] per channel long-haul transmissions had been demonstrated. Real-time optical OFDM was also implemented by many groups [51-54].

2.2.1 System Architecture

The most critical thing for an optical OFDM system is to linearly modulate electrical OFDM signal into the optical domain, transmit this signal to receiver and demodulate it back to electrical signal for processing. To convert OFDM signal to optical domain, we can either use an indirect modulation method or a direct one. The indirect conversion employs a complex electrical I/Q mixer to up-convert the baseband OFDM signal to an Intermediate Frequency (IF). The up-converted electrical signal is modulated onto the optical waveform by using a simple optical intensity modulator, as shown in Figure 2.1(a). The direct method employs an optical I/Q modulator to finish the electrical/optical conversion, as shown in Figure 2.1(b).

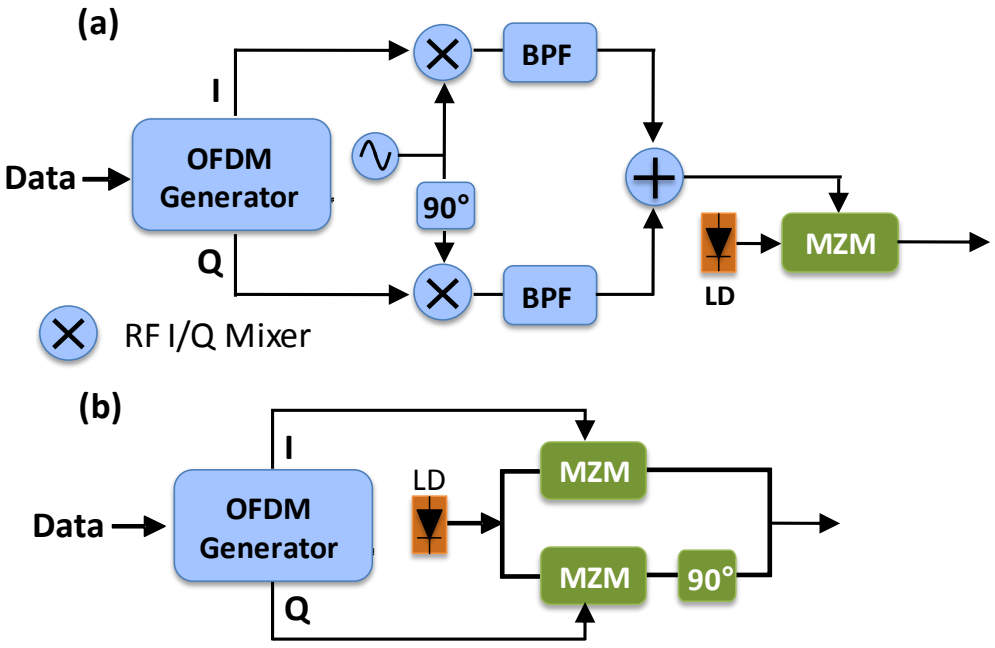

Figure 2.1: Electrical to optical converter (a) intermediate architecture and (b) direct up-conversion architecture.

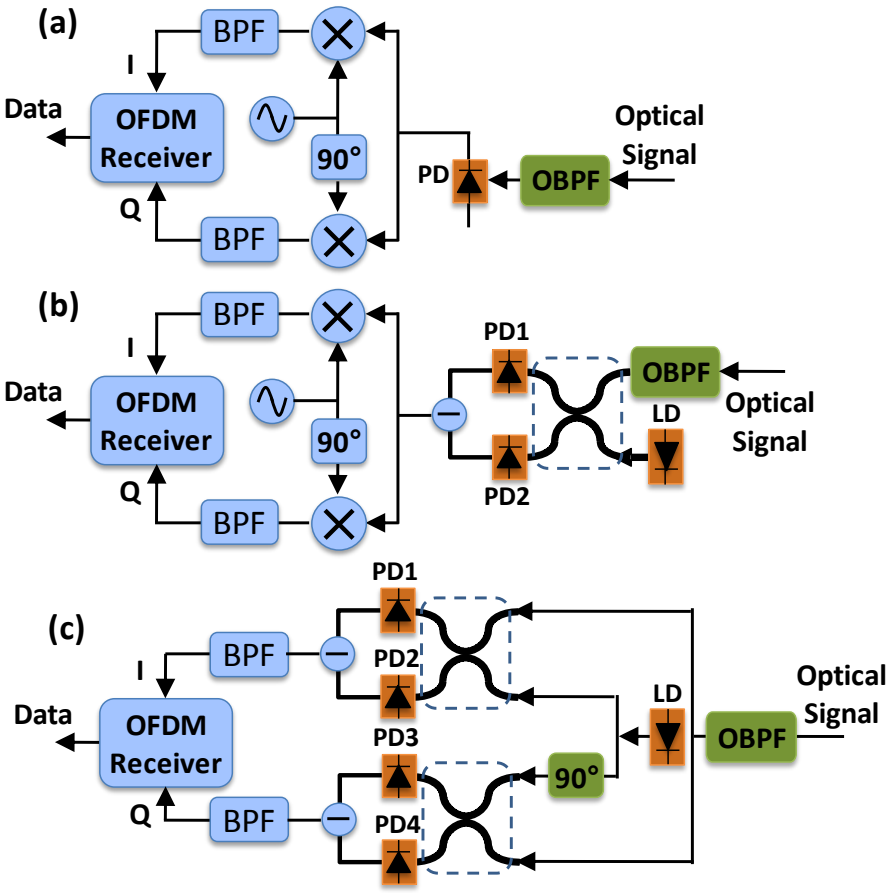

Figure 2.2: Optical to Electrical converter (a) DDO-OFDM, (b) heterodyne architecture for CO-OFDM and (c) homodyne architecture for CO-OFDM.

At the receiver side, photodiodes are applied which operate according to the square law detection scheme. It is impossible to transfer optical OFDM signal directly back to the electrical domain. An optical carrier must be provided either from the transmitter (DDO-OFDM, Figure 2.2(a)) or a local oscillator in the receiver (CO-OFDM, Figure 2.2(b) and Figure 2.2(c)) with heterodyne or homodyne architecture, respectively. In heterodyne scenario, the optical OFDM signal is converted into an IF electrical OFDM signal. The real and imaginary components are recovered at baseband by using an electrical I/Q demodulator. While in homodyne architecture, the local oscillator wavelength is finely tuned to close to the transmitter wavelength. The OFDM signal beats with the local oscillator (LO) waveform in a 90 ° optical hybrid to obtain the I and Q components of the OFDM signal.

2.2.2 Direct Detection Optical OFDM

In a DDO-OFDM transmitter, the electrical OFDM signal is generated after up-conversion. It directly drives the electrical/optical modulator, whereas the modulator's bias point determines the contribution of the laser's Continuous Wave (CW) signal, and the average amplitude of the electrical OFDM signal determines the intensity of optical OFDM signal. The spectrums of electrical and optical signals are plotted in Figure 2.3. In the presence of chromatic dispersion, it is necessary to remove one of the two optical sidebands by using an optical filter to generate Single Side Band (SSB) optical OFDM signal (Figure 2.3(c)).

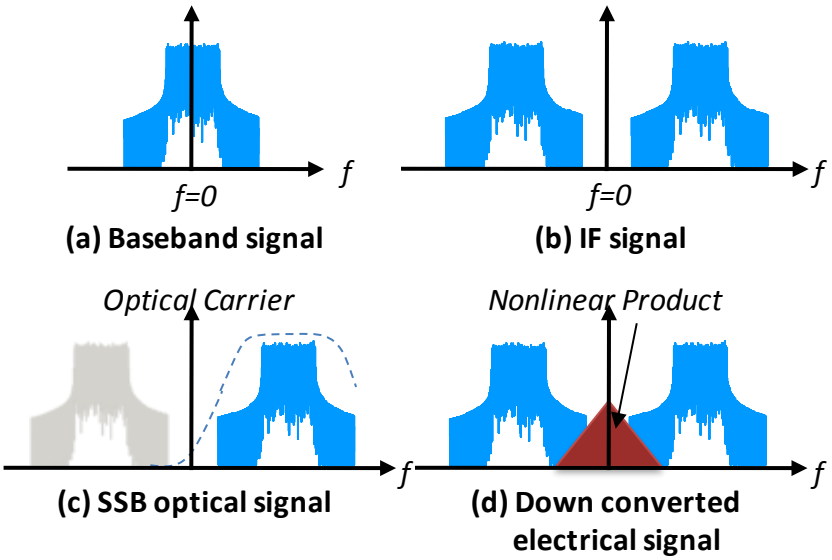

Figure 2.3: Illustration of linearly conversion from electrical domain to optical domain.

At the receiver side, the optical carrier mixes with the optical signal in the photodiode to regenerate the electrical OFDM signal. The output of photo detector consists of a Direct Current (DC) component, a fundamental term containing OFDM subcarriers and a second order nonlinear product (Figure 2.3(d)). If the optical OFDM signal spectrum is located close to the optical carrier in the frequency domain, the second order products are located in the same frequency range as the electrical OFDM signal, leading to performance degradation. The first DC term can be easily removed by a DC block. The second linear term is the signal to be retrieved and the last

nonlinear one should be removed. Several approaches are developed to minimize the penalty due to the second-order nonlinearity term.

■ ***Offset SSB-OFDM***

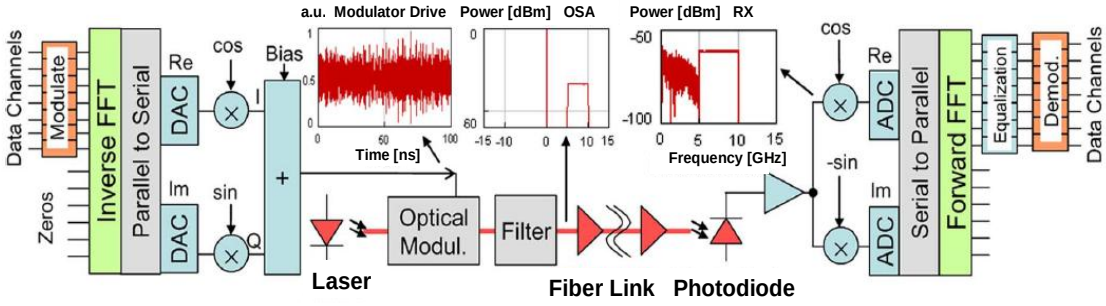

Figure 2.4: Offset SSB-OFDM long-haul optical system. After Ref. [55].

The proposed 10-Gb/s per channel offset SSB-OFDM system with 4-QAM modulation is shown in Figure 2.4 [55]. The OFDM signal is up-converted from baseband to 7.5-GHz RF domain at the transmitter, which generates the RF OFDM signal spans from 5 to 10 GHz and then fed into the optical modulator. The spectrum of optical OFDM signal is comprised of two symmetric optical bands aside the optical carriers. The optical carrier is suppressed to increase the received electrical power for a given optical power, and so the receiver sensitivity is improved. An optical band-pass filter is used to remove lower band. Therefore, only one sideband is received at the receiver to ensure one-to-one mapping from the optical to the electrical OFDM signal. The third inset of Figure 2.4 depicts the nonlinear second order component after the detector. It is obvious that the desired OFDM signal is not overlapped by the nonlinear component, which means the distortion will not affect system performance after proper electrical filtering.

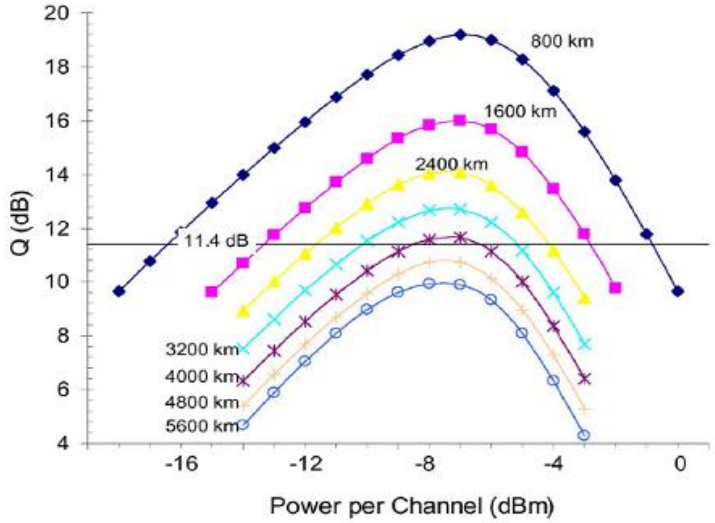

Figure 2.5: Q factor versus launch power into fibre per channel with different reach. After Ref. [55].

Figure 2.5 shows simulation results of 8 WDM channels offset SSB-OFDM system with 15-GHz spacing in different launch power. The seven curves are drawn in distinct colours to represent different transmission distances from 800 km to 5,600 km. For each distance the launch power has its optimal value. For lower launch powers, the Q factor is limited by optical power and ASE noise, while for higher input power, Q is determined by the fibre nonlinearity since the Q decreases approximately 2 dB if input power increases every 1 dB. For instance, the optimum launch power for 800 km transmission is about -6.5 dBm and the optimum Q is around 18 dB.

■ ***Baseband Optical SSB-OFDM***

Offset SSB-OFDM has a disadvantage of low spectrum efficiency. Baseband optical SSB-OFDM is proposed to solve it by Hewitt [56]. However, the baseband SSB-OFDM system is contained by two defects: it does not consider how to overcome the influence of the Signal-Signal Beat Interference (SSBI) produced by the photodiode reception [58] and the ability of combating fibre nonlinearity is poor. To overcome the two problems, a novel scheme to generate a baseband SSB-OFDM optical signal is proposed [57] by using a parallel optical single-sideband modulator which consists of two parallel dual-drive Mach-Zehnder Modulators (MZMs). Meanwhile, only the even subcarriers are used to transmit the data and the odd ones are left blank to

overcome SSBI [58]. The simulation setup for the scheme is the shown in Figure 2.6. Figure 2.7 shows the optical spectrum of the baseband SSB-OFDM signal. The positive sideband is filled with data and the DC component is used as the main carrier while the other sideband is left empty.

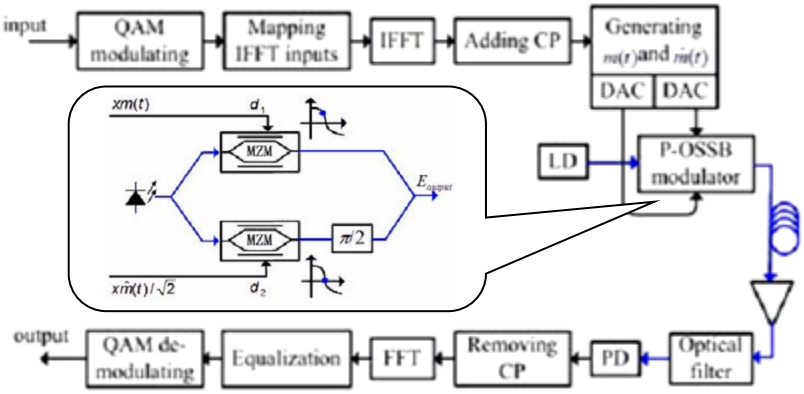

Figure 2.6: Simulation setup for the baseband SSB-OFDM system. After Ref. [57].

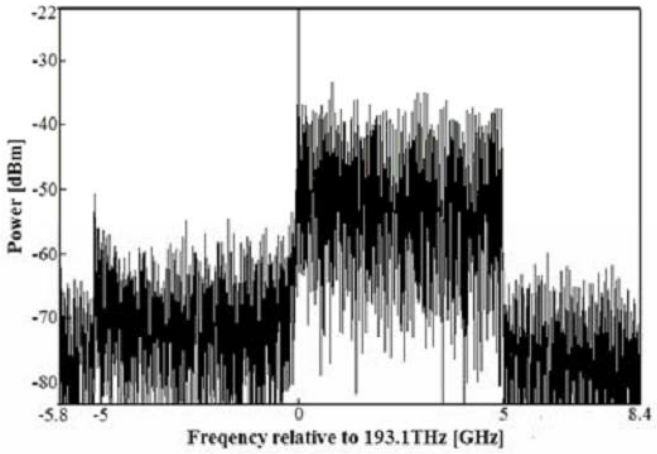

Figure 2.7: Optical spectrum for baseband optical SSB-OFDM. After Ref. [56].

The BER performances for the conventional SSB-OFDM scheme and the baseband SSB-OFDM scheme after 320 km transmission are compared in Figure 2.8. The data rate is 10 Gb/s. Fibre nonlinearity is not considered in this case. The results show a 4.5-dB benefit of required OSNR for the baseband SSB-OFDM scheme comparing with the conventional SSB-OFDM scheme. The decrease of required OSNR for the baseband SSB-OFDM can be explained by the improved capability of overcoming the SSBI.

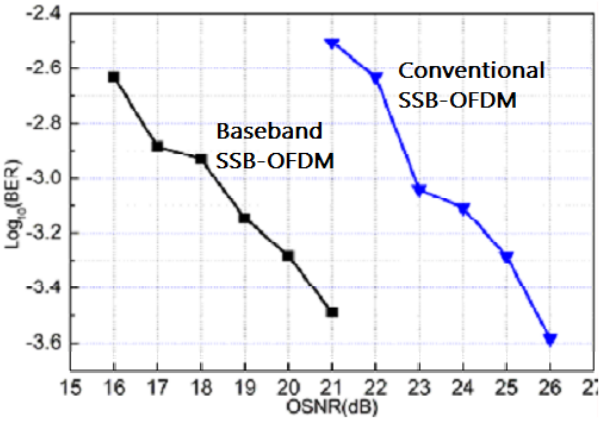

Figure 2.8: BER performance for 10-Gb/s systems after 320-km transmission. After Ref. [57].

■ ***RF Tone-Assisted OFDM***

RF Tone-assisted OFDM (RFT-OFDM) is proposed by Peng et al. to solve the problems of low spectrum efficiency in the offset SSB-OFDM and the second order nonlinearity in the baseband SSB-OFDM [58]. In this scheme the optical OFDM signal is generated coherently while detected directly. One RF tone for remote beating is placed at the left-most subcarrier. Figure 2.9 shows two types of RFT-OFDM, which named as OFDM-A and OFDM-B, respectively. For the OFDM-A, a gap with the same width as the signal spectrum is inserted between the RF tone and the signal. The second order nonlinear component falls on the gap. It will not lead to distortion to data subcarriers. The OFDM-A does not require electrical RF up-conversion. The required electrical bandwidth is smaller than the offset SSB-OFDM. The electrical spectrum of OFDM-A after the photo detector is shown in Figure 2.10(a). It is clear that all of the second order nonlinearity falls in the gap.

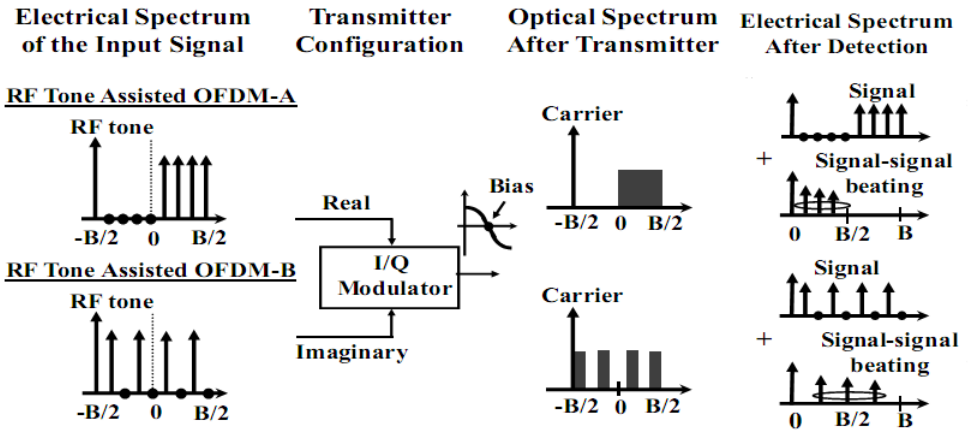

Figure 2.9: The principles for proposed RF-tone assisted OFDM-A and OFDM-B. After Ref [58].

For the OFDM-B, odd subcarriers relative to the RF-tone are used and the even subcarriers are left blank. The rest settings are the same as the OFDM-A. The second order nonlinearity will fall on those gaps. Therefore, in both OFDM-A and OFDM-B, the data subcarriers will not be affected by the nonlinearity effects. The spectrum after the photo detector is also shown in Figure 2.10(b).

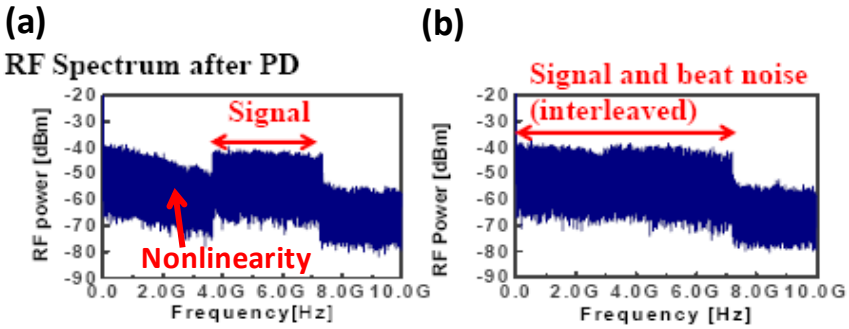

Figure 2.10: The RF spectrum after photo detector for both OFDM-A and OFDM-B. After Ref. [58].

An experiment is conducted to evaluate the performance of RFT-OFDM. In Figure 2.11 the Bit Error Rate (BER) performance is implemented for both the RFT-OFDM system and the conventional SSB-OFDM system at 10-Gb/s data rate with 8-QAM modulation format. It can be seen that the back-to-back (B2B) sensitivities of OFDM-A and OFDM-B are similar and both of them have a 5-dB better sensitivity

than the conventional SSB-OFDM. After 260-km standard SMF transmission, there are almost no penalties observed for this system.

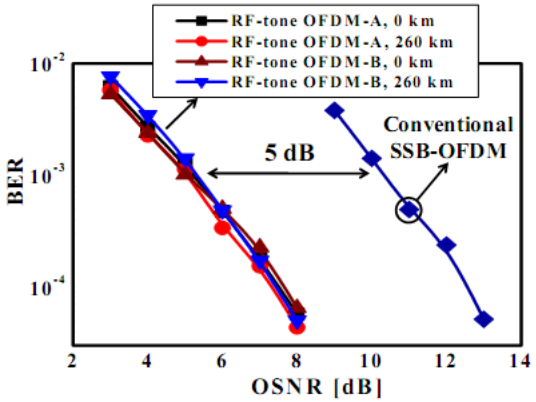

Figure 2.11: Experimental results of BER versus OSNR. The OSA resolution is 0.2 nm. After Ref. [58].

■ ***Virtual SSB-OFDM***

Virtual SSB-OFDM (VSSB-OFDM) is also proposed by Peng et al. to increase spectral efficiency while maintaining high sensitivity and CD tolerance [59]. A RF tone is inserted at the left most of all OFDM subcarriers for remote beating. No blank subcarriers are allocated such that this scheme saves half of electrical bandwidth than the conventional baseband SSB-OFDM. Figure 2.12 depicts the transmitter architecture of the VSSB-OFDM system. The optical I/Q modulator is biased at null point to minimize the modulation nonlinearity. At the receiver, the second-order nonlinearity that will degrade the performance is removed by an iterative cancellation technique. The principle is shown in Figure 2.13 and explained as follows: (i) the photocurrent is firstly stored in memory and is used to made decisions; (ii) using the decisions to reconstruct the SSBI; (iii) subtract the rebuilt SSBI from the stored photocurrent and make decisions; (iv) repeat stage (ii) and (iii) until the constellation converges. The whole procedure can be executed for several times until satisfactory results are achieved. The inset of Figure 2.13 compares the received signal constellation before and after 2 iteration processing.

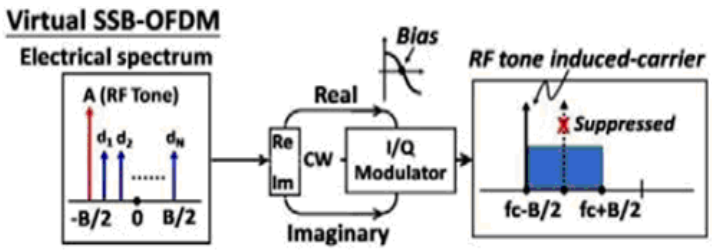

Figure 2.12: Transmitter architecture for VSSB-OFDM. After Ref. [59].

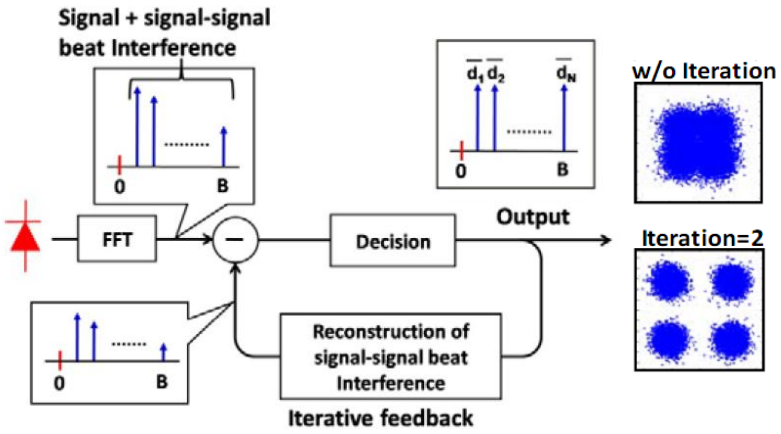

Figure 2.13: Iterative processing to remove second order nonlinearity. After Ref. [59].

The BER performances are measured for the conventional SSB-OFDM and the VSSB-OFDM in Figure 2.14. Due to the high requirement for the electrical bandwidth and the maximum sampling rate restriction of Arbitrary Waveform Generator (AWG), the constellation size of the conventional SSB-OFDM is set to 8-QAM to reach the same 10-Gb/s data rate as the VSSB-OFDM. The required OSNR at a BER of 1×10^{-3} for the VSSB-OFDM is 5-dB better than the conventional SSB-OFDM. The 5-dB gain is attributed to the optimum Carrier to Signal Power Ratio (CSPR) and a smaller constellation size. After 340-km standard SMF transmission, there is negligible penalty observed for the VSSB-OFDM system. However it is notable that the improvement comes with the cost of computational complexity.

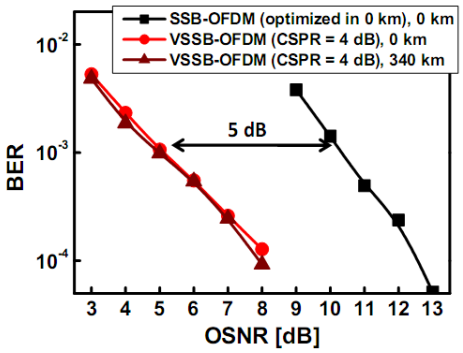

Figure 2.14: Measured BER versus OSNR for the conventional and virtual SSB-OFDM. The OSA resolution is 0.2 nm. After Ref. [59].

2.2.3 Coherent Optical OFDM

Compared with the DDO-OFDM, CO-OFDM has the advantages of higher receiver sensitivity, spectral efficiency and robustness against PMD with the cost of higher structural and computational complexity. CO-OFDM was first proposed by Shieh et al. [13]. The first experimental demonstration of CO-OFDM was provided by Shieh et al. for 1,000-km transmission over standard SMF at 8 Gb/s [60] and Jansen et al. for 4,160-km transmission at 20 Gb/s [61].

In addition to the conventional CO-OFDM, in which the incoming optical signal and the local laser waveform come from two independent laser sources, a new architecture using self optical carrier extraction was proposed by Xu et al. [62] to reduce system complexity. Guard intervals are inserted in the time domain between adjacent OFDM sequences to accommodate fibre chromatic dispersion induced ISI. However, the GIs reduce spectral efficiency and system data rate. No-Guard-Interval CO-OFDM (NGI-CO-OFDM) was proposed by Yamada et al. where OFDM signal is constructed with no CP [63] to improve spectral efficiency, but the ISI caused by transmitter bandwidth limitations is not accommodated and a more complex blind equalization is required to compensate for the effect of PMD [64]. Liu proposed the Reduced-Guard-Interval OFDM (RGI-CO-OFDM) scheme [64] to overcome the drawbacks of the No-guard-interval CO-OFDM.

Theoretical fundamentals of CO-OFDM will be described in detail in Chapter 3. We majorly address some varieties of CO-OFDM other than my research work in this

section.

■ ***Conventional CO-OFDM***

The simplified CO-OFDM system architecture is shown in Figure 2.15. At the transmitter side, the data to be transmitted is mapped to Quadrature Amplitude Modulation (QAM) or Phase-Shift Keying (PSK) format and then modulated onto parallel subcarriers. Two DACs are used to transfer the I- and Q-channel of the OFDM signal to the analog domain. The electrical OFDM signal is then up-converted to the optical domain by using a carrier-suppressed optical I/Q modulator. At the receiver side, the optical signal beats with the local laser waveform and it is converted back to the electrical domain by two balanced photo detectors. The I and Q signals are sampled by two ADCs and demodulated by the FFT operation.

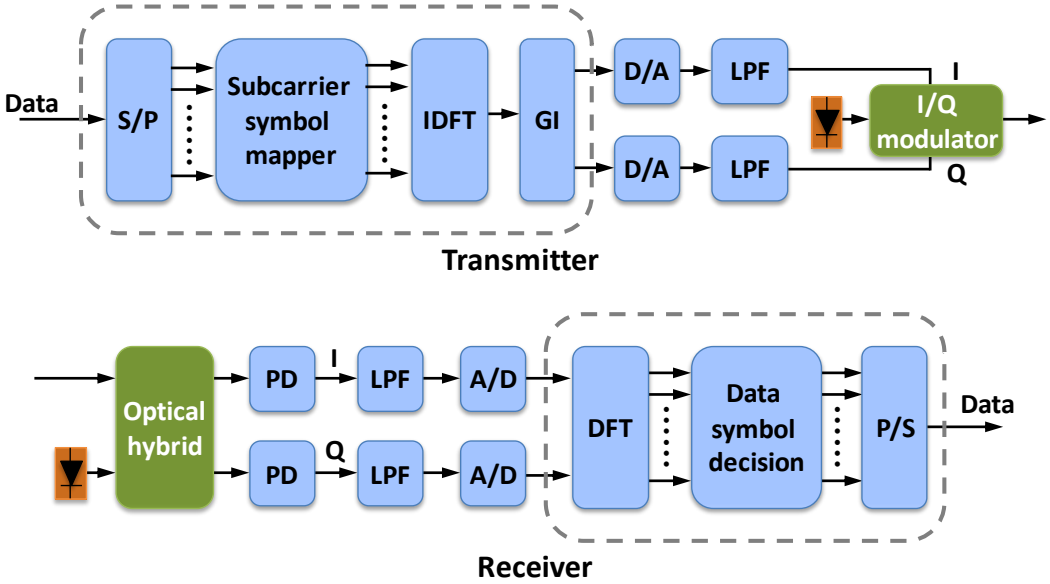

Figure 2.15: Typical CO-OFDM system architecture.

■ ***Self-Coherent Optical OFDM***

In conventional coherent optical communications, the incoming signal interferes with the Continuous Wave (CW) from a local oscillation (LO) laser in the optical hybrid for coherent detection. The local laser should have narrow linewidth, and should be tunable for the incoming signals at different wavelengths. For a digital coherent receiver, digital signal processing is used to conduct phase estimation to compensate

phase noise from local laser and polarization rotation estimation for polarization diversity detection scheme. Although significant progress has been made in high-speed DSPs, the speed and processing capabilities of current DSPs still fall far behind the requirement of practical implementations in real-time optical OFDM transmission. The self-coherent optical OFDM system architecture is aimed to reduce the complexity of required DSPs.

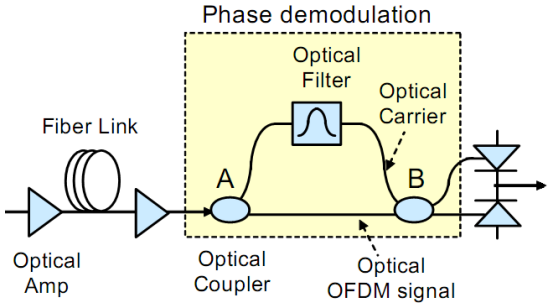

Figure 2.16: The principle of self optical carrier extraction. After Ref. [62].

The principle of self optical carrier extraction is shown in Figure 2.16. At the receiver side, the incoming optical OFDM signal is split into two branches by the optical coupler "A". One branch goes directly to coupler "B" and the other one passes through an optical band-pass filter to have the optical carrier component extracted for coherent interference. The requirements of this scheme are that the optical carrier component in incoming optical OFDM signal should not be highly suppressed and it should be separable from the incoming signal spectrum. The first condition can be easily satisfied by adjusting bias voltage of the modulator. The second requirement can be met by using either a RF carrier or zero padding [65].

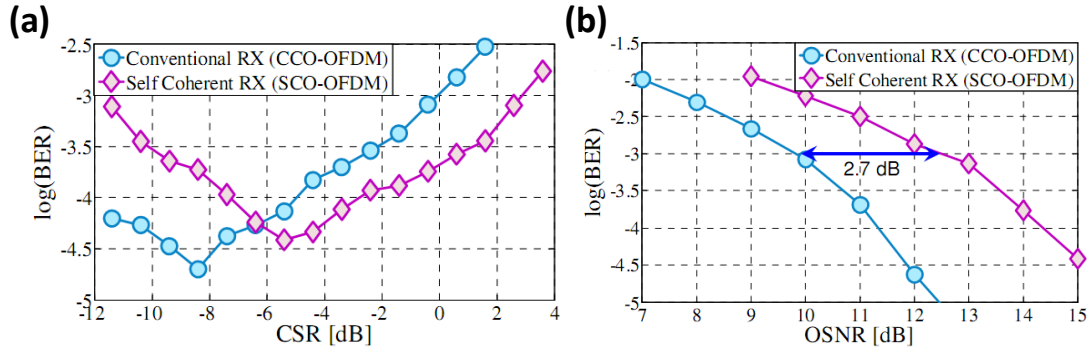

Figure 2.17: (a) BER as a function of CSR. (b) BER as a function of OSNR for back-to-back scenario. After Ref. [66].

The influence of this Carrier-to-Signal Ratio (CSR) on the BER performance is shown in a B2B transmission in Figure 2.17(a). The optimum CSR for conventional CO-OFDM is -8.4 dB with a BER of 2.0×10^{-5}. For self-coherent OFDM the value is -5.4 dB with a BER of 3.9×10^{-5}. When the CSR is below the optimum value, the optical carrier is too weak and the ASE noise limits the effectiveness of phase noise compensation. For high CSRs, the relative power of the OFDM signal becomes too low and hence the performance gets worse. Figure 2.17(b) depicts the B2B BER performance as a function of OSNR. The required OSNR for a BER of 1×10^{-3} is 9.8 dB for the conventional CO-OFDM and 12.5 dB for the self-coherent OFDM. The 2.7-dB difference is caused by the fact that in the self-coherent OFDM, the extracted optical carrier is contaminated by the ASE noise. This noisy carrier leads to distortions in the real and imaginary parts of the constellation. While in the conventional CO-OFDM, pilot tones are used for phase noise compensation and a clean local laser is used for coherent detection. In addition, the filter bandwidth in optical carrier extraction is significantly wider than the digital filter for conventional CO-OFDM phase noise compensation. The wider the filter bandwidth is set, the more noise is leaked to the carrier. It can be inferred that performance will be better with a narrower bandwidth filter.

- ***No-Guard-Interval CO-OFDM***

Yamada et al. proposed the NGI-CO-OFDM scheme to eliminate overhead. Without GIs, the linear distortion caused by CD and PMD is equalized by fixed-tap linear equalizers and adaptive Finite Impulse Response (FIR) filters with blind channel estimation at the receiver [63]. Figure 2.18 shows the NGI-CO-OFDM system configuration. At the transmitter, 76 channels of CW optical carrier were generated from Distributed Feed-Back (DFB) Laser Diodes (LDs). The odd and even channels of CW carrier are multiplexed to form two multi-tone optical sources, respectively. The OFDM modulation section consisted of a MZM acting as a 2-subcarrier generator and an integrated OFDM-QPSK subcarrier modulator to generate DWDM 44.4-Gb/s OFDM-QPSK signal. The even and odd channels are combined with an optical

interleaver. Finally, the 44.4-Gb/s DWDM OFDM-QPSK signals were polarization-multiplexed to form DWDM 88.8-Gb/s PDM OFDM-QPSK signals through a polarization multiplexer.

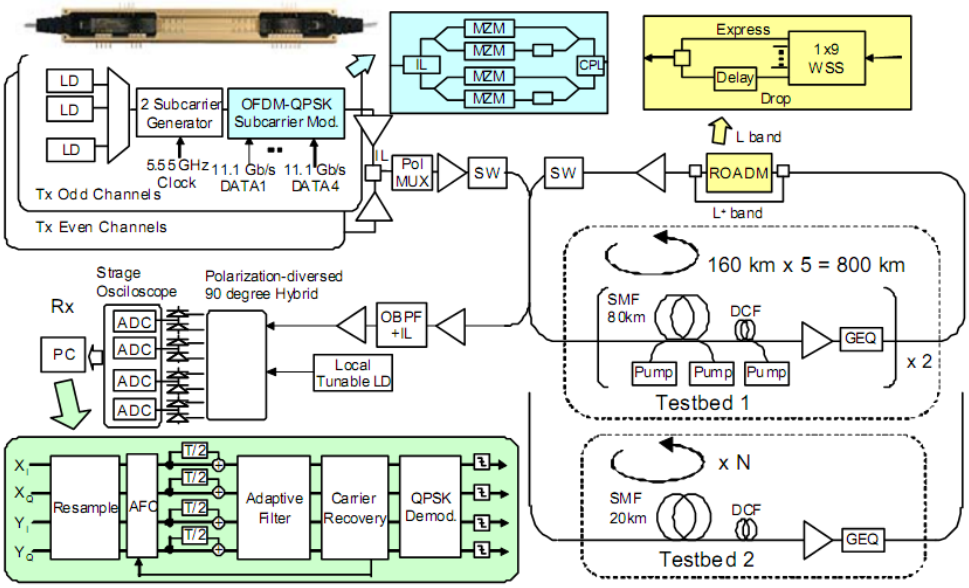

Figure 2.18: Experimental setup for PDM NGI-CO-OFDM signal transmission. After Ref. [63].

At the receiver, the PDM-OFDM signal is mixed with the CW from a local laser in a 90 ° optical hybrid. The real and imaginary parts of the PDM-OFDM signals at both polarizations are output to 4 balanced photo detectors (PDs). The local laser is tuned to the centre of one subcarrier spectrum, therefore this subcarrier is converted to baseband and the other subcarriers are filtered. The output signals from PDs were sampled by a digital storage oscilloscope running at 50 GSa/s.

Since the blind adaptive equalization with a transversal filter is used to compensate the ISI, the NGI-CO-OFDM schemes do not require guard intervals and training sequences.

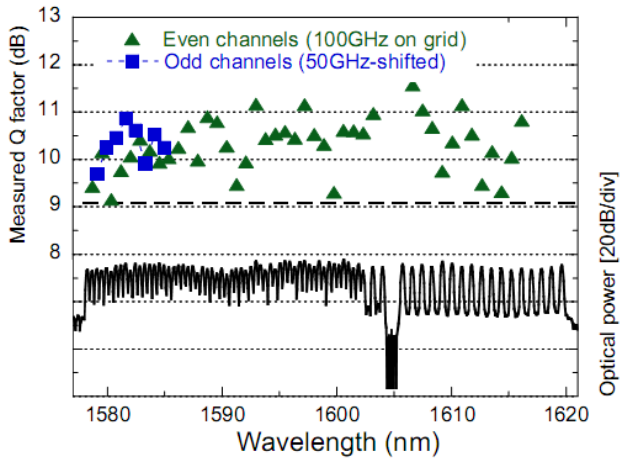

Figure 2.19: Measured Q-factors and WDM spectra after 800-km transmission. After Ref. [63].

The Q-factors of 50 channels in the transmitted 76 channels are measured in Figure 2.19. They are all better than 9.2 dB, which is beyond the Q-limit of 9.1-dB BER threshold (dashed line) of $1x10^{-12}$ with ITU-T G.975.1 enhanced FEC.

■ ***Reduced-Guard-Interval CO-OFDM***

In RGI-CO-OFDM systems, reduced GIs between adjacent OFDM sequences are inserted to accommodate the ISI induced by transmitter bandwidth limitations or fibre PMD, while the CD-induced ISI is compensated at the receiver, as is done in Single-Carrier Frequency-Domain Equalization (SC-FDE) systems [67]. The GIs only need to be longer than the memory length associated with PMD in the RGI-CO-OFDM. Therefore, the overhead and OSNR penalty due to GIs are dramatically reduced to 3.13% and 0.13 dB, respectively [64]. In essence, the RGI-CO-OFDM is a hybrid version of the conventional CO-OFDM and the SC-FDE. The RGI-CO-OFDM uses almost the same signal processing modules as the CO-OFDM. The only new ones are the steps of receiver side Electronic Dispersion Compensation (EDC) based on FFT, IFFT and overlap-add.

There are several benefits with short GIs and OFDM frame sizes: (1) shorter Training Sequences (TSs), which leads to a lower TS-induced overhead, (2) shorter OFDM frames, which leads to a higher channel tracking speed and a higher tolerance to clock or sampling frequency offset between the transmitter DACs and the receiver

ADCs, and (3) a higher tolerance to the laser linewidth. The only expense which has to be paid when applying the RGI-CO-OFDM is the use of additional signal processing to perform EDC. Nevertheless, owing to the efficiency of OFDM signal processing, the overall complexity of RGI-CO-OFDM is expected to be lower or similar to that of SC-FDE.

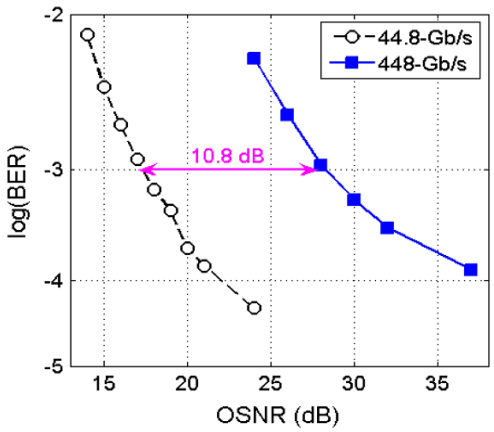

Figure 2.20: BER performance of the 10-band 448-Gb/s RGI-CO-OFDM signal as compared to the original single-band 44.8-Gb/s signal. After Ref. [64].

The measured BER as a function of OSNR is shown in Figure 2.20. The required OSNR for the 448-Gb/s signal is 28.2 dB at the BER of 1×10^{-3}, which is 10.8-dB higher than that for original single-band 44.8-Gb/s signal. The excess 0.8-dB penalty is due to band multiplexing and simultaneous detection of only 5 bands.

2.3 Real-time Optical Communication Systems

Telecommunication networks are the backbone of modern society which provides a rapid access to information exchange around the earth. There has been a considerable increase in demand for higher bandwidth and more reliable data and voice services in recent years. This development has put a serious challenge to telecommunication networks and exposed the limitations of current network architectures. Higher capacity next-generation optical networks, which are low cost and reliable, are needed to satisfy future bandwidth and flexibility requirements. A major obstacle to achieve higher bandwidth is the optical signal degradation. Therefore, it has become necessary

to develop novel digital signal processing techniques and modulation formats to resist fibre impairments.

Although real-time signal processors are widely used in wireless systems, their use in optical communications is limited because of much higher bit rates. However, the fast development of Complementary Metal-Oxide-Semiconductor (CMOS) technology has led to increasing interest on digital signal processors for optical transmission, which will allow major advances in performance and flexibility, and reduce cost for future photonic networks.

While ASIC offers optimal performance, the FPGA is a useful alternation in experimental works since it is low cost and field reprogrammable. In the latest digital systems, high-speed differential or serial interfaces are increasingly used for chip-to-chip signalling to replace single-end and parallel buses. They increase resistance to electromagnetic interference, reduce signal skew and pin numbers. Because of this reason, FPGAs with up to 28-Gb/s input/output capabilities are in production [68]. Given current trends, it is likely that high-speed differential or serial transceivers will become normal configuration for future FPGAs. This capability allows the latest FPGAs to be used for high-speed optical signal processing.

Advances in digital signal processing technology have elevated the capabilities of signal processors in optical communication. Hence, in certain communication schemes, for example the optical OFDM, the missing piece of the puzzle is getting the extremely-sensitive analog signals be converted to the digital domain for receiver. ADCs are pivotally important in trying to realize the goal.

2.3.1 Real-time Optical Single-Carrier Systems

Single-carrier modulation formats are employed since the start of optical communication. Most of them are binary signalling because they are easy to modulate and demodulate, for instance, duobinay, Non-Return-to-Zero (NRZ), Return-to-Zero (RZ), Phase-Shift-Keying (PSK) etc. The others are multi-level signalling such as Differential Quadrature-Phase-Shift-Keying (DQPSK) and M-ary Pulse Amplitude Modulation (M-PAM), etc.

High-speed real-time optical single-carrier signal processing based on the FPGA has become a research topic to improve system performance and flexibility. Watts published the first 10-Gb/s optical transmitter with real-time signal processing using an FPGA [69]. A coherent digital polarization diversity receiver for real-time polarization-multiplexed synchronous QPSK transmission with DFB lasers at a data rate of 2.8 Gb/s was reported by Pfau et al. [70]. Fukuchi et al. demonstrates a record data rate of 112-Gb/s transmission using the PM-QPSK format and the FPGA-based real-time digital signal processing [71] on 2010.

■ ***Real-time Optical Single-Carrier Transmitter***

The top-level design of real-time transmitter is shown in Figure 2.21. A MZM is driven by two drive signals d_1 and d_2. For both signals eight of the FPGA serial outputs (each running at 10 Gb/s) are time-division multiplexed to four 20-Gb/s signals. A DAC consisting of attenuators and a 4-to-1 power combiner generates the analog drive voltages.

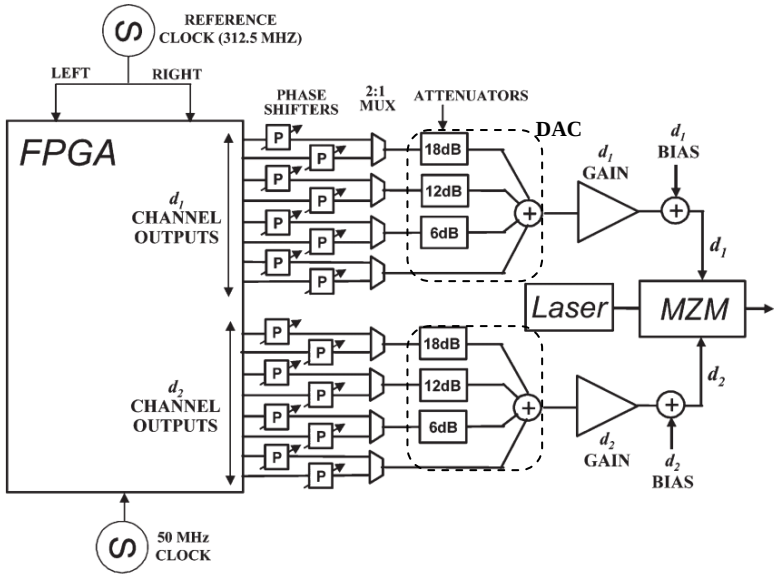

Figure 2.21: Top-level 10-Gb/s transmitter diagram. After Ref. [69].

A dual-drive MZM can be used to modulate the amplitude and phase of the transmitted optical signal. This allows the input bit stream to be pre-distorted to overcome transmission impairments. The input bit stream is filtered and converted

into two analog signals to drive the two ports of the MZM. On the other hand, a Look-Up Table (LUT) can be programmed to produce arbitrary, including nonlinear, responses. As shown in Figure 2.22, the LUT is stored in FPGA embedded memory with a length of 2n words. It is addressed by n consecutive bits of the input bit stream sequence. Each word contains m bits, where m is the resolution of the DAC multiplied by the oversampling ratio. In this experiment, LUT stores EPD waveforms to compensate fibre channel impairments.

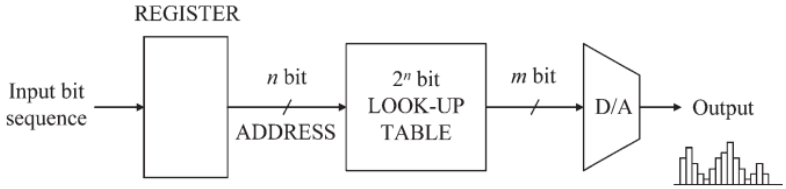

Figure 2.22: LUT used to create arbitrary, including nonlinear, responses. After Ref. [69].

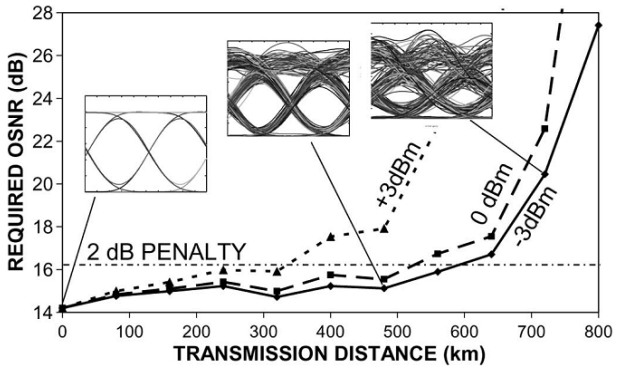

Figure 2.23: Performance of the 10-Gb/s transmitter using Electronic Pre-Distortion (EPD) with 11-bit LUT addressing with -3, 0, and +3-dBm launch power into each span and eye diagrams at 0, 480, and 720 km for -3-dBm launch power. After Ref. [69].

Figure 2.23 demonstrates the experimental result. It is observed that the chromatic dispersion after 550-km transmission can be compensated with less than 2 dB penalty at -3-dBm launch power per channel. The LUTs in this case are calculated to compensate for the chromatic dispersion only; hence, the performance at +3-dBm launch power is reduced without nonlinearity pre-distortion. However, the other work

has shown that intra-channel nonlinearities such as Self-Phase Modulation (SPM) can also be compensated by using the LUT approach [72].

■ ***Real-time Optical Single-Carrier Receiver***

The setup for 2.8-Gb/s polarization multiplexed synchronous QPSK transmission is demonstrated in Figure 2.24. Four 700-Mb/s Pseudo-Random Binary Sequence (PRBS) streams are fed into a QPSK pre-coder which encodes them as the differential QPSK format. The output bit streams are modulated onto the CW from the DFB laser in two QPSK modulators to generate a 2.8-Gb/s polarization-multiplexed QPSK signal. After 120-km standard SMF transmission, the signal is split into two arms with a Polarization Beam Splitter (PBS) and received by two 90 º optical hybrids in a polarization diversity coherent optical receiver. The four outputs from hybrids are converted to electrical signal by balanced photo detectors and then sampled by ADCs with a sampling rate of 700 MHz. Digital signal processing is undertaken in the FPGA to separate two polarizations. Finally, a feed-forward scheme recovers the optical carrier in spite of 2-MHz combined laser linewidth from the signal laser and the local laser.

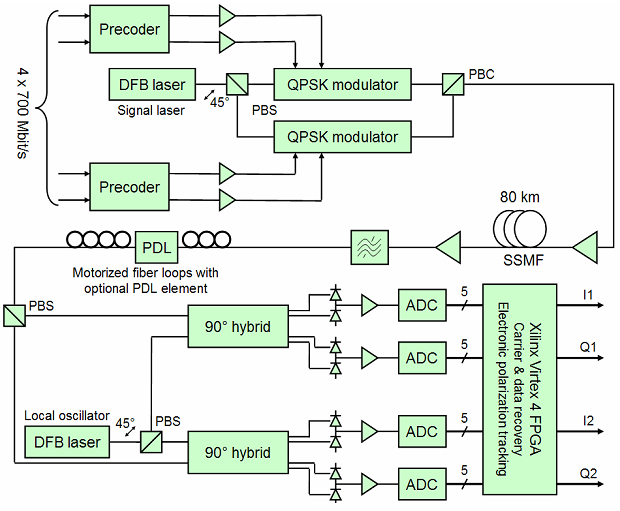

Figure 2.24: Setup for 2.8-Gb/s synchronous optical QPSK transmission with polarization division multiplex. After Ref. [70].

Fig. 2.25 shows the measured BER versus OSNR after 120-km transmission for the three scenarios. The first one was a constant polarization at the receiver input. The best measured BER for the filter with N=2 was 1.2×10^{-7} where N is the number of samples in each polarization for the phase estimation. For the filter with N=4, a BER of 1.6×10^{-5} was achieved. A polarization scrambler to generate endless polarization scrambling is inserted in the fibre link to test the performance of polarization control algorithm. This setup induces highly time-variance and degrades the minimum BER values to 2.4×10^{-7} for N=2, and 2.6×10^{-5} for N=4. Finally a 3-dB PDL is inserted in the transmission link. The minimum BER slightly degraded to 3.4×10^{-7} for N=2, and 3.5×10^{-5} for N=4.

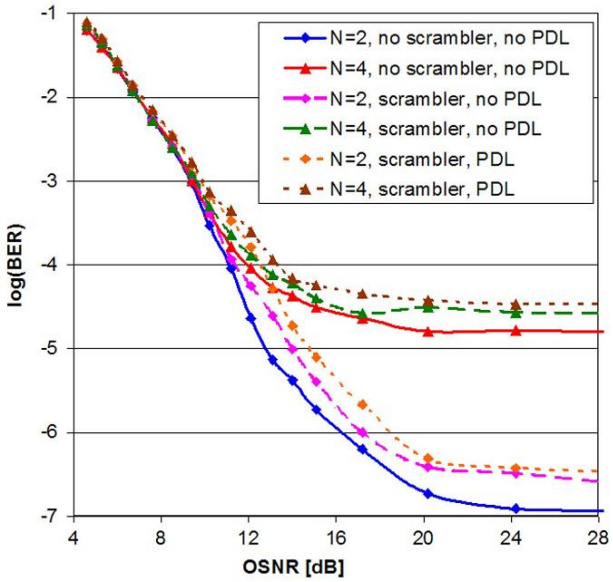

Figure 2.25: Measured BER versus OSNR for constant polarization at the receiver input and for fast polarization changes with and without PDL. PDL: Polarization-Dependent Loss. After Ref. [70].

■ ***Real-time Optical Single-Carrier Transponder***

The 112-Gb/s transponder employs the FPGA-based parallel digital signal processing to achieve a desired data throughput. Figure 2.26 shows a block diagram of the transponder. Optical signal is received by the CFP interface and fed to two Forward Error Correctors (FECs) for error correction. The two streams are realigned to four 28-Gb/s streams by the multiplexer and pre-coder. Differential coding is performed at

the pre-coder to avoid burst errors. The four signal lanes are used to modulate the CW from the tunable LD, generating polarization-multiplexed QPSK signals.

At the receiver, the polarization-diversity coherent optical front end with a local laser recovers electrical signals for each polarization. The four signals are sampled by four high-speed ADCs at 42 GSa/s. The sampling clock is generated from an external optical clock extractor. The sampled data are processed by the FPGA to output the 112-Gb/s data stream. The recovered data are then differential decoded, FEC decoded by the two FEC chips and then reconstructed at the CFP interface.

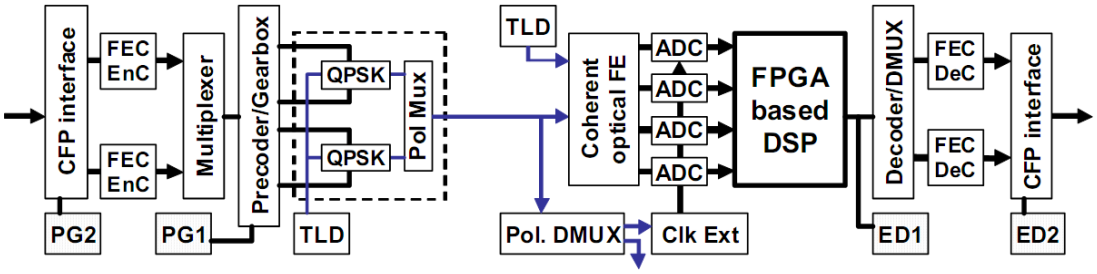

Figure 2.26: Block diagram of the optical transponder with real-time digital signal processing. After Ref. [71].

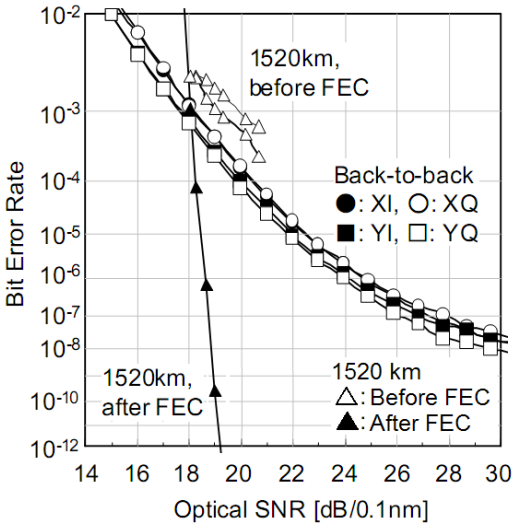

Figure 2.27: Measured BER versus OSNR for back-to-back and 1520-km WDM transmission. After Ref. [71].

Figure 2.27 shows the measured 112-Gb/s back-to-back BER with and without FEC versus received OSNR. The BERs of 1×10^{-8} is successfully achieved, which is

significantly lower than FEC threshold. All four channel BERs are very close. The BERs with and without FEC after 1520-km SMF transmissions are measured. The close triangle mark in Figure 2.27 shows the BERs before FEC, and the open triangle shows the BERs after FEC. The error correction is validated that a 10^{-3} BER is corrected to 10^{-12}.

2.3.2 Real-time Optical OFDM Systems

Since the optical OFDM introduces such efficient techniques from wired and wireless communication systems, one argument is that its implementation is straightforward or challenging. In fact, although lots of optical OFDM research works are reported based on off-line processing using high-speed sampling scopes and suggest many advantages [7-8, 13, 24, 30], most of them lack discussion on the possible implementation difficulties. Special requirements of optical communication systems, such as orders of magnitude higher data rate than wireless counterparts, demand additional attention and careful studies on the feasibility of real-time implementation for high-speed optical OFDM systems.

A limited number of real-time generation and detection have been demonstrated. Buchali et al. reported a real-time 12.1-Gb/s optical OFDM transmitter [73]. Killey et al. described an optical transmitter with electronic pre-distortion at 8.35 Gb/s [74]. At the receiver end, Chen et al. demonstrated the first single-band real-time CO-OFDM receiver at net data rate of 1.55 Gb/s [75]. Kaneda et al. introduced a 3.55-Gb/s real-time CO-OFDM reception [76]. A real-time optical OFDM transceivers which support a data rate of 3 Gb/s over 75-km SMF transmission was demonstrated by Jin et al. [77]. A 41.25-Gb/s DSP-based direct detected OFDMA-PON receiver was reported by Qian [78]. To overcome the bandwidth limit of electronic devices, Tang et al. proposed an all-optical sampling OFDM scheme [79] and Hillerkuss et al. demonstrated an all-optical FFT demodulation technique to generate and de-multiplex a 392-Gb/s OFDM signal [80].

- ***Real-time Optical OFDM Transmitter***

In [73], the high data rate real-time FPGA based OFDM transmitter employs two 10-GSa/s DACs to generate analog signals with a net data rate of 12.1 Gb/s. 400-km transmission experiments at 109 Gb/s with coherent reception are conducted using an on-line transmitter and an off-line receiver.

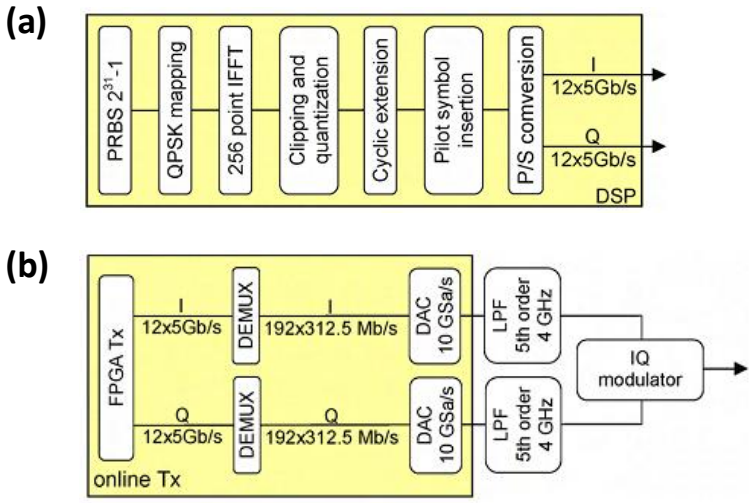

Figure 2.28: Real time optical OFDM transmitter: (a) DSP architecture; (b) FPGA-DAC integration. After Ref. [73].

The real-time transmitter is based on a Xilinx Virtex 5 FPGA. A PRBS generator drives the QPSK mapper. All 256 IFFT inputs are realized for the QPSK subcarrier modulation. After IFFT a combined 1-bit clipping and 3-to-1-bit re-quantization is applied to limit the data resolution to 6 bit. 8 samples are inserted as cyclic pre- and post-fix. Two synchronization sequences are inserted every 126 payload frames. A first pilot sequence is generated for OFDM frame synchronization and local oscillator frequency offset correction. A second pilot sequence is used for channel estimation.

The time domain real and imaginary signal components are reorganized, parallel to serial converted and output through 2×12 Rocket I/Os operated at 5 Gb/s. A further 1:16 DEMUX was required to interconnect the FPGA to the commercial 10-GSa/s DACs.

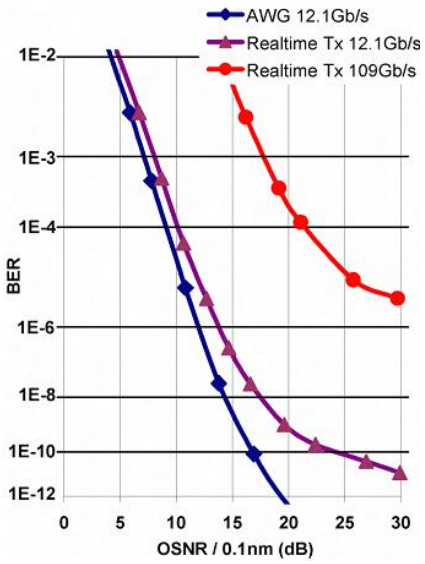

Figure 2.29: Comparison of BER in back-to-back configuration of offline Tx with AWG (diamonds), FPGA based real-time Tx (triangles) and 109-Gb/s transmission (bullets). After Ref. [73].

As shows in Figure 2.29, an OSNR penalty of 1 dB at BER 10^{-3} for the real-time transmitter was found. There is a penalty in the low noise regime (BER<10^{-8}) which is attributed to the limited numerical accuracy of the signal generation in the FPGA and a higher I/Q imbalance when driving the optical I/Q modulator due to experimental constraints.

■ ***Real-time DDO-OFDM Receiver***

Figure 2.30 depicts the experimental setup of the real-time OFDM receiver [78]. At the transmitter side, baseband OFDM signals were generated off-line and stored in the Read-Only Memory (ROM) of two FPGA evaluation boards. They are used to control two synchronized 20-GSa/s DACs. Two DFB lasers with λ_1 and λ_2 are employed as the CW optical sources for two intensity modulators (IM1 and IM2). The I/Q signal components are combined with a 50:50 optical coupler. The OFDM signal is transmitted to the real-time receiver through 20-km standard SMF. The incoming signal is amplified by an EDFA and split into λ_1 (I) and λ_2 (Q) channels by an arrayed waveguide grating. A fixed Optical Delay-2 (OD-2) is added to correct the inter-channel misalignment and enable I/Q signal path synchronization. The signals are

direct detected by two photo detectors (PD1 & PD2). The sampling and digitization are performed by a 2-channel 40-GSa/s ADC platform. The sampled data are then processed in real-time in the FPGA-based DSP platform.

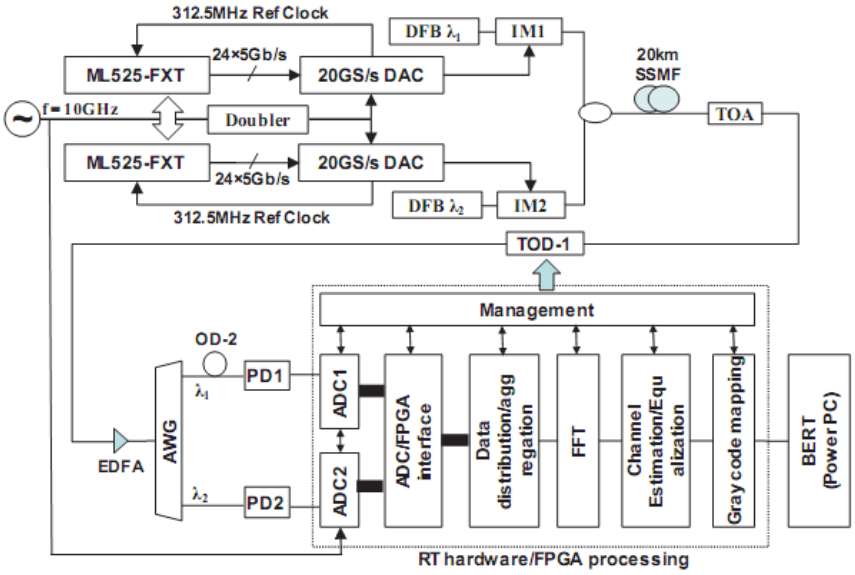

Figure 2.30: Experimental setup of the 41.25-Gb/s real-time variable-rate OFDM receiver. After Ref. [78].

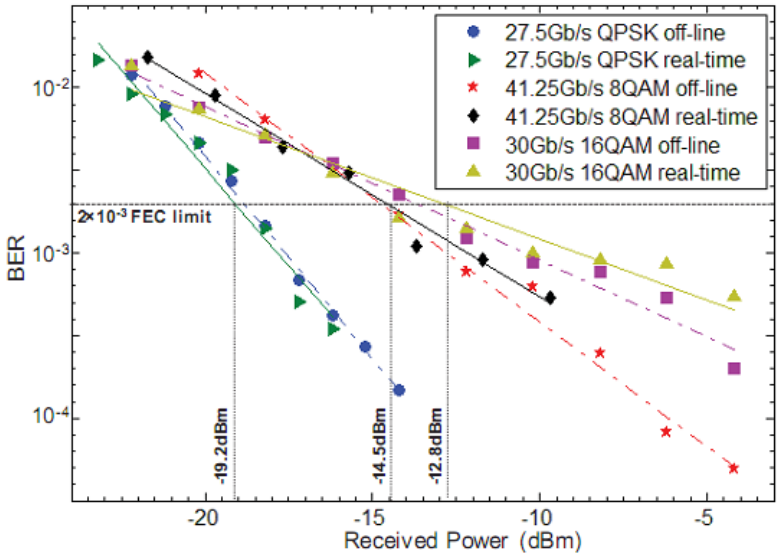

Figure 2.31: BER versus received optical power (dBm). After Ref. [78].

The measured real-time BER versus received optical power are plotted for QPSK, 8-QAM and 16-QAM signals after 20-km standard SMF transmission. As shown in Figure 2.31, the FEC threshold of BER = 2×10^{-3} was achieved with -19.2-dBm, -14.5-dBm and -12.8-dBm received powers for QPSK, 8-QAM, and 16-QAM transmission,

respectively. The penalty between the off-line and real-time processing results was negligible.

■ ***Real-time CO-OFDM Receiver***

A detailed discussion of my research work on real-time CO-OFDM reception will be presented in Chapters 4 and 5. In this section another experiment from Kaneda et al. [76] is demonstrated. The Figure 2.32 shows a typical opto-electronic block diagram of CO-OFDM receiver with two ADCs and a FPGA. The received OFDM signal is interfered with a local laser in an optical hybrid for I/Q separation. The I/Q signals are detected by photodiodes and amplified by Variable Gain Amplifiers (VGAs) to balance and optimize the amplitude for ADC sampling. Digitized signals are fed to FPGA for signal processing.

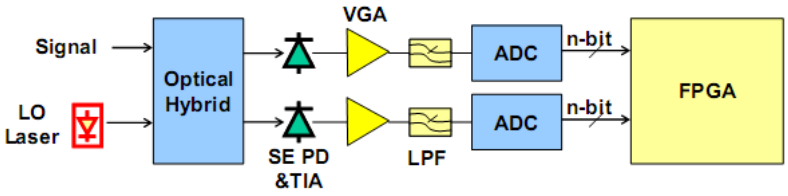

Figure 2.32: Opto-electrical block diagram of OFDM receiver with FPGA. SE PD TIA: Single-Ended Photo-Diode with Trans-Impedance Amplifier. After Ref. [76].

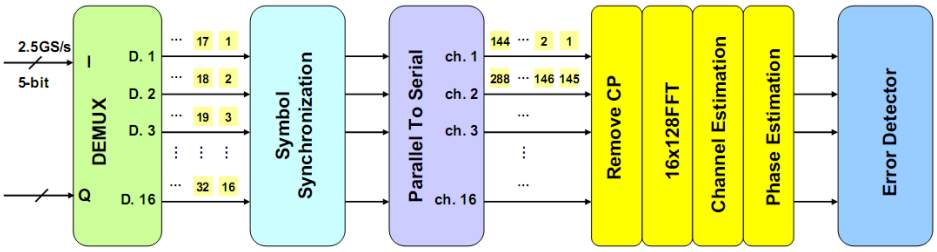

Figure 2.33: Digital signal processing diagram of real-time OFDM receiver. After Ref. [76].

Figure 2.33 shows the block diagram of the real-time receiver. Data streams are fed into FPGA through high-speed serial ports and de-multiplexed to 16 parallel channels. To improve computation efficiency, the cyclic prefix length is equal to the number of the de-multiplexed channels 16. The synchronization pattern is duplicated 16 times so that the synchronization module can still access the synchronization pattern at any one of the de-multiplexed channel. A laser source is split and used as

transmit and local laser to skip frequency offset compensation. A large proportion of FPGA's on-chip memory is used to convert the parallel data into the natural sample order for each parallel lane. After removing the cyclic prefix, 128-point FFT for each channel is performed to convert the signal back to the frequency domain. In the frequency domain, the channel transfer function can be estimated by comparing the received data with the pilot sequences. Finally, the recovered data are compared with transmitted data inside the FPGA to identify the errors.

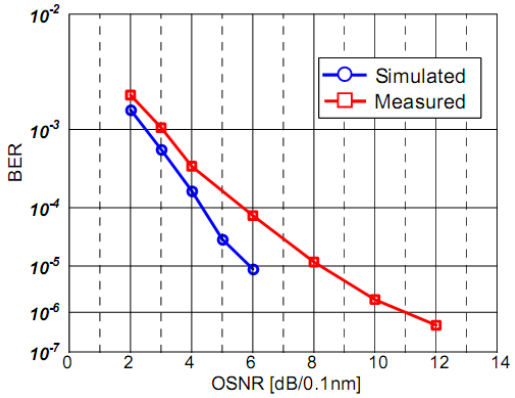

Figure 2.34: Measured BER vs. OSNR of the real-time 3.55-Gb/s CO-OFDM receiver. After Ref. [76].

Figure 2.34 shows the simulated and measured BER as a function of OSNR. A measured BER better than 1×10^{-3} is observed at +3-dB OSNR.

■ ***Real-time Optical OFDM Transceiver***

The first real-time optical OFDM transceiver experimental setup is illustrated in Figure 2.35. The signal processing blocks inside FPGA are shown in Figure 2.36.

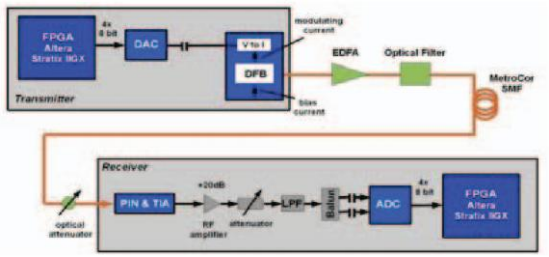

Figure 2.35: Transceiver experimental setup. After Ref. [77].

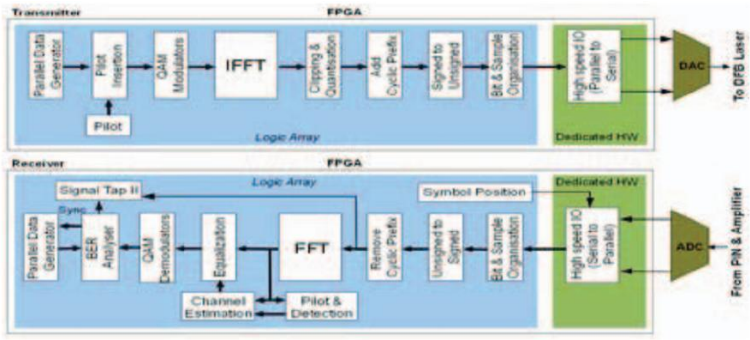

Figure 2.36: Signal processing blocks inside FPGA. After Ref. [77].

The real-time optical OFDM transmitter consists of an Altera Stratix II GX FPGA. 14 parallel PRBS streams are employed as information data. One extra sequence is used for pilot. 32 16-QAM-encoded optical OFDM subcarriers are input to the IFFT block for OFDM modulation. At the output of the IFFT, clipping and quantization are applied to the OFDM frames. A cyclic-prefix is added to each frame, resulting in 40 samples per frame. The analog OFDM signal is generated by the two DACs. The signal is injected into a directly modulated DFB laser to be converted to the optical domain.

At the receiver, the optical OFDM signal is converted back to the electrical domain using a PIN/TIA. The electrical signal is amplified by a RF amplifier and converted to differential through a balun. It is then digitized by an ADC and fed to the second FPGA.

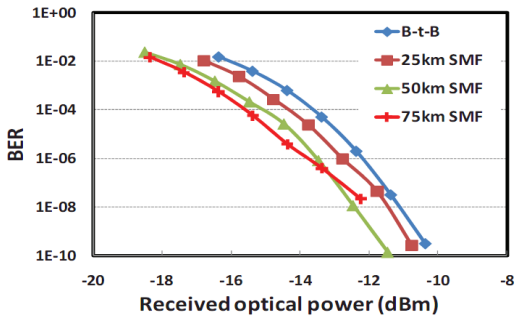

Figure 2.37: BER versus received optical power for 3-Gb/s 16QAM-encoded optical OFDM transmission over DML-based IMDD MetroCor SMFs of different lengths. After Ref. [77].

The measured BER as a function of received optical power is presented in Figure

2.37 for four different scenarios. The record low BERs of approximately 1×10^{-10} are obtained. Whilst in the 75km case, a BER of 3.98×10^{-7} is measured, which is due to the limitation of the maximum optical power received under the current operating conditions. No error floor is observed for all these four cases, indicating high accuracy of the proposed channel estimation technique. It is very interesting to note that negative power penalties are observed. It is due to the fact that the positive transient frequency chirp associated with the DML is compensated by the negative chromatic dispersion parameter associated with the MetroCor fibre.

■ ***Optical FFT Receiver***

The electronic real-time implementation is restricted to several giga-bauds due to the speed limitation of digital signal processors. Higher bit rate OFDM signals are usually processed off-line [7-8]. This is practical for laboratory experiments but cannot be used for practical applications. One method to alleviate the requirement on electronic speed is shifting the FFT into the optical domain.

The optical OFDM transmitter and receiver setup is shown in Figure 2.38. At the transmitter, the data rate limitation for each channel is overcome by using a DWDM-like approach. An optical comb generator provides subcarriers which can be modulated individually. A disinterleaver separates them into even and odd sets. Both sets of subcarriers are then individually modulated with independent DBPSK or DQPSK signals, respectively. They are then combined to form the OFDM signal.

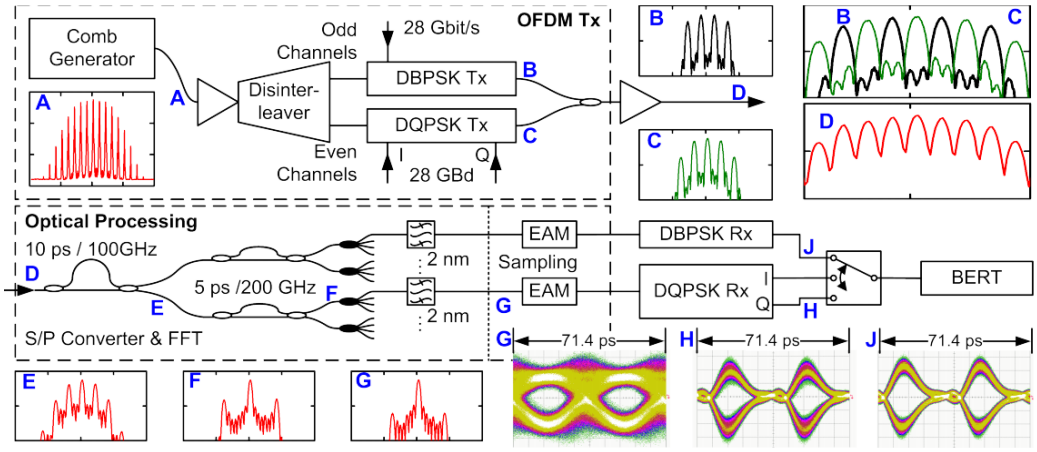

Figure 2.38: Setup of OFDM transmission system. Two cascaded MZMs generate an optical frequency comb "A". Spectrally adjacent subcarriers are modulated differently

using decorrelated DBPSK “B” or DQPSK “C” modulators, respectively. All subcarriers are combined in a coupler and transmitted “D”. The received OFDM signal “D” is processed using the “S/P converter & FFT” (“D”, “E”), where following DI stages are replaced by passive splitters “F” and optical band-pass filters. The resulting signals are sampled by Electro-Absorption Modulators (EAM) “G” and detected using DBPSK and DQPSK receivers. Either eye diagrams “D”, “G”, “H”, “J”, or BER were measured with a BERT. After Ref. [80].

The receiver comprises the all-optical FFT setup and an optical modulation analyser which performs real-time coherent detection and an Error Vector Magnitude (EVM) analysis. The optical FFT setup consists of a cascade of two Delay Interferometers (DIs) followed by passive splitters, band-pass filters and Electro-Absorption Modulator (EAM) sampling gates.

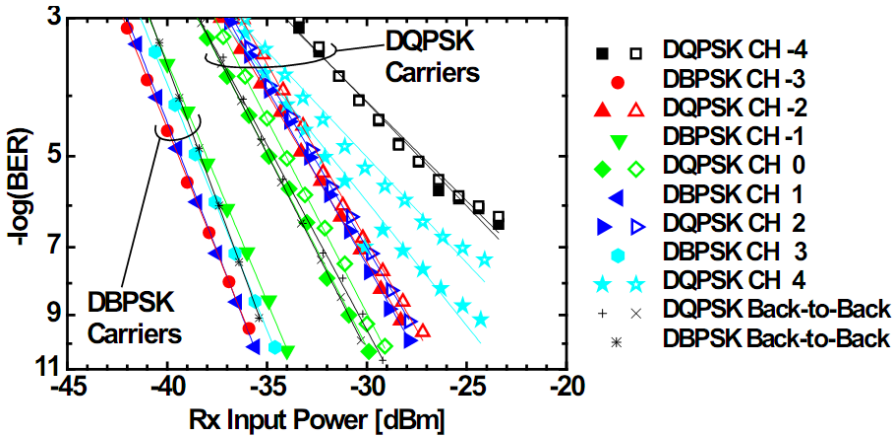

Figure 2.39: BER performance of different subcarriers. After Ref. [80].

The performance of optically processed subcarriers is compared with DBPSK and DQPSK signal in B2B transmission, respectively. The results depicted in Figure 2.39 show no penalty compared to the B2B performance for DBPSK and only a small penalty for the DQPSK channels. The outer channels -4 and 4 perform worse, because their subcarriers have 11-dB less power compared to the central channel.

2.4 I/Q Imbalance Compensation for Optical OFDM

The concept of direct-conversion for frequency translation is proposed because of its

benefits such as low cost and power dissipation. The direct conversion transmitter and receiver remove many off-chip components like Surface Acoustic Wave (SAW) filters which are expensive and take up much space. Unfortunately, in practice some RF impairments of direct conversion transmitter/receiver have been asserted. For example, I/Q imbalance between in-phase and quadrature branches makes mirror subcarrier interference. It is one of main sources of OFDM signal distortions. As the modulation level is higher, performance degradation gets severe.

Even though many I/Q imbalance compensation algorithms have been proposed for OFDM wireless transmission [81-82], only a few experimental reports exits on their application to optical OFDM transmission [83-86].

- ***Transmitter I/Q Imbalances and Bias Deviation Compensation [83]***

A transmitter side I/Q imbalance and optical modulator bias deviation compensation technique for a direct-detected interleaved OFDM system is demonstrated in [83]. The received signal is equalized by a 2×2 matrix which can simultaneously mitigate the interferences resulted from I/Q imbalances and compensate the fibre chromatic dispersion. The concept of compensation scheme is illustrated in Figure 2.40. Figure 2.40(a) is a typical optical I/Q modulator with various imbalances and bias deviation. The I/Q imbalances include (1) amplitude imbalance; (2) phase deviation and (3) time misalignment. The bias deviation means any voltage departure from the optimum bias point.

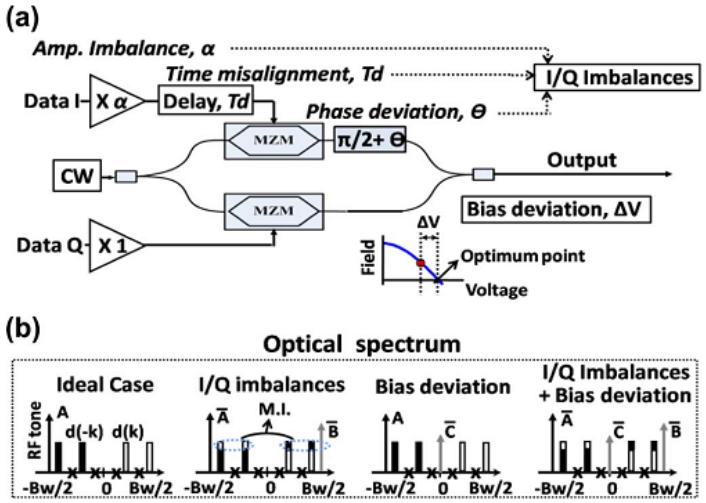

Figure 2.40: (a) Various I/Q imbalances and bias deviation. (b) Optical spectra with I/Q imbalances and bias deviation. M. I.: mirrored interference. After Ref. [83].

The optical spectra of ideal signal and distorted signal are shown in Figure 2.40(b). With I/Q imbalances, the interfered positive subcarrier $\bar{d}(k)$ is polluted by its negative counterpart $d(-k)$, where the bar notation over the subcarrier index is to indicate that the subcarrier is interfered by the imbalances. Similarly, the negative subcarrier $d(-k)$ is interfered by $d(k)$. Additionally, there are now two tones along the signal after I/Q imbalances: (1) the original inserted RF tone and (2) a newly born frequency tone $\bar{B}$, which is the mirror of tone A. The only effect to the optical spectrum due to the bias deviation is the newly induced tone $\bar{C}$ at central subcarrier. The spectrum with both the I/Q imbalances and bias deviation is shown at the rightmost position in Figure 2.40(b). Its effect is a combination of these two interferences.

The transmitted data frames $d(k)$ and $d(-k)$, and the received data frames $y(k)$ and $y(-k)$ relate to each other via a 2×2 channel matrix $\bar{H}$ as Eq. (2.1)

$$\begin{bmatrix} y(k) \\ y^*(-k) \end{bmatrix} = \begin{bmatrix} H_{11} & H_{12} \\ H_{21} & H_{22} \end{bmatrix} \begin{bmatrix} d(k) \\ d^*(-k) \end{bmatrix} \Rightarrow \begin{bmatrix} d(k) \\ d^*(-k) \end{bmatrix} = \begin{bmatrix} R_{11} & R_{12} \\ R_{21} & R_{22} \end{bmatrix} \begin{bmatrix} y(k) \\ y^*(-k) \end{bmatrix} \quad (2.1)$$

The matrix $\bar{H}$ can be estimated by using the training sequences to derive the inverse matrix $\bar{R}$ which is used to equalize the received data. Superscript "*" stands for complex conjugation.

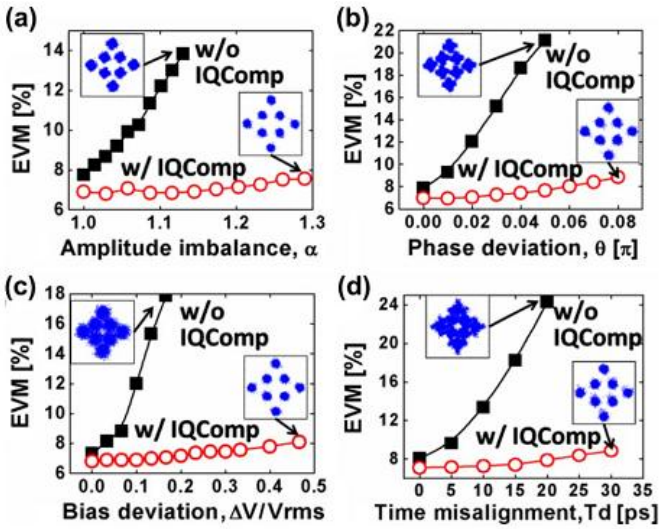

Figure 2.41: (a) EVM versus amplitude imbalance, (b) EVM versus phase deviation, (c) EVM versus bias deviation, where V_{rms} is the root-mean-squared amplitude of the input signal, and (d) EVM versus the time misalignment.

Figure 2.41 depicts the B2B performance in terms of EVM versus amplitude imbalance, phase deviation, bias deviation and time misalignment with and without this compensation scheme. From Figure 2.41 the signal with this technique is insensitive to these deleterious effects, while the signal without I/Q compensation strongly suffers from the imbalance interferences and thus its performance degraded rapidly as the imbalances or the bias deviation increase.

■ ***Receiver I/Q Imbalance Calibration [84]***

In CO-OFDM direct down-conversion receivers, both I- and Q-branch from optical 90 ° hybrid must be strictly matched. Otherwise, the phase difference between I and Q will destroy the desired 90 ° relationship between them [87]. The amplitude imbalance will cause severe penalty as well [87]. A specific algorithm is introduced to compensate the amplitude and phase imperfection. I and Q components of OFDM signal can be written as

$$I_\omega = \frac{A_\omega}{2} + \frac{A_{-\omega}}{2} \tag{2.2}$$

$$Q_\omega = \frac{A_\omega}{2} i\alpha(\omega) e^{i(\phi_H + \phi_{RF}(\omega))} + i\frac{A_{-\omega}}{2} i\alpha(\omega) e^{i(\phi_H - \phi_{RF}(\omega))} \tag{2.3}$$

where I_ω and Q_ω represent I and Q components at frequency ω. A_ω and $A_{-\omega}$ are

frequency components at positive and negative frequency, respectively. ϕ_H and $\phi_{RF}(\omega)$ are phase imbalance from optical 90° hybrid and photodiodes. $\alpha(\omega)$ is I/Q amplitude imbalance factor. ϕ_H, $\phi_{RF}(\omega)$ are equal to zero and $\alpha(\omega)$ equals to 1 without I/Q imbalance interference. The imbalance coefficients ϕ_H, $\phi_{RF}(\omega)$ and $\alpha(\omega)$ are estimated by beating signal laser and local laser with discrete frequency offset ranging from -10 GHz to 10 GHz. Multiple coefficients in different frequency points are collected to fit a curve. The imbalance can be compensated by simply multiplying the inverse of estimated coefficients to OFDM data frames.

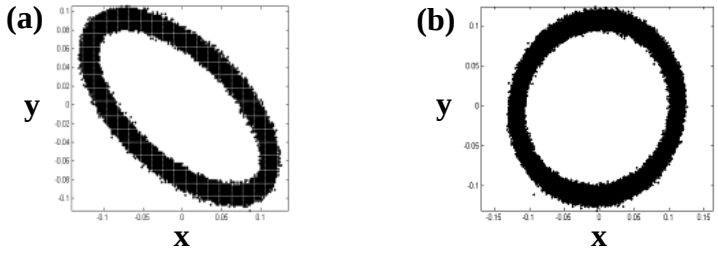

Figure 2.42: The x-y plot for the time domain I and Q signals. (a) before imbalance calibration, and (b) after imbalance calibration. After Ref. [84].

Figure 2.42 compares time domain x-y plot of the I/Q components before and after calibration. The ideal I/Q time domain signal is a perfect circle. Before calibration, an significant imbalance exists resulting in an elliptical shape in the x-y plot. while after calibration it is close to a perfect circle, indicating the effectiveness of the I/Q imbalance calibration.

■ ***Hybrid I/Q Imbalance Compensation [85]***

The proposed hybrid method mitigates both Tx and Rx I/Q imbalance in optical OFDM transmission in the presence of CFO. A low-overhead, orthogonal training sequence based approach is taken for I/Q compensation occurring at the transmitter. A simple, iterative image minimization based approach is taken for calibration of receiver-side I/Q imbalance.

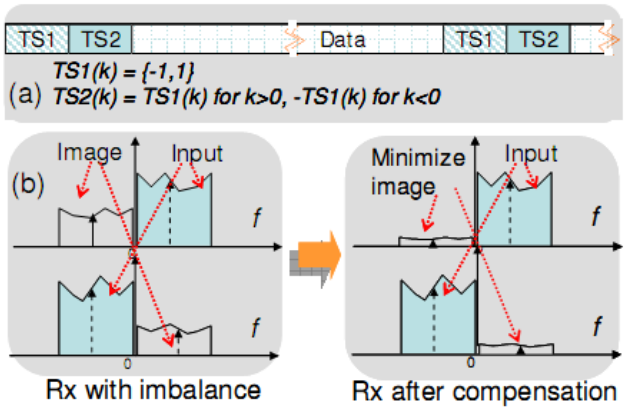

Figure 2.43: (a) Mutually orthogonal training sequences for Tx I/Q compensation, (b) Schematic spectrum showing two input signals for Rx I/Q imbalance adjustment. After Ref. [85].

For the Tx I/Q imbalance compensation, a pair of mutually orthogonal training sequences is inserted between OFDM data frames (Figure 2.43(a)). The frequency dependent amplitude and phase imbalance parameters at Tx can be estimated from the received orthogonal training sequences following the similar formulas as Eq. (2.1).

For frequency-dependent I/Q imbalance at the Rx side, a digital image rejection filter for Rx I/Q imbalance compensation that is independent from Tx I/Q imbalance and CFO is proposed. The compensation filter is implemented by Finite Impulse Response (FIR) filters. An iterative optimization algorithm is used to estimate the required characteristics for the Rx I/Q imbalance. Note that the Tx I/Q imbalance or CFO can be present during the adjustment if the image power measurement range is effectively selected.

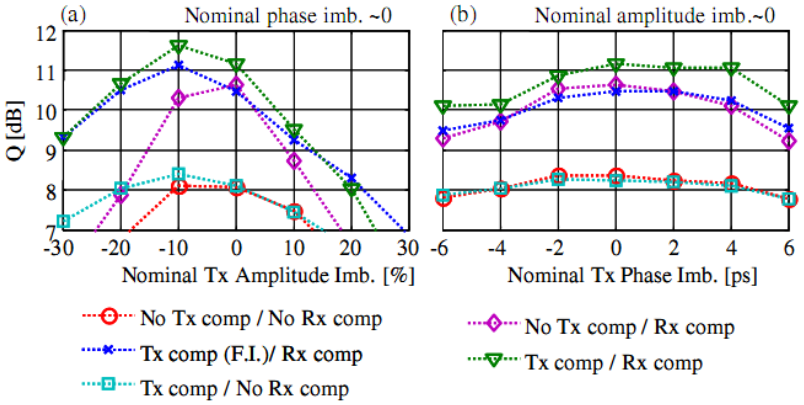

Figure 2.44: Effect of the I/Q imbalances at B2B DDO-OFDM transmission. (a) with intentional amplitude imbalance (phase imbalance minimum). (b) with intentional

phase imbalance (amplitude imbalance minimum).

Figures 2.44(a) and 2.44(b) shows the Q values with respect to the amplitude and phase imbalances, respectively. The received OSNR is set to 34 dB. The frequency dependent Tx and Rx I/Q compensation method shows a better performance than the scenarios without I/Q compensation. It is notable that only apply the Tx I/Q imbalance compensation cannot sufficiently reduce the image interference, which confirms the importance of the hybrid compensation for both Rx and Tx I/Q imbalance.

2.5 Conclusion

Recently, optical OFDM has attracted increased attention as a promising scheme for future optical network. In this chapter, related literature is explored.

In Section 2.2, two types of optical OFDM architectures, DDO-OFDM and CO-OFDM, are introduced. DDO-OFDM is a cost-effective solution and tolerant to laser phase noise, which is more suitable for short reach applications, while CO-OFDM has more spectral efficiency, higher PMD tolerance and OSNR sensitivity, which makes it more suitable for long-haul transmission systems.

FPGA based real-time optical communication systems are reviewed in Section 2.3. This section concerns single-carrier and OFDM modulation formats. Single-carrier modulation is widely used because they are easy to modulate and demodulate. The real-time transmitter, receiver and transponder are discussed in the single-carrier section. On the other hand, the optical OFDM system has attracted a large amount of interest as another transmission scheme. In the OFDM section, demonstrations of real-time transmitter, receiver and transceiver are reviewed. The concept of all-optical OFDM is also introduced to overcome the bandwidth limit of electronic devices.

In Section 2.4, optical OFDM I/Q imbalance compensation schemes for transmitter, receiver and hybrid transmitter and receiver mismatch are reviewed, respectively.

Chapter 3

Fundamentals of Real-time CO-OFDM Systems

3.1 Introduction

Significant progress has been made in theoretical analysis and experimental demonstration on the CO-OFDM area. It brings two powerful techniques, namely coherent optical detection and OFDM, to optical communications. The coherent system provides a much needed linearity in up/down conversion to OFDM while the OFDM provides coherent systems with computation efficiency, and easiness of channel and phase estimation.

The first wave of intense interests on coherent detection appeared in the 1980s and early 1990s when it was viewed as a promising technique to improve receiver sensitivity [88 - 89]. However, the invention of the EDFA reduced coherent communication research interests since the direct detection scheme is simpler and low cost. In recent years, the second wave of research on coherent communications is highlighted by impressive theoretical and experimental demonstrations from various groups around the world [90-95]. The circumstance and technologies in this push are entirely different from the previous one, owing to the rapid technological advancement within the last decade in silicon-based digital signal processing and multi-carrier technology from RF domain. The primary aim of the coherent communication has shifted toward supporting high-speed dynamic networks by simplifying the network installation, monitoring and maintenance. OFDM has been widely studied in mobile communications to combat multi-path reflections and frequency-selective fading. It has been incorporated into wireless network standards (WiFi, WiMax, 3GPP-LTE) and digital audio and video broadcasting (DAB and DVB-T).

In spite of the fact that most of current CO-OFDM experimental reports are

based on off-line signal processing, the FPGA based real-time signal processors have recently been demonstrated for optical OFDM [78]. It signifies that current silicon based high-speed devices can support beyond 40-Gb/s OFDM transmission. With the introduction of next generation high-speed ADCs [18] and FPGAs [21], real-time CO-OFDM is well positioned to be an attractive choice for the next generation 100-Gb/s scale optical transmission.

In this chapter, we first provide an introduction to the OFDM fundamentals in Section 3.2, introducing basic mathematical formulas of OFDM, FFT and CP. Section 3.3 introduces the principle of CO-OFDM from the aspect of system architecture, CO-MIMO-OFDM model, orthogonal band multiplexed CO-OFDM and signal processing for CO-OFDM. Relevant technologies to implement real-time CO-OFDM will be described in Section 3.4. I/Q imbalance model and its compensation will be presented in Section 3.5.

3.2 Principle of OFDM

Conventional single-carrier system modulates information onto frequency, phase, or amplitude of one carrier. A typical single-carrier spectrum is shown in Figure 3.1(a). As higher data rates are used, the duration of each bit becomes smaller. Therefore, the system becomes more susceptible to noise, signal reflections and other impairments. These impairments impede signal recovery. In addition, as the bandwidth used by a single-carrier system increases, the possibility of being interfered by neighbouring signals becomes greater. This type of interference is commonly labelled as frequency interference.

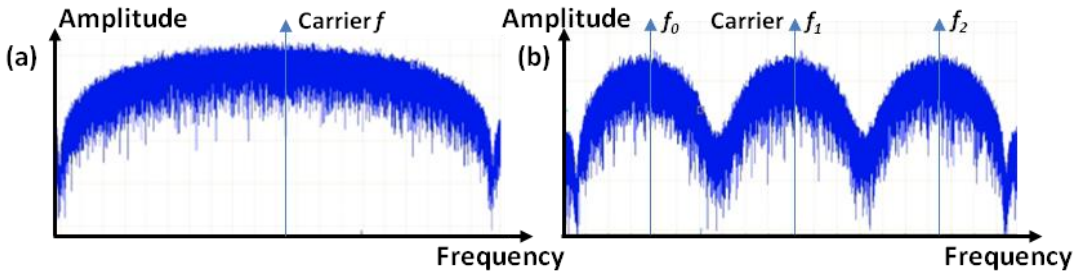

Figure 3.1: (a) a typical spectrum of single-carrier signal and (b) a typical spectrum of

FDM signal. After Ref. [96].

Frequency Division Multiplexing (FDM) extends the concept of single-carrier modulation by using multiple subcarriers within the same channel. The whole data stream is divided into multiple sub-channels. Because different subcarriers share the same transmission media, conventional FDM system has to use extra frequency spacing between each subcarrier to minimize the inter-carrier interference. A typical FDM spectrum is shown in Figure 3.1(b).

OFDM is a special form of FDM. Its subcarrier spacing can be minimized because the subcarriers are orthogonal to each other. For OFDM systems, each subcarrier can be considered non-dispersive because its bandwidth is much narrower than the whole spectrum. Thus, no channel equalization is required. In addition, instead of applying a bank of analog oscillators for each subcarrier at discrete frequencies, OFDM modulation can be conveniently implemented with the aid of FFT as that will be outlined in Section 3.2.2. This principle of orthogonal multiplexing from Chang [39] greatly improves the efficiency of OFDM implementation. Figure 3.2 shows a typical OFDM spectrum. It is observed that subcarriers are heavily overlapped with each other.

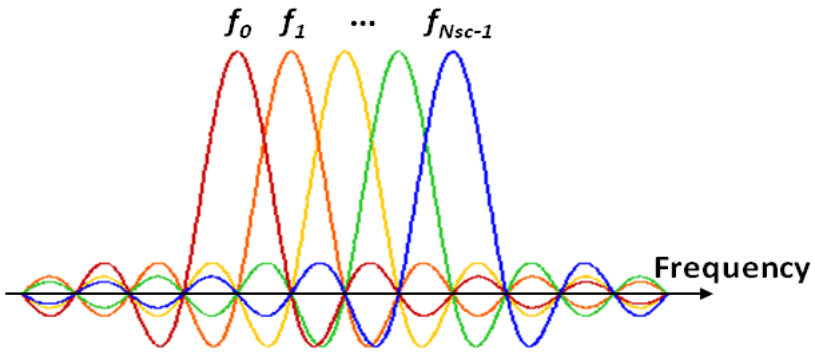

Figure 3.2: OFDM spectrum diagram.

3.2.1 Mathematical Description of OFDM Signal

A typical FDM system consists of N_{sc} electrical up-converters at transmitter with carrier frequencies f_0, f_1, f_2, … f_{Nsc-1}, where N_{sc} is channel number. At the receiver the

same number of down-converters at the same frequency are applied to unload information from carriers. Each transmitted FDM signal can be represented as

$$s_n(t) = A_n(t)e^{j[\omega_n t+\phi_n t]} \tag{3.1}$$

where n is channel index ranging from *0* to N_{sc}*-1*; $A_n(t)$ is the amplitude of transmitted complex data at the nth channel and $\phi_n(t)$ is the phase. To simplify the equation pulse shape function is dropped. The combined FDM signal is

$$s(t) = \sum_{n=0}^{N_{sc}-1} A_n(t)e^{j[\omega_n t+\phi_n t]} \tag{3.2}$$

Traditional FDM uses non-overlapped signal so it requires broader bandwidth than OFDM due to the spacing between two channels. On the contrary, OFDM uses overlapped yet orthogonal subcarrier sets. So if the condition

$$\omega_n = \omega_0 + n\frac{2\pi}{T_s} = \omega_0 + n\Delta\omega \tag{3.3}$$

holds, the correlation will be zero since two subcarriers are orthogonal to each other. In Eq. (3.3), ω_0 is the lowest subcarrier frequency, T_s is OFDM frame period and $\Delta\omega$ is OFDM subcarrier spacing. Therefore, this kind of orthogonal subcarrier set can be recovered without any ICI although they are severely overlapping.

The complex envelop of OFDM frame has the form

$$s(t) = \frac{1}{N_{sc}}\sum_{n=0}^{N_{sc}-1} A_n(t)e^{j[\omega_n t+\phi_n t]} \tag{3.4}$$

This is indeed a continuous signal. If we consider each component of the signal over one frame period, then the variables $A_n(t)$ and $\phi_n(t)$ take on fixed values, which depend on the frequency of that particular carrier, and so they can be rewritten as

$$A_n(t) \Rightarrow A_n$$
$$\phi_n(t) \Rightarrow \phi_n$$

3.2.2 Discrete Fourier Transform for OFDM

Before the theoretical breakthrough on OFDM modulation and demodulation, it suffers from extremely complex structure to generate large quantities of subcarriers by using analog oscillators and filters in the traditional way. In 1971 Weinsten and Ebert

first discovered that OFDM modulation and demodulation can be equal to Inverse Discrete Fourier Transform (IDFT) and Discrete Fourier Transform (DFT) [97]. From then on OFDM signal can be processed in digital domain and the system complexity is largely reduced, which makes this technology widespread.

If OFDM signal is sampled at a sampling frequency of $1/T_s$, then the resulting signal is represented by

$$s(kT_s) = \frac{1}{N_{sc}} \sum_{n=0}^{N_{sc}-1} A_n e^{j[(\omega_0 + n\Delta\omega)kT_s + \phi_n]} \tag{3.5}$$

At this point, the time we analysis this signal has been restricted to N_{sc} samples. It is convenient to sample over the period of one data frame. Thus we have a relationship $t = N_{sc}\, T_s$. Without losing generality by letting ω_0=0, then the Eq. (3.5) becomes

$$s(kT_s) = \frac{1}{N_{sc}} \sum_{n=0}^{N_{sc}-1} A_n e^{j\phi_n} e^{jn\Delta\omega kT_s} \tag{3.6}$$

Now Eq. (3.6) can be compared with the general form of inverse Fourier transform

$$g(kT_s) = \frac{1}{N_{sc}} \sum_{n=0}^{N_{sc}-1} G\left(\frac{k}{N_{sc}T_s}\right) e^{j2n\pi k/N_{sc}} \tag{3.7}$$

In Eq. (3.6), the function $A_n e^{j\phi_n}$ is just a definition of the signal in the sampled frequency domain, and $s(kT_s)$ is a time domain representation. Eq. (3.6) and Eq. (3.7) are equivalent if

$$\Delta f = \frac{\Delta\omega}{2\pi} = \frac{1}{N_{sc}T_s} \tag{3.8}$$

This is the same condition for orthogonality. Thus, one consequence of maintaining orthogonality is that the OFDM signal can be defined by using Fourier transform procedures.

The conventional Fourier transform relates to continuous signals which are unlimited in either time or frequency domains. However, signal processing can be easier if the signals are sampled. Sampling of signals with a finite spectrum leads to aliasing, and signal processing for unlimited data number is actually impossible. To avoid this, Discrete Fourier Transform (DFT) is used in the majority of signal processing [98]. The DFT is a variant of the normal Fourier transform in which the

signals are sampled in both time and the frequency domains. By its definition, the time waveform must repeat continually, and this leads to a frequency spectrum that repeats continually in the frequency domain [97].

3.2.3 Cyclic Prefix for OFDM

The orthogonality of subcarriers in OFDM can be maintained and individual subcarriers can be completely separated by FFT at the receiver when there is no ISI and ICI introduced by channel distortion and CFO. However in practice these conditions cannot be achieved. For example, because the spectra of OFDM signal is not strictly band limited, linear distortion such as multipath cause each subcarrier to spread energy into adjacent channels and consequently cause ISI. A simple solution is to increase the frame duration or the number of subcarriers so that distortion becomes insignificant. However, this method may be difficult to implement in terms of carrier stability, Doppler shift, FFT size and latency. One way to prevent ISI in practice is to create a cyclic prefix/guard interval (Figure 3.3), where each OFDM frame is preceded by a periodic extension of its rear portion. The total frame duration is $T_s=t_s+\Delta G$, where T_s is OFDM frame duration, t_s is observation window and ΔG is cyclic prefix. When the CP is longer than the channel impulse response or multipath delay, the ISI can be eliminated while the ICI still exists. The ratio of CP to the whole OFDM frame duration is application-dependent.

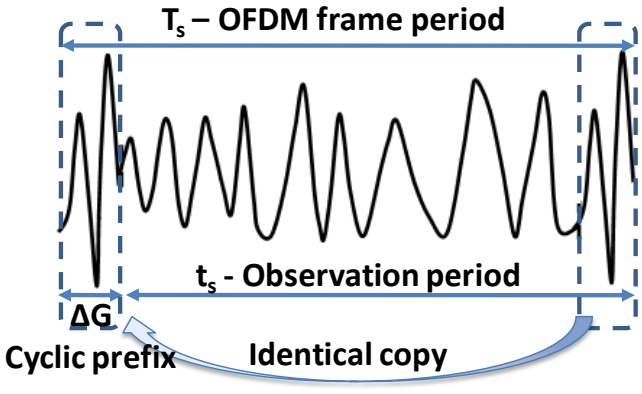

Figure 3.3: Cyclic prefix insertion for time domain OFDM frame.

3.3 Coherent optical OFDM Systems

3.3.1 CO-OFDM System Architecture

The most critical condition for CO-OFDM system is linear modulation, transmission and demodulation since OFDM is more sensitive to nonlinearity than chromatic dispersion [99]. At the transmitter, linear electrical to optical up-conversion can be achieved in two ways: RF I/Q mixer and optical I/Q modulator. By using RF I/Q mixer as shown in Figure 3.4(a), complex OFDM signal will be electrically up-converted to IF then transformed to optical domain with an intensity modulator. The more direct method is to use an optical I/Q modulator. Figure 3.4(b) shows the architecture of optical direct up-convertor with an optical I/Q modulator. The baseband I and Q signals are fed into two RF ports of optical I/Q modulator which is comprised of two MZMs and a 90 ° phase shifter. The I and Q optical signal branches will be combined together at the output of I/Q modulator to form the complex OFDM signal.

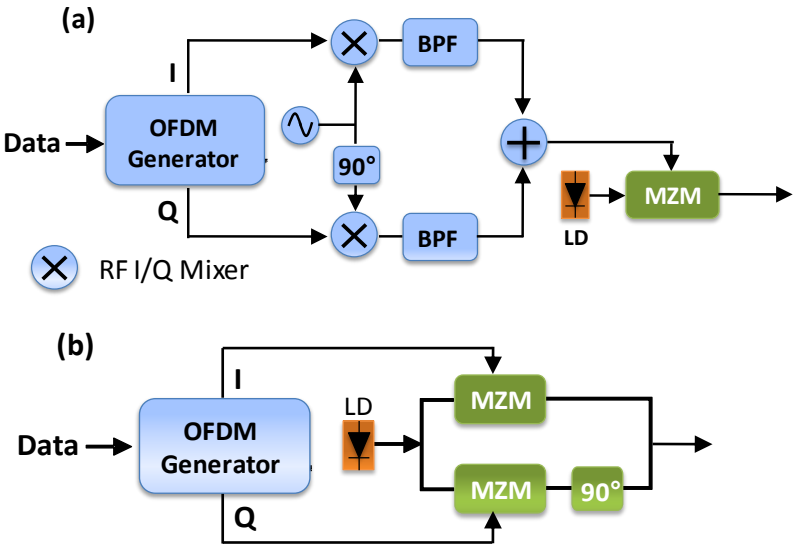

Figure 30.4: Linear conversion from electrical domain to optical domain using (a) an electrical I/Q mixer and an optical intensity modulator or (b) an optical I/Q modulator.

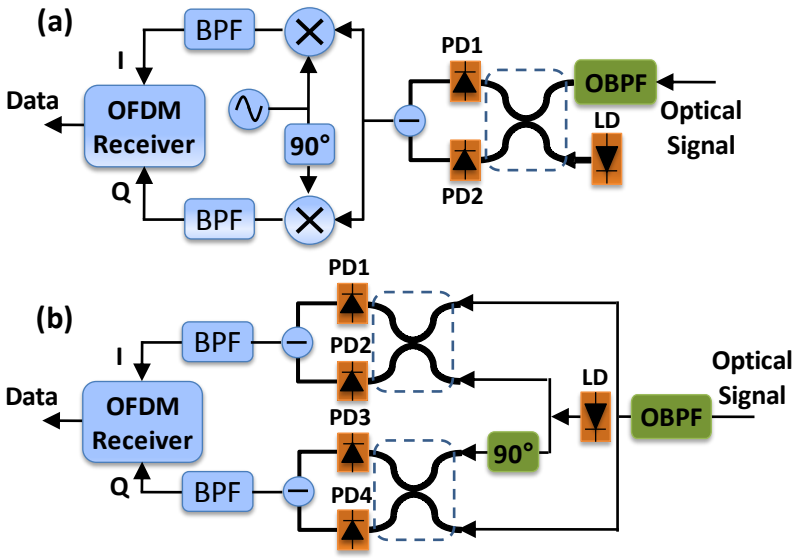

Figure 3.5: (a) heterodyne detection architecture, (b) homodyne detection architecture.

Correspondingly, at the receiver side there are also two types of architectures, IF down-conversion (heterodyne) and direct down-conversion (homodyne). Figure 3.5(a) is the heterodyne convertor architecture. The OFDM signal is first down-converted to electrical IF signal using one balanced photo detector and then further down to baseband via an electrical I/Q mixer. The optical structure is simpler than homodyne with only one balanced receiver and one optical coupler. However, it requires doubled electrical bandwidth and has lower sensitivity compared to the homodyne detection. Figure 3.5 (b) shows the homodyne architecture. It includes two balanced photo detectors, a 90 ° optical hybrid and a local laser. The OFDM spectrum can be directly down-converted to baseband. Although the structure is complicated, the homodyne detection only requires half of the electrical bandwidth and it has 3-dB sensitivity advantage compared with the heterodyne detection.

3.3.2 Coherent Optical MIMO-OFDM Models

It is well known that optical fibre can support two polarization modes. Similar to the single-polarization OFDM signal model, the transmitted OFDM time-domain signal, $s(t)$ is described using Jones vector given by

$$s(t) = \sum_{i=-\infty}^{+\infty} \sum_{k=-\frac{1}{2}N_{sc}+1}^{\frac{1}{2}N_{sc}} \vec{c}_{ik} \Pi(t - iT_s) \exp(j2\pi f_k (t - iT_s)) \tag{3.9}$$

$$s(t)=\begin{pmatrix} s_x \\ s_y \end{pmatrix},\ \ \vec{c}_{ik}=\begin{pmatrix} c_{ik}^{x} \\ c_{ik}^{y} \end{pmatrix} \tag{3.10}$$

$$\prod(t)=\begin{cases} 1 & (-\Delta_G < t \le t_s) \\ 0 & (t \le -\Delta_G, t > t_s) \end{cases} \tag{3.11}$$

where N_{sc} is the number of OFDM subcarriers, $\vec{c}_{ik}$ is transmitted OFDM data frames in the form of Jones vector for the kth subcarrier in the ith OFDM frame, f_k is the frequency for the kth subcarrier, s_x and s_y are two polarization components of $s(t)$, c_{ik}^{x} and c_{ik}^{y} are the two polarization components for $\vec{c}_{ik}$, T_s, Δ_G, and t_s are OFDM frame period, guard interval length and observation period respectively. The Jones vector $\vec{c}_{ik}$ is employed to describe generic OFDM data frames regardless of any polarization configuration for the OFDM transmitter.

A long-enough cyclic prefix is selected to handle fibre dispersion including PMD and CD. This condition is given by

$$\frac{c}{f^2}\left|D_t\right| \cdot N_{SC} \cdot \Delta f + DGD_{\max} \le \Delta_G \tag{3.12}$$

where f is the frequency of the optical carrier, c is the light speed constant, D_t is accumulated chromatic dispersion in fibre link in unit of ps/km, N_{sc} is the number of the subcarriers, Δf is the subcarrier channel spacing, and $DGD_{\max}$ is the maximum budget of Differential-Group-Delay (DGD), which is set to 3.5 times of the mean PMD to have sufficient margin in our experiments.

Using the frequency domain channel transfer function for polarization effects [100], and assuming sufficient long OFDM frame period, the received OFDM frame is given by

$$\vec{c}'_{ki} = e^{j\phi_i} \cdot \boldsymbol{H}(f_k) \cdot \vec{c}_{ki} + \vec{n}_{ki} \tag{3.13}$$

$$\boldsymbol{H}(f_k) = e^{j\Phi_D(f_k)} \cdot \boldsymbol{T}_k \tag{3.14}$$

$$\boldsymbol{T}_k = \prod_{l=1}^{N} \exp\left\{\left(-\frac{1}{2} j \cdot \vec{\beta}_l \cdot f_k - \frac{1}{2}\vec{\alpha}_l\right) \cdot \vec{\sigma}\right\} \tag{3.15}$$

$$\Phi_D\left(f_k\right) = \pi \cdot c \cdot D_t \cdot f_k^2 \Big/ f_{LD1}^2 \tag{3.16}$$

where $\vec{c}'_{ki} = (c'^{x}_{ki} \quad c'^{y}_{ki})^T$ is the received data frame in the form of the Jones vector for the *k*th subcarrier in the *i*th OFDM frame; ϕ_i is the OFDM frame phase noise from signal laser and local laser at transmitter and receiver. It is usually dominated by the laser phase noise; $\boldsymbol{H}(f_k)$ is a 2×2 channel response matrix including CD and DGD; $\vec{n}_{ki} = (n^{x}_{ki} \quad n^{y}_{ki})^T$ is the noise including two polarization components; $\Phi_D(f_k)$ is the phase dispersion owing to the fibre CD; $\boldsymbol{T}_k$ is the Jones matrix for the fibre link; N is the number of PMD/PDL cascading elements represented by their birefringence vector $\vec{\beta}_l$ and PDL vector $\vec{\alpha}_l$ [100]; $\vec{\sigma}$ is the Pauli matrix vector. Eq. (3.13) shows the MIMO model relating the two outputs c'^{x}_{ki} and c'^{y}_{ki} to the two inputs c^{x}_{ki} and c^{y}_{ki}.

The architecture of CO-MIMO-OFDM system can be grouped into four categories according to the number of the transmitters and receivers used in the polarization dimension. They are Single-Input Single-Output (SISO), Single-Input Two-Output (SITO), Two-Input Single-Output (TISO) and Two-Input Two-Output (TITO). The detailed discussion on SISO and TITO is given as follows since they are used in real-time CO-OFDM receptions.

■ ***Single-Input Single-Output (SISO)***

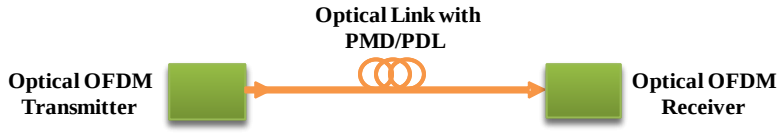

Figure 3.6: SISO CO-OFDM model.

As shown in Figure 3.6, only one optical OFDM transmitter and one optical OFDM receiver are used for transmission. The SISO configuration is susceptible to the polarization mode coupling in the fibre. A polarization controller is required before the receiver to align the polarizations of input signal and local laser. More importantly, in the presence of large PMD, due to the polarization rotation between subcarriers, even the polarization controller cannot function well. This is because there is no uniform subcarrier polarization that the local receiver laser can be aligned to.

■ ***Two-Input Two-Output (TITO)***

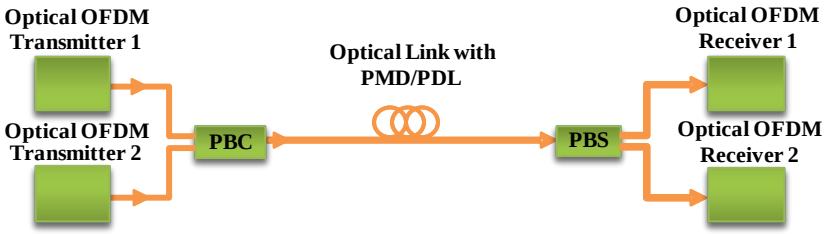

Figure 3.7: TITO CO-OFDM model.

Both a polarization diversity transmitter and a polarization diversity receiver are employed in the TITO scheme, as is shown in Figure 3.7. There are three benefits of applying TITO configuration. Firstly, because the transmitted OFDM data frames can be considered as polarization multiplexed, the capacity is doubled compared with the SISO scheme. Secondly, as the impact of PMD is simply rotating the subcarrier polarization and can be treated with channel estimation and phase estimation, the doubling of the channel capacity will not be affected by PMD. Finally, due to the polarization diversity receiver employed at the receive end, TITO scheme does not need polarization tracking at the receiver.

3.3.3 Orthogonal Band Multiplexed CO-OFDM

As single-carrier optical systems are approaching 100-Gb/s data rate [6], the required analog bandwidth for CO-OFDM to reach the same data rate would be at least 15 GHz. It is not cost-effective to implement the best commercial DACs and ADCs in silicon ICs. To overcome this electrical bottleneck, the concept of Orthogonal Band Multiplexed OFDM (OBM-OFDM) was proposed [24] to divide the entire large bandwidth OFDM spectrum into multiple narrower bandwidth orthogonal bands. Due to the inter-band orthogonality, the multiple OFDM bands with small or null guard bands can be multiplexed and de-multiplexed without inter-band interference. OBM-OFDM has the following advantages: (i) high spectral efficiency can be achieved by allowing zero guard bands and (ii) OBM-OFDM signal can be partitioned with electrical anti-alias Low-Pass Filters (LPFs), and subsequently processed with relatively lower speed DACs/ADCs.

The basic principle of OBM is to partition the whole OFDM band into multiple sub-bands, while maintaining its orthogonal property. As shown in Figure 3.8, the entire OFDM spectrum comprises of N OFDM bands, each with the subcarrier spacing of Δf and band guard spacing of Δf_G. The subcarrier spacing Δf is set to identical for each band to use the same sampling clock. The orthogonal condition between the neighbouring bands is restricted to

$$\Delta f_G = m\Delta f \tag{3.17}$$

which means that the guard band must be multiple (m times) of subcarrier spacing to avoid inter-band interference. By doing so the orthogonality condition is satisfied for any two subcarriers inside the complete OFDM spectrum. In the special case when m equals to 1 the OFDM bands can be multiplexed/de-multiplexed even without guard band, despite the fact that they are originated from different bands.

To detect OBM-OFDM signal, two methods can be used as is shown in Figure 3.8. Firstly, the local laser is tuned to the centre of each sub-band. This sub-band is down-converted to baseband and the other are filtered by "Anti-alias Filter I" LPF. The second way is to tune the local laser frequency to the centre of guard band. Two sub-bands adjacent to this guard band are detected and the others are filtered by "Anti-alias Filter II".

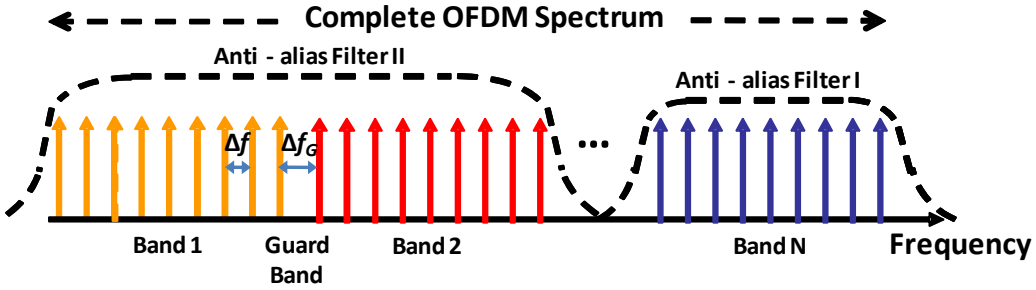

Figure 3.8: Conceptual diagram of OBM-OFDM. Anti-alias filters I and II correspond to two detection approaches illustrated in the text.

OBM-OFDM can be implemented either in electrical or optical domain. In section 4.5 and section 5.4 there are two examples of applying OBM-OFDM both in electrical and optical domain to overcome the limits imposed by ADC bandwidth and

Optical Spectrum Analyser (OSA) resolution. As mentioned earlier, OBM-OFDM technology is particularly suitable to be realized with a mixed signal IC to solve the ADC/DAC bandwidth bottleneck, while the optical realization of OBM-OFDM serves as an alternative to the other spectral efficient multiplexing schemes.

3.4 Real-time CO-OFDM Reception

The critical hardware devices to achieve real-time CO-OFDM reception are high-speed ADCs and FPGAs. They are used to replace the high-speed digital sampling oscilloscope and the combination of computer and signal processing software, for example MATLAB, respectively.

3.4.1 Analog-to-Digital Converter

An ADC is an electronic device that converts an input analog signal to a digital number proportional to the magnitude of the input. The conversion process causes a loss of information. In addition, because digital signals have less accuracy than analog signals, the sampled values may not even be expressed correctly. In mathematics the sampling is described as follows: the input signal is convoluted with an impulse at the sampling time *T*, the output will be the value of the input function at time *T*. Here is the definition:

$$\bar{f}(T) = f(t) * \delta(t - T) \tag{3.18}$$

where $\bar{f}(T)$ is the sampled value at *T*. There are several specifications that decide the performance of an ADC, which is discussed in the following.

■ ***Nyquist Frequency***

One of the most important theorems concerning the sampling process is Nyquist criterion. It relies on the definition of Nyquist frequency. For its definition the frequency range between zero and half of the sampling frequency f_s is defined as the first Nyquist zone and the frequency range from half of f_s to f_s is defined as the second Nyquist zone. When the input signal frequency is larger than f_s, which means its frequency falls inside the second Nyquist zone, the sampled result will appear to be a

low frequency wave, as shown in Figure 3.9. In this figure, the red dots are the sampling points, and the black sinusoid is the input waveform. Notice that since the ADC is sampling too slowly, the recovered signal appears to be the orange waveform, whose frequency is much lower than the correct value.

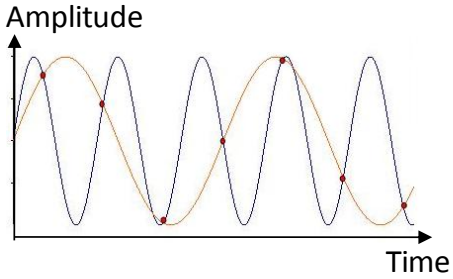

Figure 3.9: Principle of undersampling.

The Nyquist theorem states that a signal must be sampled at a rate greater than twice of its highest frequency to accurately reconstruct the waveform; otherwise, the high frequency content will alias at a frequency inside the spectrum of interest. An alias is a false lower frequency component that appears in sampled data acquired at too low a sampling rate. In real-time CO-OFDM reception, the ADC should be carefully selected that its sampling rate is at least two times higher than the upper limit of subcarrier frequencies.

- ***Analog Bandwidth***

Analog bandwidth describes the frequency range in which the input signal can pass through the ADC with minimal amplitude loss. It is specified as the frequency at which a sinusoidal input signal is attenuated to 70.7% of its original amplitude, also known as the -3 dB point. In real-time application the ADC -3 dB bandwidth is a critical standard for device selection. It should be guaranteed that the -3 dB bandwidth is wider than the input baseband OFDM frequency span.

- ***Resolution***

The resolution of the ADC indicates the number of discrete values it can produce over the range of analog input. The values are usually stored in binary form, so the resolution is usually expressed in bits. Consequently, the number of discrete values is

usually a power of two. For example, an ADC with a resolution of 8 bits can encode an analog input to one of 256 different levels because $2^8 = 256$. The values can represent the range in unsigned integer format from 0 to 255 or in signed integer format from −128 to 127 depending on the application.

■ ***Quantization Error***

The quantization error is a nature product of the analog-to-digital conversion process itself since digital values are discrete. Figure 3.10 shows the transfer functions of an ADC. The diagonal line describes the ideal analog-to-digital transfer function of an ideal ADC with an infinite resolution and the Least Significant Bit (LSB) of this transfer function is infinitesimal. The stair-like curve describes the theoretical transfer function of a 3-bit ADC. The difference between the ideal transfer function and the actual transfer function of ADC with finite resolution is defined as the quantization error. The quantization error is also called quantization noise in literature.

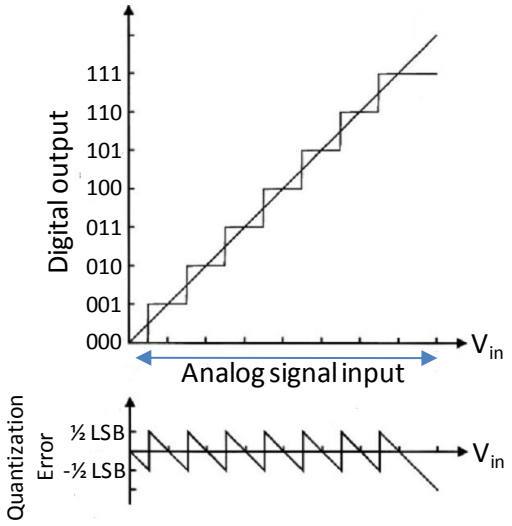

Figure 3.10: Quantization error of 3-bit ADC example.

■ ***Signal-to-Noise Ratio***

The SNR is one of the most important parameters to evaluate the dynamic performance of an ADC. It describes the resolution of the ADC in dynamic range. The theoretical value of the SNR is given by the quantization error. In real ADC other noise sources such as thermal noise and DC power supply may also degrade SNR.

■ ***Harmonic Distortion***

Nonlinearity of ADC results in harmonic distortion when analysed in frequency domain. Such distortion is observed as "spurs" in the FFT spectrum at harmonics of the measured signal. This distortion is referred to as Total Harmonic Distortion (THD).

■ ***Spurious-Free Dynamic Range***

Spurious-Free Dynamic Range (SFDR) is the difference between the magnitude of the measured signal and its highest spur peak. This spur is typically a harmonic of the measured signal but doesn't have to be.

3.4.2 Field-Programmable Gate Array

The FPGA is a semiconductor device that can be configured by the customer or designer in field--hence the name “field-programmable”. FPGA is designed using a logic circuit schematic or a source code in a Hardware Description Language (HDL) to specify how the chip should work. They can be used to implement any logical function that an ASIC could perform, but the ability to reconfigure the functionality after shipping offers advantages for many applications.

FPGAs contain programmable logic components called Configurable Logic Blocks (CLBs), and a hierarchy of reconfigurable interconnects that allow the blocks to be “wired together”. CLBs can be configured to perform complex combinational functions, or merely basic logic gates like AND and XOR.

The most common FPGA architecture consists of an array CLBs, I/O pads and routing channels, as shown in the figure below.

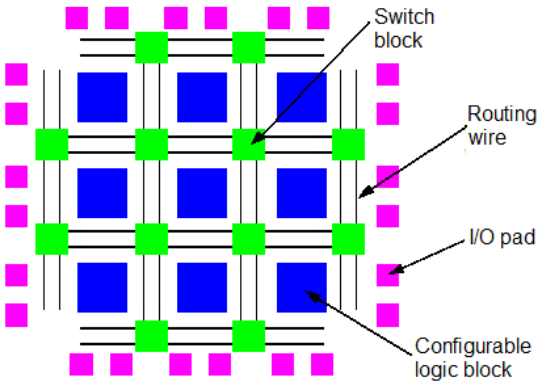

Figure 3.11: A simplified FPGA structure.

Each CLB input pin can be connected to any one of the routing wires in the channel adjacent to it. It is the same case for each CLB output pin. The Figure 3.12 shows the situation clearer. Similarly, an I/O pad can also be connected to any one of the routing wires in the channel adjacent to it.

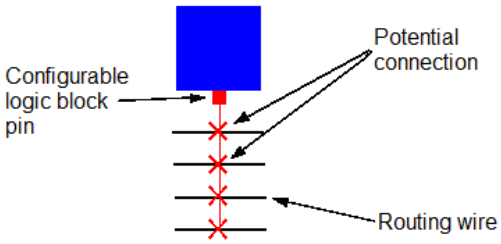

Figure 3.12: CLB pin to routing wire interconnect.

Whenever a vertical and a horizontal channel intersect there is a switch block. In this architecture, when a wire enters a switch block, there are three programmable switches that allow it to connect to three other wires in adjacent channel segments. The pattern, or topology, of switches used in this architecture is the planar or domain-based switch block topology. In this topology, a wire in track number one connects only to wires in track number one in adjacent channel segments, while wires in track number 2 connect only to other wires in track number 2 and so on. The figure below illustrates the connections in a switch block.

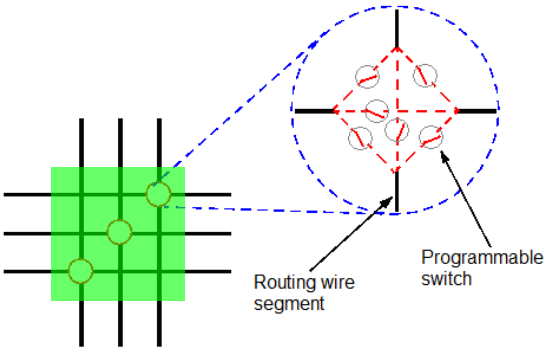

Figure 3.13: Switch block topology.

Modern FPGA families expand the above capabilities to include higher level functionality fixed into the silicon including multipliers, generic DSP blocks, embedded processors, high-speed I/O transceivers and embedded memory blocks. Having these common functions embedded into the silicon reduces the area required and gives those functions increased speed compared to building them from primitives.

To define the behaviour of the FPGA, hardware description languages such as VHSIC Hardware Description Language (VHDL) and Verilog HDL are developed to describe the circuit's operation and verify it. Using an Electronic Design Automation (EDA) tool for FPGA design, a technology-mapped netlist is generated from the HDL. The netlist can then be fitted to the actual FPGA architecture using a process called place-and-route, usually performed by the FPGA vendor's proprietary place-and-route software. The designer will first verify the functionality of this design based on programmed HDL files. Then after the place-and-route process it is further validated based on the generated netlist file for timing analysis. Once the design and validation process is completed, the generated configuration file is used to configure the FPGA to achieve certain functions.

3.5 Principles of I/Q Imbalance

The I/Q imbalance compensation scheme is divided into transmitter (Tx) and receiver (Rx) compensation. The received OFDM signal is first calibrated by Rx compensation scheme in time domain. After FFT, channel estimation and phase estimation, the Tx I/Q imbalance is compensated in frequency domain before OFDM symbol decision.

■ *I/Q Imbalance Model*

Let s and s_{iq} represent the transmitted complex signal vector with FFT length N before and after being distorted by Tx I/Q impairment; r and r_{iq} the received signal before and after being distorted by Rx I/Q impairment; g_t (φ_t), g_r (φ_r) are the amplitude (phase) mismatch between the I and Q branches at Tx and Rx respectively. The distorted transmitted time domain signal can be expressed as

$$s_{iq} = \alpha_t \otimes s + \beta_t \otimes s^* \tag{3.19}$$

$$\alpha_t = (1 + g_t \cdot \mathrm{e}^{\mathrm{j}\varphi_t})/2 \tag{3.20}$$

$$\beta_t = (1 - g_t \cdot \mathrm{e}^{-\mathrm{j}\varphi_t})/2 \tag{3.21}$$

where α_t and β_t are Tx imbalance factors [101].$\otimes$ stands for convolution and * represents complex conjugation.

At the receiver side, the amplitude and phase imbalance are assumed to be frequency independent since the OFDM signal bandwidth is relatively narrow. This simplification decreases Rx compensation performance while it greatly reduces the complexity of real-time implementation because convolution operation is difficult to construct inside FPGA. When carrier frequency offset (CFO) presents together with the receiver I/Q imbalance, the resulting OFDM signal can be simplified [102] as

$$r_{iq} = \alpha_r \cdot r \cdot e^{j \cdot 2\pi \cdot \Delta f \cdot t} + \beta_r \cdot r^* \cdot e^{-j \cdot 2\pi \cdot \Delta f \cdot t} \tag{3.22}$$

$$\alpha_r = (1 + g_r \cdot \mathrm{e}^{-\mathrm{j}\varphi_r})/2 \tag{3.23}$$

$$\beta_r = (1 - g_r \cdot \mathrm{e}^{\mathrm{j}\varphi_r})/2 \tag{3.24}$$

where α_r and β_r are the Rx I/Q imbalance factors and Δf is the CFO.

■ *Rx I/Q Imbalance Compensation*

The Rx algorithm employs the one proposed by Leonardo Lanante Jr. [82]. It requires two identical OFDM training sequences to estimate the I/Q imbalance factors α_r and β_r. The estimation is operated for two times from four consecutive training sequences to increase accuracy. Assuming Rx_1, Rx_2 and Rx_{iq1}, Rx_{iq2} to be the received OFDM frames before and after Rx imbalance distortion, Rx_1 and Rx_2 are equal after removing

cyclic prefix and CFO compensation since they are identical when transmitted. From Eq. (3.22) and its conjugation we can get

$$Rx_1 = \frac{\alpha_r^* \cdot Rx_{iq1} - \beta_r \cdot Rx_{iq1}^*}{|\alpha_r|^2 - |\beta_r|^2} \cdot e^{-j \cdot 2\pi \cdot \Delta f \cdot t} \tag{3.25}$$

$$Rx_2 = \frac{\alpha_r^* \cdot Rx_{iq2} - \beta_r \cdot Rx_{iq2}^*}{|\alpha_r|^2 - |\beta_r|^2} \cdot e^{-j \cdot 2\pi \cdot \Delta f \cdot (t+T)} \tag{3.26}$$

where T is the duration between two training sequences, which is time period of one OFDM frame with CP. As Rx_1, Rx_2 are identical, Eq. (3.25) and Eq. (3.26) can be combined together to be

$$\frac{\beta_r}{\alpha_r^*} = \frac{Rx_{iq1} - e^{-j \cdot 2\pi \cdot \Delta f \cdot T} \cdot Rx_{iq2}}{Rx_{iq1}^* - e^{-j \cdot 2\pi \cdot \Delta f \cdot T} \cdot Rx_{iq2}^*} = \psi \tag{3.27}$$

From definition of α_r, β_r and Eq. (3.27) the Rx I/Q imbalance factors can be estimated by these two training sequences as

$$\Re(\alpha_r) = \frac{1 + \Re(\psi)}{1 + 2\Re(\psi) + \Re^2(\psi) + \Im^2(\psi)} \tag{3.28}$$

$$\Im(\alpha_r) = \frac{\Im(\psi)}{1 + 2\Re(\psi) + \Re^2(\psi) + \Im^2(\psi)} \tag{3.29}$$

$$\Re(\beta_r) = 1 - \Re(\alpha_r) \tag{3.30}$$

$$\Im(\beta_r) = \Im(\alpha_r) \tag{3.31}$$

where the notations $\Re(\cdot)$ and $\Im(\cdot)$ are the real and imaginary components of a complex variable.

Applying the estimated parameters α_r and β_r to Eq. (3.25) for OFDM data payload frames, the Rx I/Q imbalance compensation is finished.

■ ***Tx I/Q Imbalance Compensation***

Assume Rx_5, Rx_6 and Rx_{iq5}, Rx_{iq6} to be two received training sequences before and after Tx I/Q imbalance distortion. In frequency domain Eq. (3.19) can be transformed as

$$Rx_{iq5}(k) = A_t(k) \cdot Rx_5(k) + B_t(k) \cdot Rx_5^*(-k) \tag{3.32}$$

$$Rx_{iq6}(k) = A_t(k) \cdot Rx_6(k) + B_t(k) \cdot Rx_6^*(-k) \tag{3.33}$$

where A_t and B_t are Tx I/Q imbalance factors in frequency domain.

Eq. (3.32) and Eq. (3.33) can be rewritten as

$$\begin{bmatrix} Rx_{iq5}(k) \\ Rx_{iq6}(k) \end{bmatrix} = \begin{bmatrix} Rx_5(k) & Rx_5^*(-k) \\ Rx_6(k) & Rx_6^*(-k) \end{bmatrix} \cdot \begin{bmatrix} A_t(k) \\ B_t(k) \end{bmatrix} \tag{3.34}$$

where *k* is OFDM subcarrier index ranging from 1 to N/2-1.

Replace unknown data Rx with Tx in Eq. (3.34), Tx I/Q imbalance factors A_t and B_t can be estimated as following formula

$$\begin{bmatrix} A_t(k) \\ B_t(k) \end{bmatrix} = \begin{bmatrix} Tx_5(k) & Tx_5^*(-k) \\ Tx_6(k) & Tx_6^*(-k) \end{bmatrix}^{-1} \cdot \begin{bmatrix} Rx_{iq5}(k) \\ Rx_{iq6}(k) \end{bmatrix} \tag{3.35}$$

Tx I/Q imbalance factors A_t and B_t can be estimated as

$$\alpha_t(k) = \frac{Rx_{iq3}(k)Tx_4^*(-k) - Rx_{iq4}(k)Tx_3^*(-k)}{Tx_3\ (k)Tx_4^*(-k) - Tx_4\ (k)Tx_3^*(-k)} \tag{3.36}$$

$$\beta_t(k) = \frac{Rx_{iq4}(k)Tx_3\ (k) - Rx_{iq3}(k)Tx_4\ (k)}{Tx_3\ (k)Tx_4^*(-k) - Tx_4\ (k)Tx_3^*(-k)} \tag{3.37}$$

$$\alpha_t^*(-k) = \frac{Rx_{iq3}^*(-k)Tx_4^*(-k) - Rx_{iq4}^*(-k)Tx_3^*(-k)}{Tx_3\ (k)Tx_4^*(-k) - Tx_4\ (k)Tx_3^*(-k)} \tag{3.38}$$

$$\beta_t^*(-k) = \frac{Rx_{iq4}^*(-k)Tx_3\ (k) - Rx_{iq3}^*(-k)Tx_4\ (k)}{Tx_3\ (k)Tx_4^*(-k) - Tx_4\ (k)Tx_3^*(-k)} \tag{3.39}$$

Applying the estimated Tx I/Q imbalance parameters to received frames according to the following formula

$$\begin{bmatrix} Rx(k) \\ Rx^*(-k) \end{bmatrix} = \begin{bmatrix} \alpha_t(k) & \beta_t(k) \\ \beta_t{}^*(-k) & \alpha_t{}^*(-k) \end{bmatrix}^{-1} * \begin{bmatrix} Rx_{iq}(k) \\ Rx_{iq}^*(-k) \end{bmatrix} \tag{3.40}$$

Then the Tx I/Q imbalance is compensated. It is note that the two training sequences should be carefully designed to hold this condition $Tx_5(k)Tx_6^*(-k) \neq Tx_6(k)Tx_5^*(-k)$.

3.6 Conclusion

In this chapter, the principles of OFDM and CO-OFDM systems, the key devices to implement real-time CO-OFDM reception and I/Q imbalance models are illustrated in detail.

In Section 3.2, OFDM principles including mathematical description, DFT and

cyclic prefix are discussed. The introduction of IDFT/DFT for OFDM modulation and demodulation greatly reduces the transmitter/receiver complexity. The CP insertion preserves the orthogonality of OFDM subcarriers and prevents ISI between successive OFDM frames.

In Section 3.3, the fundamental structure of CO-OFDM system, the linear conversion structures for both transmitter and receiver are shown. After that, MIMO-OFDM model is discussed and SISO and TITO structure are compared. In the third part, the two critical components for real-time application, namely ADC and FPGA are introduced including their major specifications and principles.

In Section 3.5, I/Q imbalance mathematical model is given and two compensation algorithms for Tx and Rx are demonstrated.

Chapter 4

Real-time Single-Input Single-Output CO-OFDM Reception

4.1 Introduction

Optical OFDM has gained substantial interests these years due to high spectral efficiency, receiver sensitivity and polarization-dispersion resilience. In addition to these advantages, the OBM-OFDM technique proposed in [46] alleviates the speed and bandwidth requirement of ADCs which provides more network service flexibility. Experiments with data rates over 100 Gb/s per channel have been demonstrated over hundreds of kilometres of uncompensated standard SMF [7-8]. However, the abovementioned progresses in CO-OFDM are demonstrated using AWG at the transmitter and high-speed DSO at the receiver coupled with off-line processing. In order to go one step further towards the deployment of CO-OFDM in real systems, and to confirm its viability, it is necessary to verify the developing techniques and algorithms in real-time transceivers. OFDM is a primarily digital technique, its modulation and demodulation can be easily implemented by IFFT and FFT completely in the digital domain. Unfortunately its adoption to the optical communications has been dictated by the speed of ADC and DSP. Recently, multi-gigabit per second ADCs have become commercially available, making the real-time implementation of optical OFDM possible. Moreover, the DSP can be implemented at high speeds using multi-million equivalent ASIC gates FPGA which offers both cost-effectiveness and flexibility for the experimental work.

In this chapter, we conduct analysis on signal processing algorithms for each module and its hardware implementation in real-time CO-OFDM receiver. The algorithms for OFDM frame synchronization and carrier frequency offset compensation are totally different from those in off-line mode. Data resolution is

decreased in some modules to save FPGA resource and to maintain the clock rate. Three real-time CO-OFDM systems are then demonstrated. The 3.1-Gb/s reception is the first demonstration in real-time CO-OFDM research area. The RFS is applied to generate multi-band OBM-OFDM signal in the third experiment.

4.2 Real-time Signal Processing Algorithms and Implementation

Figure 4.1 shows the major procedures of a real-time CO-OFDM receiver. The optical OFDM signal is first coherently detected and sampled by the high-speed ADCs. Both I and Q components are fed into the FPGA platform for digital signal processing via high-speed connections such as Low-Voltage Differential Signalling (LVDS).

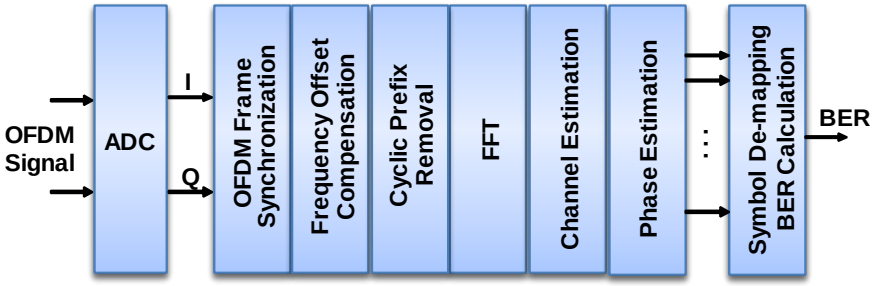

Figure 4.1: Generic signal processing procedures for SISO OFDM.

4.2.1 OFDM Frame Synchronization

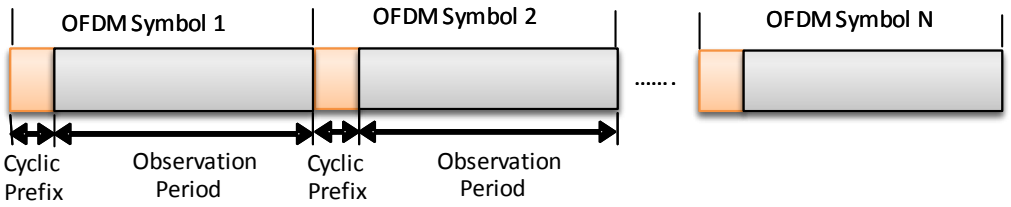

Figure 4.2: OFDM frame time-domain structure.

In this stage, OFDM frames are properly separated to avoid ISI. Figure 4.2 shows the time-domain structure of an OFDM signal consisting of many OFDM frames. Each one comprises a cyclic prefix and an observation period. It is imperative that the start of the DFT window, i.e., observation period, is determined properly, as an improper DFT window will result in ISI and ICI. The most popular data-aided algorithm is the one proposed by Schmidl [103]. In this scheme a pilot sequence or preamble with N_{sc}

samples is transmitted consisted of two identical segments expressed as

$$s_m = s_{m-Nsc/2}, \qquad m \in \left[Nsc/2+1, Nsc \right] \tag{4.1}$$

where s_m is the mth time-domain value of the transmitted signal. Assuming time-invariant channel transfer function $h(t)$, the sampled received signal will have a form of

$$r_m = r\left(mt_s / Nsc \right) = r_m^0 e^{j\Delta\omega m t_s / Nsc} + n_m \tag{4.2}$$

Constant phase across the entire OFDM is assumed. The start of OFDM signal can be identified by applying the following correlation function defined as

$$R_d = \sum_{m=1}^{Nsc/2} r_{m+d}^* r_{m+d+Nsc/2} \tag{4.3}$$

Assuming the frequency offset $\Delta\omega_{off}$ is small, when d=0, the correlation function R_d reaches its maximum value. The correlation function can be normalized to its maximum value given by

$$M\left(d \right) = R_d / S_d, \qquad S_d = \sqrt{\left(\sum_{m=1}^{Nsc/2} \left| r_{m+d+Nsc/2}^2 \right| \right) \left(\sum_{Nsc/2+1}^{Nsc} \left| r_{m+d+Nsc/2}^2 \right| \right)} \tag{4.4}$$

$M(d)$ is defined as DFT window synchronization timing metric. The timing metric takes the maximum value at d=0, namely, at the correct timing.

A Monte Carlo simulation is conducted to evaluate the OFDM frame synchronization using Schmidl's approach for a CO-OFDM system at 10-Gb/s data rate under the influence of CD. QPSK encoding is used for each subcarrier, resulting in total bit rate of 10 Gb/s. The linewidth of signal laser and local laser are assumed to be 100 kHz each, which is close to the actual value of commercially available semiconductor lasers. The optical noise from the optical amplifiers is assumed to be white Gaussian noise and phase noise of laser is modelled as white frequency noise characterized by its linewidth.

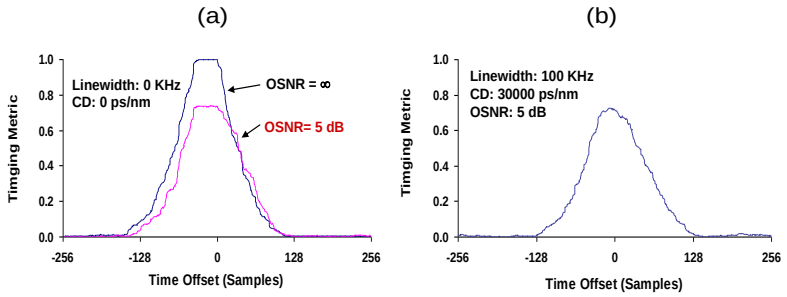

Figure 4.3: Schmidl timing metric for CO-OFDM system at the chromatic dispersion of (a) 0 ps/nm, and (b) 30000 ps/nm.

Figure 4.3 shows that the timing metric will decrease from ideal value of 1 to about 0.7 when OSNR is 5 dB. For reference, to achieve a BER of 10^{-3}, an OSNR of 3.5 dB is needed. Both curves at OSNR of infinity and 5dB show the flat platform of 32 samples under no chromatic dispersion. However, at the chromatic dispersion of 30,000 ps/nm (Figure 4.3(b)), the flat platform has almost disappeared, indicating that most of the guard interval has been affected by the crosstalk from the neighbouring OFDM frames.

The major problem of Schmidl's timing method is that it has a plateau that causes timing uncertainty. To solve this problem several OFDM frame synchronization algorithms in wireless domain are tested in optical channel to find a suitable one for real-time CO-OFDM implementation. This algorithm should be (1) its timing metric should be steep and obvious; (2) it is robust to chromatic dispersion and carrier frequency offset because it is the first stage of real-time signal processing procedure. Minn et al. proposed a method that most fits the requirement [104]. In this scheme, a time-domain preamble that is partitioned into four equal length segments as [B B B –B] is used, where B is generated with IFFT from a Pseudo-random Noise (PN) sequence. Figure 4.4 compares the training sequence structures of Schmidl's approach and Minn's approach.

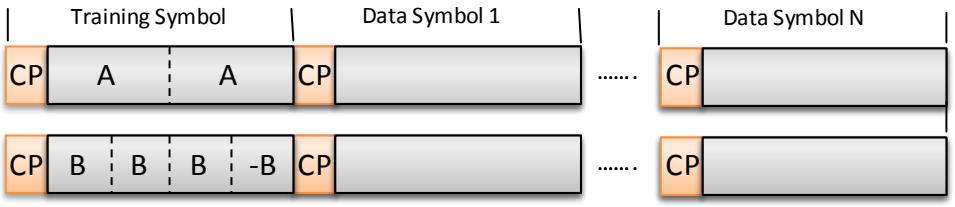

Figure 4.4: Training sequence structure of Schmidl's approach (a) and Minn's approach.

The timing metric at the *d*th sample is expressed as

$$M(d) = \left(\frac{4}{3} \frac{|P(d)|}{R(d)} \right)^2 \tag{4.5}$$

$$P(d) = \sum_{k=0}^{N/4-1} \left[r^*(d+k) r\left(d+k+\frac{N}{4}\right) + r^*\left(d+k+\frac{N}{4}\right) r\left(d+k+\frac{N}{2}\right) - r^*\left(d+k+\frac{N}{2}\right) r\left(d+k+\frac{3N}{4}\right) \right] \tag{4.6}$$

$$R(d) = \sum_{m=0}^{3} \sum_{k=0}^{N/4-1} \left| r\left(d+k+m\frac{N}{4}\right) \right|^2 \tag{4.7}$$

where r represents data sample and * is complex conjugation, N is the length of training sequence. The OFDM frame timing is estimated by finding d which maximizes the timing metric in Eq. (4.5). That is

$$d_i = \arg\{\max[M(d)]\} \tag{4.8}$$

where d_i stands for the optimal timing metric. The timing metric at the peak will be considered as the start of the DFT window and also will be used as an indication for frequency offset estimation.

The comparison of timing metric for Schmidl's and Minn's approach is shown in Figure 4.5. It can be seen that the peak of timing metric from Minn's is sharper and more obvious, signifying that the timing estimation is easy to detect.

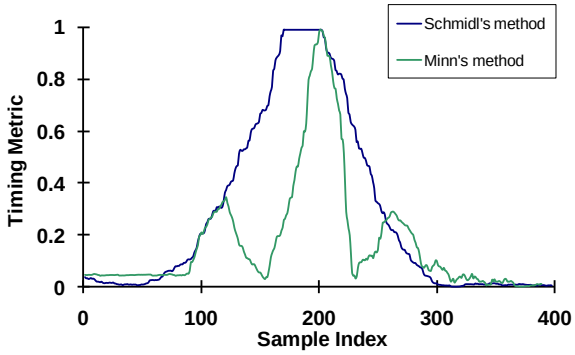

Figure 4.5: Real-time measurement of timing metric for the CO-OFDM signal.

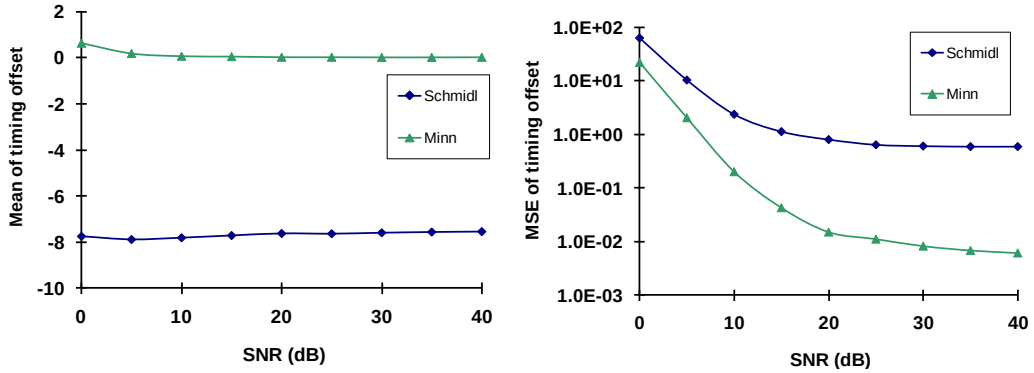

Figure 4.6: Performance of Schmidl's and Minn's timing estimator against CFO.

The performances of the two estimators are evaluated by computer simulation. OFDM system with 128 subcarriers and 16 cyclic prefix is considered and the optical channel model in [13] is used for simulations. Figure 4.6 compares the average and variance of timing accuracy for Minn's and Schmidl's. Figure 4.6(a) shows that the average value of Schmidl's method has shifted to the middle of cyclic prefix, while the value of Minn's estimators is roughly at the correct timing point. From the MSE curve in Figure 4.6(b) it is observed that the Minn's estimators have much smaller MSE than Schmidl's. This improvement can be inferred from the sharpness of the timing metric curve of Minn's approach.

Minn's algorithm is chosen to implement in real-time reception because of its superior performance than Schmidl's, however it requires too much complex multiplication and division operations. The total multiplication of each timing metric value is 1.75N, where N is the FFT length. Suppose N is 64, the integer multipliers required for OFDM frame synchronization is 336 or 448 depend on the structure of

complex multipliers. These numbers take up to 58.3% or 77.7% DSP blocks of Altera Stratix III EP3SL340H1152 FPGA. In addition, complex division takes much more chip resource than complex multiplication. It is clear that the algorithm could not be directly implemented in real-time application before optimization.

The algorithm can be optimized in two aspects:

(1) According to Minn's approach, the start of OFDM frame can be estimated by Eq. (4.5). The square, division and constant multiplication operations can be avoided by using the following equation

$$est = \max[|P(d)| > |R(d)|] \tag{4.9}$$

The $R(d)$ item represents received signal power whose value varies following the input signal amplitude. This benefit makes it suitable to work as the detection threshold of timing estimation because the value of $P(d)$ is also determined by input signal amplitude.

(2) Timing metric can be simplified to the iterative formula

$$\begin{aligned} P(d) = P(d-1) - r^*(d-1)r(d-1+\frac{N}{4}) + 2r^*(d-1+\frac{N}{2})r(d-1+\frac{3N}{4}) \\ - r^*(d-1+\frac{3N}{4})r(d-1+N) \end{aligned} \tag{4.10}$$

This equation can be further simplified by delaying the item $r^*(d-1+\frac{3N}{4})r(d-1+N)$ $N/2$ clocks and $3N/4$ clocks to get the items $r^*(d-1+\frac{N}{2})r(d-1+\frac{3N}{4})$ and $r^*(d-1)r(d-1+\frac{N}{4})$, respectively. In addition, as a left arithmetic shift by n bits is equivalent to multiplying by $2n$, the multipliers required in this new equation is only one. The same method can be used to the calculation of denominator item $R(d)$.

Table 4.1 compares the multiplication and division operation before and after optimization. The training sequence length is set to 64 excluding CP length of 8. It is clear that the multiplier usage sharply decrease into 2% of original number. The system performance before and after simplification is simulated using VPI transmissionMaker. The simulated penalty is less than 1 dB. This penalty can be

reduced by using higher resolution ADCs and larger volume FPGAs.

Table 4.1: Comparison of multiplication/division usage before and after optimization

	Before optimization	After optimization
Multiplication/division operation	112/1	2/0
Multipliers*	336 or 448	6 or 8
DSP block usage**	58.3% or 77.7%	1% or 1.4%

Note: * The number of multipliers required in each multiplication depends on the structure of complex multiplier.

** The total DSP block is set to 576, the total DSP block number in Altera FPGA EP3SL340H1152.

4.2.2 Carrier Frequency Offset Compensation

The frequency offset in OFDM system breaks orthogonality between subcarriers and leads to ICI. For CO-OFDM systems, the frequency synchronization process is envisaged to be divided into two phases that are frequency acquisition phase and a tracking phase [105].

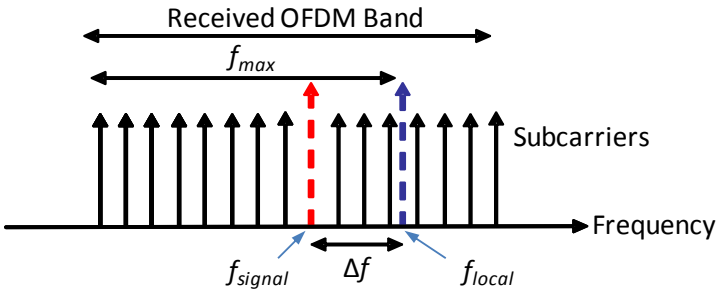

Figure 4.7: Frequency spectrum of the received OFDM signal in relation to the local oscillator laser. f_{signal} and f_{local} are respectively the transmitter and receiver laser frequencies.

Figure 4.7 shows the spectrum of the received CO-OFDM signal in relation to the local laser frequency. The excessive frequency offset Δf brings two problems to the CO-OFDM system: (i) the highest RF frequency (f_{max}) of the RF OFDM signal after direct down-conversion is increased by the amount of frequency offset Δf and (ii) for these signal subcarriers that happen to overlap with local laser will have degraded

performance, due to direct-down conversion DC leakage. The former problem leads to excessive RF bandwidth expansion, therefore increasing the receiver cost. The later problem will be quite challenging for an optical broadcast network. The purpose of the acquisition phase is to first coarse-estimate the frequency offset and brings the receiver laser approximately within one or two times of subcarrier frequency spacing.

The purpose of the frequency tracking is to identify the magnitude of the frequency offset and compensate for it. Various approaches can be used for this purpose. The Schmidl approach can be used for frequency tracking. From Eq. (4.9), we get

$$R_d = \sum_{m=1}^{Nsc/2} \left| r_{m+d} \right|^2 e^{j\frac{\pi f_{off}}{\Delta f}} + o(n) \tag{4.9}$$

where $o(n)$ stands for the residual term with the magnitude in the order of noise component. The offset frequency can be estimated as

$$\hat{f}_{off} = \frac{\Delta f}{\pi} \arg(R_d) \tag{4.10}$$

where $\arg(R_d)$ stands for the angle of the complex value of R_d. Once the frequency offset is estimated, the received sampled signal will be compensated as

$$r_c(t) = \exp\left(-j2\pi \hat{f}_{off} t\right) r(t) \tag{4.11}$$

The algorithm used in real-time signal processing is similar to Schmidl's, expressed as

$$\hat{\varphi} = \arg(P(d)) \tag{4.12}$$

where $P(d)$ has been defined in Eq. (4.6). The maximum estimation frequency range of this estimator is ±2 subcarriers. Then the frequency offset can be estimated as

$$\Delta f = \hat{\varphi} / (\pi T / 2) \tag{4.13}$$

where T is the OFDM frame period.

Once the frequency offset is estimated, the received signal will be compensated as Eq. (4.11).

The COordinate-Rotation-DIgital-Computer (CORDIC) algorithm is used to

calculate the frequency offset angle in vector mode and compensate input data in rotation mode. For both vector mode and rotation mode the CORDIC algorithm can be realized by an iterative sequence of additions/subtractions and bit shift operations, which are rotations by a fixed angle but with variable rotation direction. Due to the simplicity of the operations involved, the CORDIC algorithm is suited for FPGA implementation.

4.2.3 Channel Estimation and Phase Estimation

Assuming successful completion of OFDM frame synchronization and carrier frequency synchronization, the OFDM signal after FFT becomes

$$r_{ki} = e^{\phi_i} h_{ki} c_{ki} + n_{ki} \tag{4.14}$$

where r_{ki} is the ith received OFDM data frame at the kth subcarrier, φ_i is the OFDM frame phase or Common Phase Error (CPE), h_{ki} is the frequency domain channel transfer function, c_{ki} is the transmitted data frame and n_{ki} is the noise.

From the channel model Eq. (4.14), there are three factors that leads to the rotations of the received data frame constellation: (i) the channel dispersion which gives frequency selective dependence across the OFDM spectrum, (ii) the OFDM sampling clock offset will generate phase term that is linear to the subcarrier frequency, and (iii) the phase noises from the signal and local lasers. The orders of magnitude for these three factors are different. The first one changes in the time scale of millisecond which is caused by mechanical vibration. In particular, the CD varies in response to the diurnal temperature fluctuation while PMD varies due to the mechanical and temperature fluctuation. The second item is caused by the sampling clock rate deviation, and may need to be reset every microsecond to tens of microseconds. The third one comes from the laser phase noises with linewidth ranging from 100 kHz to several MHz, which need to be tracked on frame by frame basis. The factors (i) and (ii) are dealt with through channel estimation. The factor (iii) can be compensated through phase estimation and compensation.

The signal processing is operated in blocks each containing a large number of OFDM frames. Within each block, the optical channel is assumed to be invariant,

whereas the frame phase is varying on OFDM frame basis. Subsequently, there are two signal processing procedures which are channel estimation and phase estimation to recover OFDM subcarriers. There are various methods of channel estimation such as time-domain approach and frequency-domain approach. The subcarrier recovery based upon pilot subcarriers or pilot sequences in frequency-domain is employed in real-time implementation. Figure 4.8 shows the two dimensional time/frequency structure for one OFDM block, which includes N_{sc} subcarriers in frequency domain and N_f OFDM frames in time domain. The training frames are added at the beginning to realize OFDM frame synchronization and channel estimation.

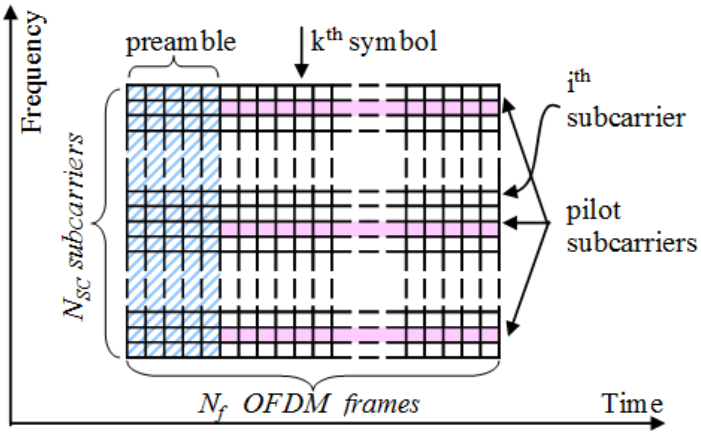

Figure 4.8: Time and frequency representation of a CO-OFDM block.

The channel transfer function h_{ki} can be estimated as

$$\hat{h}_k = \sum_{i=1}^{p} e^{-j\angle r_{k1i}} r_{ki} / c_{ki} \tag{4.15}$$

where $\angle r_{k1i}$ is the angle for the k_1th carrier (an arbitrary reference carrier) in the ith OFDM frame. p is the number of pilot sequences. The additional phase compensation of $-\angle r_{k1i}$ is needed to remove the influence of the CPE. The estimated channel transfer function has uncertainty of a common phase, which can be included in the CPE [105]. The phase estimation is to obtain the CPE primarily due to the laser phase noise. Assume that N_p pilot subcarriers are used for phase estimation, and the maximum likelihood CPE can be estimated as [105].

$$\phi_i = \arg(\sum_{k=1}^{N_p} r_{ki} h_k^* c_{ki}^*) \tag{4.16}$$

Once φ_i and h_{ki} are known, the estimated frame $\hat{c}_{ki}$ is given by zero-forcing method as

$$\hat{c}_{ki} = \frac{h_{ki}^*}{|h_{ki}|^2} e^{-i\phi_i} r_{ki} \tag{4.17}$$

$\hat{c}_{ki}$ is used for symbol decision, in which data frames are subsequently mapped back to the original transmitted digital bits.

The above description of CO-OFDM processing has so far leaved out the pilot sequences and subcarrier insertion where a proportion of the frames and subcarriers in one OFDM block are known values to the receiver. The purpose of these pilot subcarriers is to assist the channel estimation and phase estimation.

The above-mentioned mathematical models have been used in off-line experiments, while optimization is required to make hardware implementation feasible. For example, in off-line programs complex division is widely used while it should be avoided in real-time processing since it takes too much hardware resource and slows down system clock rate. Complex division is replaced by two ways. If the amplitude factor can be neglected and only OFDM symbol phase carriers information, for instance 4-QAM signal, conjugated complex multiplication is transferred to

$$(\mathrm{a} + \mathrm{bj})/(\mathrm{c} + \mathrm{dj}) \Longrightarrow (\mathrm{a} + \mathrm{bj}) \times (\mathrm{c} + \mathrm{dj})^* = (\mathrm{a} + \mathrm{bj}) \times (\mathrm{c} - \mathrm{dj}) \tag{4.18}$$

While if both phase and amplitude factors carrier information, for instance 16-QAM signal, the complex division is converted to a combination of integer multiplication and integer division which are able to implement in FPGA as

$$\frac{a + bj}{c + dj} = \frac{a \cdot c + b \cdot d}{c^2 + d^2} + \frac{b \cdot c - a \cdot d}{c^2 + d^2} j \tag{4.19}$$

4.2.4 Symbol Decision and Error Counting

After all the required synchronization and compensation processing, the next step is to decide what is actually received. This is done by a demodulator that decides the most likely transmitted bits for each received symbol. The decision methods include soft

decision and hard decision, depending on how much information each transmitted bit is produced.

Soft decision is a class of algorithms used to decode data that has been encoded. It requires a stream of "soft bits" where not only 1 or 0 decision is got but also an indication of how certain the decision is correct. On the other hand, a hard decision demodulator makes a definite determination of whether a 1 or 0 bit is transmitted, thus the output of the demodulator are 1s and 0s. Figure 4.9 shows hard decision boundaries for 4-QAM constellation. The boundaries determine how received symbols are mapped to bits. For example, in Figure 4.8, the x mark represents the location of a received symbol. It is closest to the constellation point on the positive I-axis and negative Q-axis, hence the hard decision bits are 11.

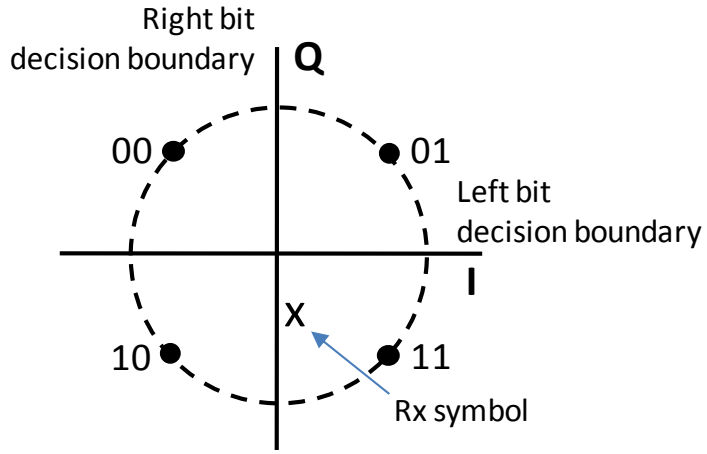

Figure 4.9: Hard decision boundary for 4-QAM constellation.

Hard decision is applied in real-time CO-OFDM reception since it is easier to implement. For 4-QAM optical OFDM signal, the demodulator only requires to judge the sign of received symbol. That is: if the symbol locates at the positive half of I axis then the right bit is 1, otherwise it is 0. This is the same case for Q axis.

After OFDM symbol decision, the recovered bit stream is compared with the transmitted data which is stored inside FPGA ROM. The error bits are counted and collected by the SignalTap II embedded logic analyser from FPGA vendor Altera. The data are exported to computer to calculate BER.

The SignalTap II logic analyser is scalable, easy to use, and is available with the Quartus II EDA software. This logic analyser helps debug an FPGA design by probing

the state of the internal signals in the design without the use of external equipment. The SignalTap II logic analyser does not require external probes or changes to the design files to capture the state of the internal nodes or I/O pins in the design. All captured signal data are stored in device memory and then transported to computer when it is read and analysed.

4.3 3.1-Gb/s Single-band Real-time CO-SISO-OFDM Reception

The first real-time CO-OFDM reception is achieved with 3.1-Gb/s data rate. It is equipped with the ability of receiving 4-QAM and 16-QAM modulation format signals and accumulating error bits to calculate BER data.

4.3.1 Experimental Setup

The experimental setup incorporating the real-time CO-OFDM receiver is shown in Figure 4.10. The transmitted signal is generated by MATLAB program originated from 2^{15}-1 PRBS, and then mapped to 4-QAM or 16-QAM data frames. The time domain signal is formed after IFFT operation, and then inserted with guard interval. The I and Q components of the time signal is uploaded onto Tektronix AWG, which produces the analog signals at 1.4 GSa/s. The total number of OFDM subcarriers is 64; Guard interval is 1/8 of the observation window; 48 subcarriers out of 64 are filled; 4 of them are used for phase estimation; 40 out of 500 OFDM frames are used as training sequences for channel estimation. The resultant data rate of 4-QAM transmissions is 1.55 Gb/s and 3.1 Gb/s for 16-QAM. The net data rate of this experiment is calculated as the follow equation: $1.4 \times 2 \times 8/9 \times 40/64 = 1.556$Gb/s, where the 1.4 (GSa/s) is the ADC sampling rate; 2 is the number of bits per symbol for 4-QAM modulation; since the CP ratio is 1/8, the observation window over the entire OFDM frame is 8/9; 48 out of 64 subcarriers are modulated but 4 are used as pilot tones and the other 4 subcarriers at the centre are skipped to avoid DC leakage. The optical I/Q modulator comprised of two MZM with 90^{o} phase shift, directly up-converts OFDM baseband signals from RF domain to optical domain.

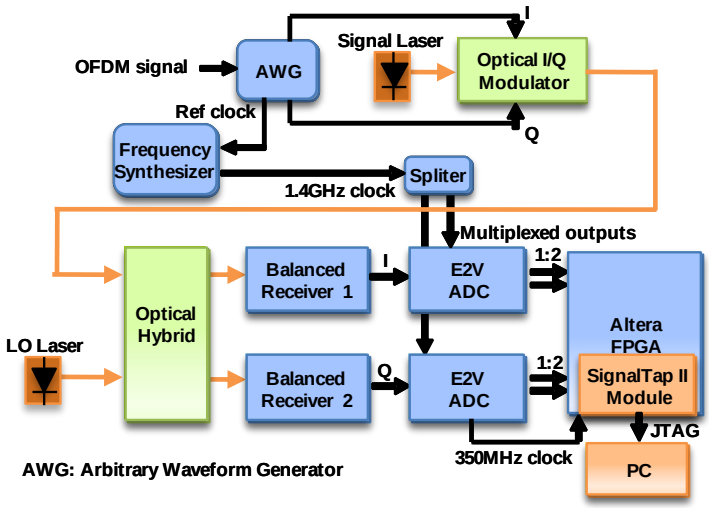

Figure 4.10: Experiment setup for 3.1-Gb/s real-time CO-OFDM receiver.

At the receiver side, direct optical-to-RF down-conversion is employed. We tune the local laser frequency close to that of the incoming signal. Both the signal and local laser are fed into an optical 90 °hybrid. Two balanced receivers are used to detect the I and Q components. The detected RF signals are then sampled with two high-speed E2V ADCs at 1.4 GSa/s. Then the signal is transmitted via LVDS interface onto Altera Stratix III FPGA through 1:2 multiplexed outputs, which lowers the rate down to 700MSa/s. The multiple inputs are received and de-multiplexed into 4 channels at 350MSa/s in the FPGA for further signal processing. After all the OFDM signal processing, the recovered data are compared with transmitted ones in FPGA and errors are counted. This error count, together with transmitted OFDM frame numbers, is then sampled by SignalTap II debugging module and transported via JTAG cable to PC for BER collection.

A synthesizer is employed to receive 10 MHz reference clock from AWG and generate 1.4 GHz sampling clock for two ADCs. FPGA is driven by a 350 MHz clock from one ADC which is derived from its sampling clock input. As such, the clocks in the receiver system are completely synchronized.

4.3.2 Measurement Results and Discussion

The timing metric for the measured real-time data is shown in Figure 4.11. It can be seen that the peak of timing metric is sharp and distinctive, signifying that the timing

estimation is accurate. The peak of timing metric indicates the start of OFDM training sequence. Since the length of training sequence is already known then the start point of data frames can be estimated and each OFDM frame can be separated for further processing.

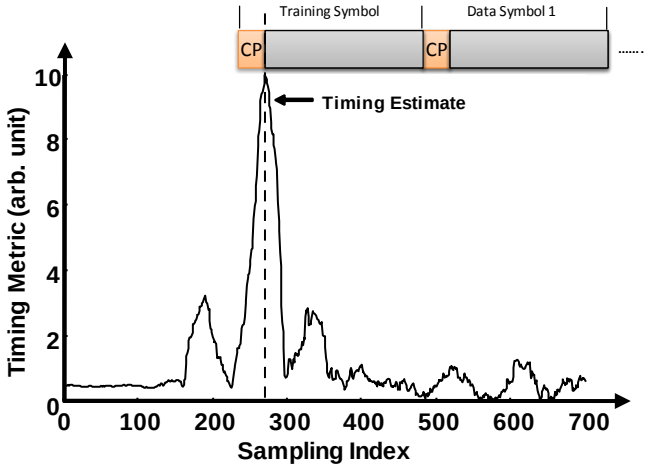

Figure 4.11: Real-time measurement of the timing metric for the CO-OFDM signal.

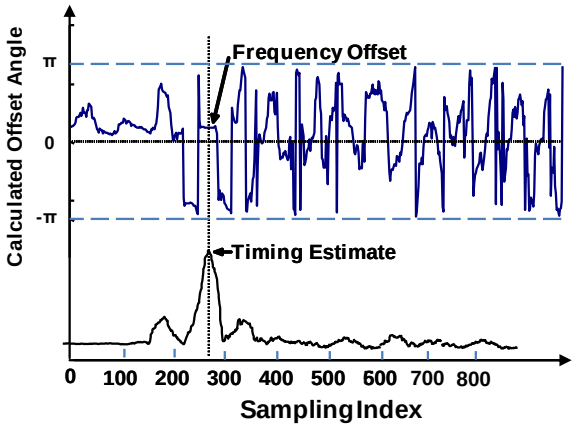

Figure 4.12: Real-time measurement of frequency offset estimation for the optical OFDM signal.

Figure 4.12 shows the estimated frequency offset angle against the sampling index with the frequency offset normalized to $2/(\pi T)$. As 18-bit resolution is used, the output range is from -2^{17} to $2^{17}-1$, which represents $-\pi$ to π respectively. Once the timing estimate signal from OFDM frame synchronization stage is received, the current output value of Eq. (4.12) is the correct frequency offset.

The estimated phase noise as a function of OFDM frames is demonstrated in

Figure 4.13. The abrupt phase jump is due to the 2π phase wrap.

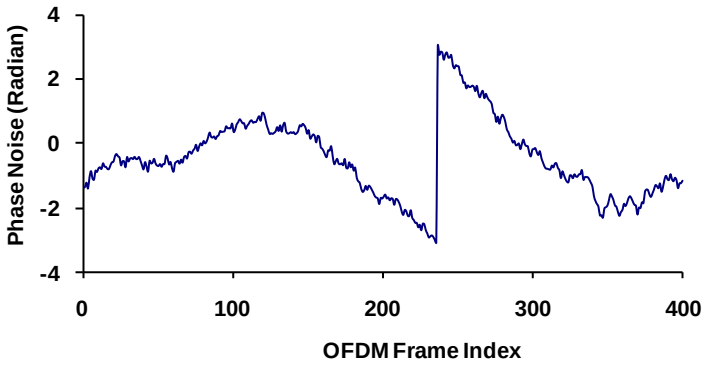

Figure 4.13: Real-time phase noise as a function of OFDM frame sequence for 3.1-Gb/s real-time reception.

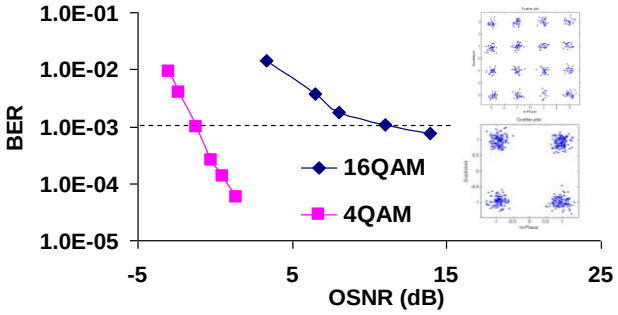

Figure 4.14: The real-time BER performance for 1.55-Gb/s 4-QAM and 3.1-Gb/s 16-QAM CO-OFDM signal at back-to-back transmission.

Figure 4.14 shows the BER performance of 1.55-Gb/s 4-QAM CO-OFDM signal at the back-to-back transmission. Each point in this figure is an average of 50 OFDM transmission blocks each containing 368 OFDM data frames. The combined laser linewidth is about 100 kHz. A BER of 10^{-3} can be observed at an OSNR of -2 dB (ASE noise bandwidth of 0.1 nm) for 4-QAM signal. The obtained data rate is limited to 1.55 Gb/s due to the maximum sampling rate of 1.4 GSa/s offered by the ADC used. The choice of only filling 46 subcarriers out of 64 is due to 550-MHz anti-alias filter used. By accessing a higher sampling rate ADC or using the polarization multiplexing can further improve the data rate. We also show the performance of 16-QAM in Figure 4.14. The BERs better than 10^{-3} is achieved at high OSNRs. The BER floor for 16-QAM is attributed to the limited 7-bit ADC resolution, and large phase drift due to

long OFDM frame length by using a relatively low sampling rate of 1.4 GSa/s. This can be avoided to use ADC with higher sampling rate. Nevertheless, this demonstration has achieved the record data rate of 3.1 Gb/s when this paper [75] was published for real-time reception of coherent OFDM signal, in either RF domain or optical domain.

4.4 12.1-Gb/s Single-band Real-time CO-SISO-OFDM Reception

Limited sampling speed of ADCs constrains the improvement of single-band data rate for real-time CO-OFDM receiver. In some demonstrations high received data rate is achieved by combining several relatively low speed (<10-Gb/s) OFDM bands [25]. With the advancement of silicon technology, high-speed ADCs beyond 3 GSa/s are now commercially available. By using these devices the bottleneck of 10 Gb/s net data rate for single-band reception can be overcome. Although the 10-Gb/s real-time OFDM reception has just been reported [106], it uses direct-detection scheme. In this experiment a demonstration of FPGA based single-band real-time CO-OFDM receiver at a raw data rate of 12.1 Gb/s is shown. The resultant BER is better than the FEC threshold of 2×10^{-3}. To the best of our knowledge, this is the record real-time single channel data rate for a CO-OFDM reception when the paper [107] was published.

4.4.1 Experimental Setup

The experimental setup of single-band 12.1-Gb/s real-time CO-OFDM reception is shown in Figure 4.15. The transmitted data stream consisting of PRBS of length 2^{15}-1 is mapped onto 128 subcarriers with 16-QAM modulation. The time-domain digital baseband OFDM signal is generated via 256-point IFFT. Only the middle 128 subcarriers out of 256 subcarriers are filled with 16-QAM symbols and the rest one left blank. The analog time-domain OFDM signal is generated with an AWG at 6.8-GSa/s. The total number of OFDM frames in each block is 257 with 1 training sequence for frame synchronization, and 16 training sequences for channel estimation, the remainder for data. Cyclic prefix is set to be 1/16 of the observation window; 4 of

filled subcarriers are used for phase estimation; The base-band RF signal is then directly up converted to optical domain through an optical I/Q modulator. The transmitted OFDM signal parameters are listed in Table 4.2 and the output signal spectrum is shown in inset of Figure 4.15.

Table 4.2: OFDM system parameters

Parameter	Value
AWG sampling rate	6.8 GSa/s
ADCs sampling rate	3.4 GSa/s
OFDM frames per block	256
Subcarriers per frame	128
Cyclic prefix	8
Samples per frame	136
Pilot tones	4
Modulation format	16 QAM

At the receiver side, direct optical-to-RF down-conversion is employed. The signal laser at the transmitter and the local laser at the receiver are originated from the same External-Cavity Laser (ECL) with 100-kHz linewidth through a 50:50 coupler with one branch delayed by 2-km optical fibre to get uncorrelated optical signal. In this setup frequency offset estimation and compensation can be avoided in order to fit the whole design in one FPGA chip. The detected RF signals are fed into 3.8-GHz anti-alias LPFs, and then sampled with two high-speed ADCs at 3.4-GSa/s with 7-bit resolution. By using this configuration, all of the 128 modulated subcarriers in the middle of 6.8-GHz span can be employed and 12.1-Gb/s net data rate is achieved.

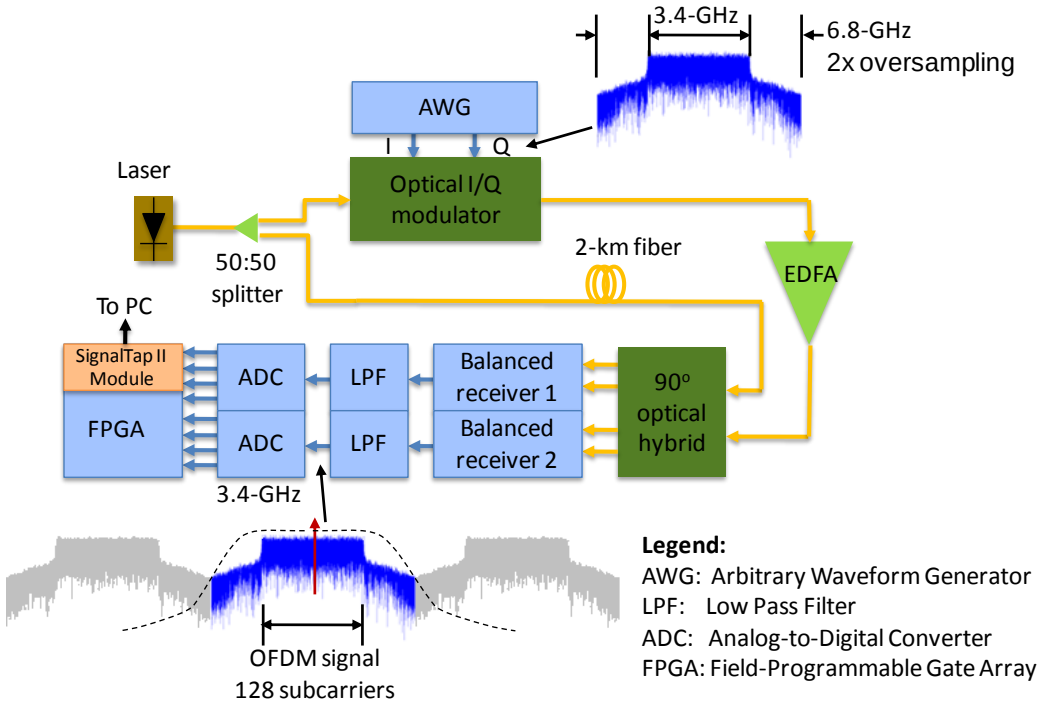

Figure 4.15: Experimental setup for 12.1-Gb/s real-time CO-OFDM reception.

The digitalized signal is transmitted via LVDS interface onto FPGA through 1:8 multiplexed outputs, which lowers the rate down to 425-MHz. The multiple inputs are received and de-multiplexed into 16 channels at 212.5-MHz in the FPGA for further processing. After all the OFDM signal processing, the recovered data are compared with transmitted ones in FPGA and the errors are counted. This error count, together with transmitted OFDM frame numbers, is sampled by SignalTap II debugging module and transported via JTAG cable to PC for BER collection.

The CO-OFDM receiver signal processing procedure is divided into six stages, the same as the 3.1-Gb/s real-time reception [75] except carrier frequency offset compensation: (1) OFDM frame synchronization; (2) CP removal and parallel-to-serial conversion to recover time-domain OFDM frames; (3) FFT to recover the frequency-domain symbols; (4) channel estimation; (5) phase estimation; (6) symbol decision, error accumulation and BER computation. The frame synchronization module is discussed in detail below:

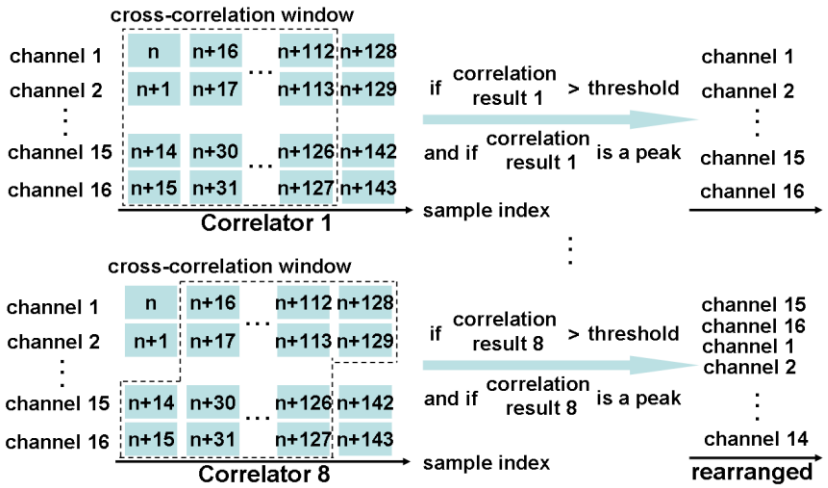

Figure 4.16: Principle of frame synchronization and channel order rearrangement for 12.1-Gb/s experiment.

At the first frame of each block a 272 length ((128+8)*2 because of transmitter 2 oversampling) training sequence is transmitted with its value randomly selected from the set of (1, -1). At the receiver side, the received data are cross-correlated with the training sequence. In FPGA this correlation operation is implemented by addition and subtraction so complex multiplication is removed and large chip area is saved.

Since the high-speed sampled data are de-multiplexed into 16 parallel channels, estimating the exact frame beginning would involve heavy computation for all channels. To solve this problem, cross-correlation window slides every two samples, which means that only 8 correlators are needed. The principle of synchronization scheme is demonstrated in Figure 4.16. By performing the cross-correlation, the resulting sharp peak indicates the beginning of each block. Once the starting point is obtained, the channel order requires to be rearranged if correlation result 1 isn't the peak.

4.4.2 Measurement Results and Discussion

The real-time CO-OFDM receiver uses 78% of DSP block elements, 27 % of Look-Up Tables (LUTs), 37% of dedicated registers and 8% of memory of the FPGA chip (Altera Stratix III EP3S340H1152).

Table 4.3 shows the BER performance comparison of 12.1-Gb/s 16-QAM

OFDM signal for optical back-to-back (data sampled by ADCs) and electrical back-to-back (data sampled by ADCs and Tektronix TDS6154C oscilloscope respectively) transmission.

Table 4.3: BER performance comparison between electrical B2B and optical B2B

Optical back-to-back (by ADCs)	1.9×10^{-3}
Electrical back-to-back (by ADCs)	6.5×10^{-4}
Electrical back-to-back (by Scope)	2.1×10^{-5}

The BER of OFDM signal sampled by ADCs is 1.9×10^{-3}, better than the FEC threshold of 2×10^{-3}, or error free data would be obtained after FEC. As the optical back-to-back performance is not as good as theoretical estimation, we further test electrical back-to-back result to locate the reason of degradation. From rows 2 and 3 of Table 4.3 it is obvious that the sampled data quality from oscilloscope is much better than that from ADCs as the BER for the former is over ten times lower than the latter. Two factors are attributed to this degradation.

(1) In the setup, analog input and clock input are both single-end driven. This type of operation will degrade ADC performance significantly [108-109]. It is highly recommended to use a differential source to drive the analog inputs to ADC. The following figures compare the spectrum of sampled data from ADCs. The SFDR of single-end drive signal is just up to 16 dB while that of differential driving can reach around 30 dB.

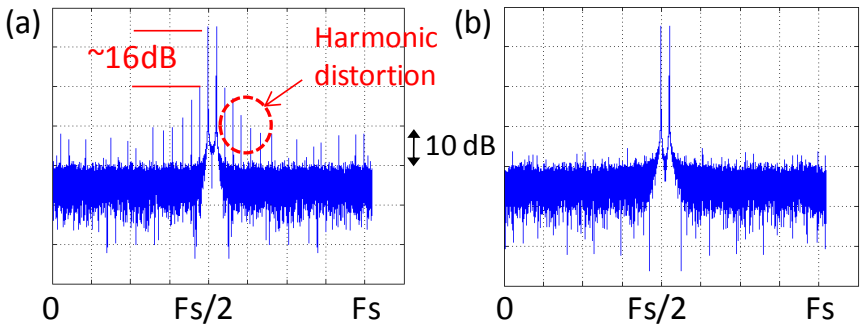

Figure 4.17: Comparison of spectrum from the ADCs with single-end drive (a) and differential drive (b).

(2) These two ADCs can achieve better accuracy by further calibration such as the items of DC offset and Integral Non-Linearity (INL).

4.5 110-Gb/s Multi-band Real-time CO-SISO-OFDM Reception

It is difficult to improve data rate by increasing the sampling rate of ADCs with the limit of silicon technology. Multi-band OFDM has been proposed to alleviate bandwidth constraint of ADC and it has been shown that a part of the OFDM spectrum can be carved out and detected at a fraction of the overall data rate [24]. A multi-band 54-Gb/s real-time CO-OFDM reception has been demonstrated [25]. However in [25] the signal and local lasers are derived from the same source so only the central sub-band on each tone can be recovered. In addition, the sub-band spacing is set to 62 subcarriers which reduce the spectrum efficiency. In this experiment, a demonstration of Recirculating Frequency Shifter (RFS) generated multi-band real-time CO-OFDM receiver at a data rate of 110 Gb/s is provide by characterising the performance of its sub-band.

4.5.1 Principle of Recirculating Frequency Shifter

The architecture of the RFS, which consists of a closed fibre loop, an optical I/Q modulator, two EDFAs to compensate the frequency conversion loss and a tuneable band-pass filter with a flat-top shape to restrict the number of optical tones, is shown in Figure 4.18(a).

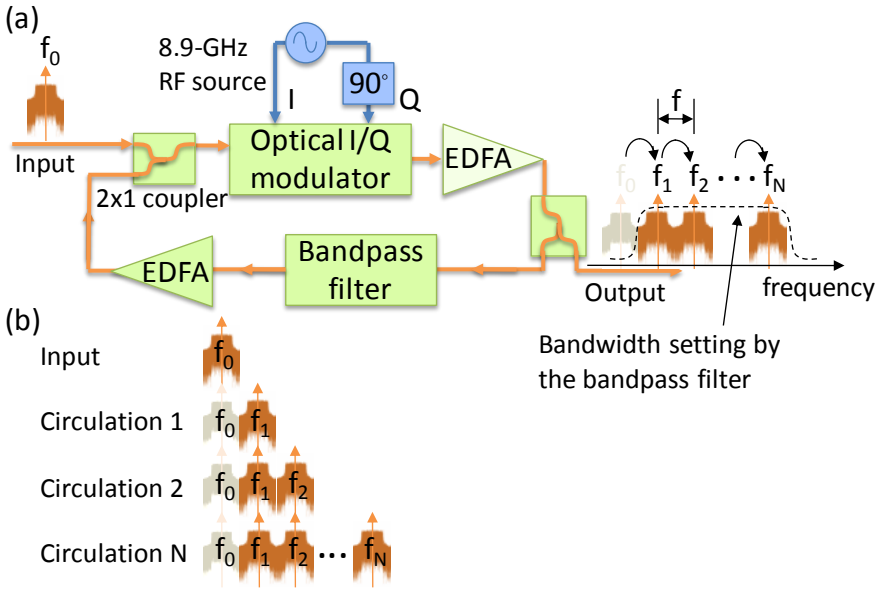

Figure 4.18: (a) Architecture of RFS as a multi-tone generator; (b) Illustration of replication of OFDM bands with a RFS.

The OFDM signal at the input of the I/Q modulator for the first circulation can be expressed as

$$E_{in1}(t) = S_B(t) \cdot e^{j \cdot 2\pi f_0 t} \tag{4.19}$$

$$S_B(t) = \sum_{k=-(N_{sc}/2)+1}^{k=N_{sc}/2} c_k e^{j \cdot 2\pi k f_k t},\ f_k = (k-1)/t_s \tag{4.20}$$

N_{sc} is the total number of OFDM subcarriers, f_k is the frequency of the kth subcarrier and t_s is the OFDM frame period. Then the output of the I/Q modulator can be written as [110]

$$E_{out1}(t) = \frac{1}{4} \cdot S_B(t) e^{j \cdot 2\pi f_0 t} \sum_{n=-\infty}^{\infty} e^{j \cdot 2\pi n f t} \sum_{i=1}^{4} J_n A_i^{RF} P_{n,i} A_i^{Opt} \tag{4.21}$$

where f is the drive voltage frequency, i represents one of 4 optical paths inside the I/Q modulator, J_n is the nth-order first kind Bessel function, A_i^{RF} is the optical phase induced by RF drive voltage in path i which is proportional to the amplitude of RF signal, A_i^{Opt} is the optical amplitude in path i. Eq. (4.21) shows there exists many optical harmonics denoted as $f_0 + nf\,(n = 0, \pm 1, \pm 2 \ldots)$. $P_{n,i}$ is expressed as

$$P_{n,i} \equiv \exp j \cdot [(Y - Xn)\, j\frac{\pi}{2} + \Delta\phi_i^{Opt} + n\Delta\phi_i^{RF}] \tag{4.22}$$

$$\phi_i^{Opt} = Y\frac{i \cdot \pi}{2} + \Delta\phi_i^{Opt} \tag{4.23}$$

$$\phi_i^{RF} = -X\frac{i\pi}{2} + \Delta\phi_i^{RF} \tag{4.24}$$

$$X = \pm 1, \quad Y = \pm 1 \tag{4.25}$$

ϕ_i^{Opt} and ϕ_i^{RF} are phases of optical and RF signal for path i. $\Delta\phi_i^{Opt}$ and $\Delta\phi_i^{RF}$ are the noise terms of the corresponding phases for imperfect single side band condition. Since the phase shifter is well justified that two branches of RF signal with 90 °phase difference are fed into the I/Q modulator, the noise terms can be set as 0 and the optical and RF phases are 0, 90 °, 180 °, 270 °. The third order harmonic is the most dominant among all the harmonics and ultimately limits the single side band conversion efficiency. Ignoring all the high order harmonics beyond the third order, the output of the I/Q modulator with $X \times Y$=1 can be rewritten as

$$E_{out1}(t) \approx A^{Opt} \cdot S_B(t) \cdot e^{j\cdot 2\pi f_0 t} \cdot \tilde{V}(t) \tag{4.26}$$

$$\tilde{V}(t) = J_1 A^{RF} e^{j\cdot 2\pi f t} - J_3 A^{RF} e^{-j\cdot 2\pi\cdot 3 f t} \tag{4.27}$$

J_1 term represents the upper side band at the frequency of $f_1 = f_0 + f$ and is the dominant component. J_3 term is the third order harmonic and J_1/J_3 is defined as the extinction ratio of the I/Q modulator. We will concentrate on the shifted tone only and ignore the newly input optical signal as the last tone's performance is our main concern. The frequency-shifted OFDM signal recirculates back at the input of the I/Q modulator for the second circulation and can be described as

$$E_{in2}(t) = GA^{Opt}E_{in1}(t-\tau)e^{j\cdot\varphi_1(t)}\tilde{V}(t-\tau) + n_1(t) \tag{4.28}$$

where G is the gain of the recirculating loop, τ is the loop delay, $\varphi_1(t)$ is the phase noise for the first circulation due to mechanical disturbance of the fibre and $n_1(t)$ is the ASE noise inside the loop for the first circulation. Following the similar procedure we can get the output of I/Q modulator for the second circulation as

$$E_{out2}(t) = A^{Opt}E_{in2}(t)\tilde{V}(t) \tag{4.29}$$

Therefore the Nth tone can be described as

$$E_{outN}(t) = G^{N-1}(A^{Opt})^N \tilde{V}[t-(N-1)\tau]\tilde{V}[t-(N-2)\tau]\cdot\ldots \\ \cdot\tilde{V}(t)E_{in1}[t-(N-1)\tau]e^{i\sum_{n=1}^{N-1}\varphi_n(t)} + n(t) \quad (4.30)$$

where φ_n is the phase noise for nth circulation and $n(t)$ is the accumulated ASE noise at Nth circulation. It can be seen that the last tone suffers from all the accumulated ASE noise from previous circulations and exhibits the worst Tone-to-Noise Ratio (TNR) which is the bottleneck of the system performance. From Eq. (4.30) we can see there are three factors that will contribute to the TNR of last tone which are accumulated ASE noise, the third order harmonic which is represented by $\tilde{V}(t)$ and the input signal's OSNR which is denoted as $E_{in1}(t)$.

As shown in Figure 4.18(a), the optical I/Q modulator is driven with two equal but 90 ºphase shifted RF tones through I and Q ports to induce a frequency shift to the input optical signal [111]. In the first circulation, the OFDM band at the centre frequency of f_1 (named f_1 band) is generated when the initial OFDM signal at the centre frequency of f_0 is fed into the modulator and incurs a frequency shift equal to the drive frequency f. After amplification by the first EDFA, the f_1 band is split into two branches with one coupled out and the other recirculating back to the input of optical I/Q modulator. In the second circulation, f_2 band is generated by shifting f_1 band along with a new f_1 band which is generated from initial f_0 band, as shown in Figure 4.18(b). Similarly, in the Nth circulation, f_N band is shifted from the previous f_{N-1} band and f_{N-1} is shifted from previous f_{N-2}, etc. The f_{N+1} band and beyond are filtered out by the band-pass filter in the loop. With this scheme, the OFDM bands from f_1 to f_N derive from different circulations and therefore each band contains uncorrelated data pattern. Advantages of such bandwidth expansion scheme are: (i) excessive drive voltage for optical modulator is not required; (ii) the delay of recirculating loop can be adjusted to an integer multiple (30 in this experiment) of the OFDM frame periods, therefore neighbouring bands not only reside at the correct frequency grids, but are also synchronized in OFDM frame which is a necessary condition for OBM [24]; (iii) the signal bandwidth (OFDM bands number) can be adjusted by requirement. The same configuration is proposed in [111] but the quality

of tones including the spectral flatness and TNR was not discussed and the BER performance of the multi-tone signal was not investigated. We extend the application of RFS for bandwidth expansion of uncorrelated multi-band OFDM signal.

4.5.2 Experimental Setup

Figure 4.19(a) shows the experimental configuration of multi-tone generation and real-time CO-OFDM reception. The transmitted data stream consisting of PRBS of length 2^{15}-1 is first mapped onto three OFDM sub-bands with 4-QAM modulation. The 3 OFDM sub-bands were generated by an AWG at 6 GSa/s. Each sub-band contains 46 subcarriers modulated with 4-QAM symbols and 18 unused subcarriers. The 3 sub-bands together with 64 unused subcarriers are converted to the time domain via IFFT with size of 256. The two sub-bands at each side are pre-equalized to compensate the frequency roll-off of AWG. The base-band RF signal is then directly up converted to optical domain through an optical I/Q modulator. At the output of modulator the optical signal is fed into a RFS to generate 22 uncorrelated sub-bands OFDM signal as shown in Figure 4.19(b). The I/Q modulator is driven with two equal but 90 ° phase shifted 4.5-GHz RF tones through I and Q ports, to induce a frequency shifting to the input optical signal [111]. The recirculating loop enables replicating multiple copies by one step per circulation if the initial optical OFDM signal is supplied. The optical spectrum of OFDM signal after RFS is depicted in Figure 4.19(c).

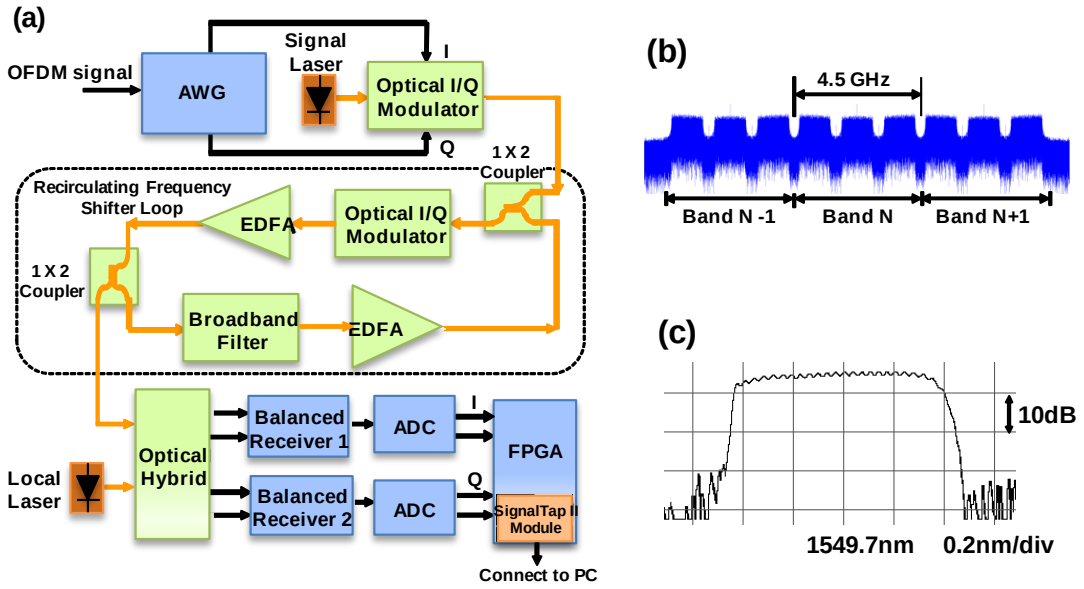

Figure 4.19: (a) Experimental setup for 110 Gb/s real-time CO-SISO-OFDM reception. (b) Electrical spectrum of 3 sub-bands OFDM signal. (c) 110-Gb/s CO-OFDM optical spectrum.

At the receiver side, direct optical-to-RF down-conversion is employed. The principle of signal processing procedures is the same as 3.1-Gb/s real-time reception. Only one sub-band is detected at a time and others are filtered out by two 575-MHz anti-alias LPFs before ADCs. The detected RF signals are then sampled with two high-speed ADCs at 1.5 GSa/s with 7-bit resolution. The signal is transmitted via LVDS interface onto FPGA through 1:2 multiplexed outputs, which lowers the rate down to 750 MSa/s. The multiple inputs are received and de-multiplexed into 4 channels at 375 MSa/s in the FPGA for further processing. After all the OFDM signal processing, the recovered data are compared with transmitted ones in FPGA and the errors are counted. This error count, together with transmitted OFDM frame numbers, is sampled by SignalTap II debugging module and transported via JTAG cable to PC for BER collection.

4.5.3 Measurement Results and Discussion

In this experiment an Altera EP3SL340H1152 FPGA is applied to achieve real-time signal processing. The receiver takes up 9% of Look-Up Tables (LUTs), 11% of

registers, 8% of memory blocks and 8% of DSP blocks. The resource utilization by module is listed out in Table 4.4.

Table 4.4: FPGA chip resource utilization by module

	LUT	Register	Memory	DSP
Timing Sync.	1561	1778	3832	12
Freq. Sync.	5481	4364	1176	0
CP Removal	691	688	244	0
FFT	4082	8913	61824	32
Phase Est.	7916	10580	7496	0
Channel Est.	4000	4308	8688	0
BER Collection	436	462	0	0

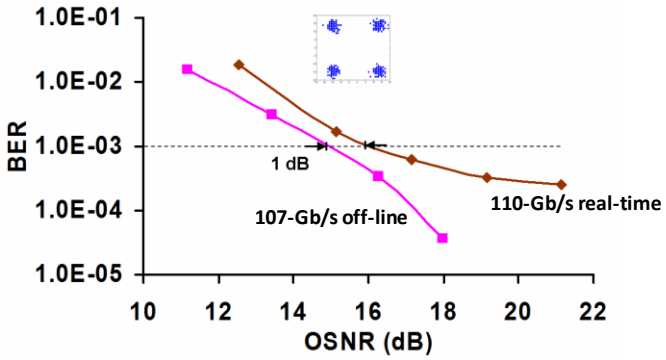

Figure 4.20: Real-time BER performance for the 110-Gb/s CO-OFDM signal at back-to-back transmission.

Figure 4.20 shows the BER performance of 110-Gb/s 4-QAM CO-OFDM signal at back-to-back transmission comparing with that of off-line 107 Gb/s in previous work. The inset shows a typical constellation diagram for the detected CO-OFDM signal. Each point in this figure is obtained by averaging over 30 OFDM transmission blocks each containing 368 OFDM data frames. The combined laser linewidth is about 100 kHz. A BER of 10^{-3} can be observed at an OSNR of 16 dB (ASE noise bandwidth of 0.1 nm) for 4-QAM. The choice of only filling 46 subcarriers out of 64 is due to 575 MHz anti-alias filter used. It is noted that the OSNR penalty of real-time

reception is 1 dB. The BER performance for this real-time 110-Gb/s CO-OFDM transmission is limited by three factors: (i) the noise accumulation for the edge bands that have gone through most of the frequency shifting, and (ii) the large phase drift due to long OFDM frame length by using relatively low sampling rate of 1.5 GSa/s, which can be avoided by using ADCs with higher sampling rate.

4.6 Conclusion

In this chapter, signal processing algorithms for real-time implementation, including OFDM frame synchronization, carrier frequency offset compensation, channel and phase estimation and symbol decision, are elaborated in Section 4.2.

In Section 4.3, the first real-time CO-OFDM reception up to 3.1 Gb/s is demonstrated. By using two high-speed ADCs and a large volume FPGA, optical OFDM signal is sampled and processing within this setup. The real-time transmission experiment confirms the feasibility of CO-OFDM to be used in practical communication networks.

In Section 4.4, two 3.4-GSa/s sample rate ADCs are employed to increase single-band optical OFDM data rate beyond 10 Gb/s. By using 16 parallel signal processing streams inside FPGA the record data rate up to 12.1 Gb/s is achieved. The reason of relatively high BER floor is studied and a solution is provided. ADC performance before and after calibration are compared. The spurious-free dynamic range of ADCs increases by 14 dB after this operation.

In Section 4.5, theoretical analysis of RFS is given and the principle of multi-tone generation is analysed. We demonstrate the experimental setup and performance of 110-Gb/s real-time multi-band CO-OFDM receiver. Three 3.33-Gb/s single polarization CO-OFDM sub-bands are generated simultaneously from AWG. Then they are duplicated 22 times in the RFS loop to expand the total data rate to 110 Gb/s. The BER values of real-time 110-Gb/s reception are compared with the data from off-line 107-Gb/s experiment. The OSNR penalty of real-time reception is around 1 dB.

Chapter 5

Real-time Multiple-Input Multiple-Output CO-OFDM Reception

5.3 Introduction

Since its short conception, CO-OFDM has experienced a rapid progress. It is highlighted by the recent demonstrations of long-haul beyond 1-Tb/s transmissions from various groups [7-8, 48-49]. CO-OFDM has been considered as one of promising alternative pathways toward Tb/s transport. This technology has shown its resilience to chromatic dispersion [24, 47-48], polarization-mode dispersion [105] and achieve high spectral efficiency [112] for optical communication systems. However, most of these results were obtained by off-line processing where only limited length of received signal is sampled and processed. These approaches might be useful to verify signal processing algorithms but do not allow long-term performance verification which is a necessary step for ASIC based product design. To solve this problem, real-time experiments with single-polarization [25**Error! Bookmark not efined.**, 51] have been demonstrated. As shown in [105], SMF link in essence can be represented by a 2×2 MIMO channel, and some sort of polarization diversity, either transmit or receive diversity can be employed for practical implementation. On the other hand, with the rapid advance in silicon digital signal processing, the high-speed ADCs at multi-gigahertz sampling rate and high-speed large-volume 28-nm FPGAs are now commercially available. One benefit of the state-of-the-art FPGA is that it has sufficient gate resource, embedded memory and DSP blocks to process digital signal in multiple parallel channels at a relatively lower clock rate.

In this chapter, the MIMO-OFDM signal processing stage is elaborated in Section 5.2. The first multi-gigabit real-time CO-OFDM receiver for dual polarizations with a 2×2 MIMO-OFDM configuration is shown in Section 5.3. The

experimental setup consists of four 1.5-GSa/s high-speed ADCs and one Stratix III FPGA. The signal streams are processed in real-time mode. 3.33-Gb/s and 6.67-Gb/s net data rates are realized for 4-QAM and 16-QAM modulations, respectively. In Section 5.4, the principle of recirculation loop is introduced to emulate long-haul fibre transmission. The 110-Gb/s multi-band CO-MIMO-OFDM reception with 600-km transmission in recirculation loop is then demonstrated. To achieve this high data rate the wideband optical OFDM signal is generated by a RFS loop where the initial OFDM band is duplicated several times.

5.2 Real-time MIMO-OFDM Signal Processing Algorithms

One of major differences between SISO and MIMO in optical OFDM signal processing is that MIMO system requires recovering two polarization signals with the help of training sequences. Mathematically, the transmitted data frames of two polarization signals in the forms of Jones vector are given by

$$\boldsymbol{c} = \begin{bmatrix} c_x \\ c_y \end{bmatrix} \tag{5.1}$$

Assume the fibre link Jones matrix $\boldsymbol{H}$ is

$$\boldsymbol{H} = e^{j\Phi_D(f_k)} \cdot \boldsymbol{T}_k = \begin{bmatrix} h_{xx} & h_{xy} \\ h_{yx} & h_{yy} \end{bmatrix} \tag{5.2}$$

Expand the received frames $\boldsymbol{c}' = [c'_x \quad x'_y]^T$ after phase noise estimation and compensation. We get

$$\begin{cases} c'_x = h_{xx}c_x + h_{xy}c_y + n_x \\ c'_y = h_{yx}c_x + h_{yy}c_y + n_y \end{cases} \tag{5.3}$$

where n_x and n_y are the random noises for two polarizations. The subcarrier index k and OFDM frame index i are dropped for the sake of simplicity in Eq. (5.3). From the expression Eq. (5.3), the transmitted data frames can be recovered from the received signals by inverting $\boldsymbol{H}$:

$$\boldsymbol{c} = \boldsymbol{H}' \begin{bmatrix} c'_x \\ c'_y \end{bmatrix} + \boldsymbol{H}' \begin{bmatrix} n_x \\ n_y \end{bmatrix}, \qquad \boldsymbol{H}' = \boldsymbol{H}^{-1} \tag{5.4}$$

Subsequently the estimated transmitted frame, $\hat{\boldsymbol{c}}$ is given by

$$\hat{\boldsymbol{c}} = \begin{bmatrix} \hat{c}_x \\ \hat{c}_y \end{bmatrix} = \boldsymbol{H}'\boldsymbol{c}' \tag{5.5}$$

Eq. (5.5) indicates that once the channel transfer function $\boldsymbol{H}$ and the received frame $\boldsymbol{c}'$ are obtained, the estimated transmitted frame $\hat{\boldsymbol{c}}$ can be computed. The two elements of $\hat{\boldsymbol{c}}$, $\hat{c}_x$ and $\hat{c}_y$, are the estimated transmitted frames encoded onto the two polarizations and will be subsequently de-mapped to the nearest constellation points to recover the transmitted frames.

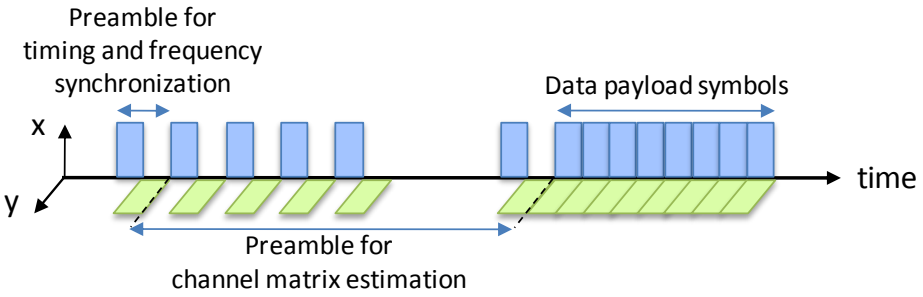

Figure 5.1: Time-domain representation of the dual-polarization OFDM block including training sequences for timing and frequency synchronization, channel matrix estimation and payload. "x" and "y" represent two polarization components.

The training sequences for MIMO-OFDM signal recovery are generated by filling the odd sequences with normal transmitted data, while leaving the even sequences blank. After the polarization multiplexing emulator, the training sequences form a pattern of alternative polarization launch for two consecutive OFDM frames as depicted in Figure 5.1. Using odd training sequences, channel estimation can be expressed as

$$\begin{bmatrix} c'_x \\ c'_y \end{bmatrix} = \begin{bmatrix} h_{xx} & h_{xy} \\ h_{yx} & h_{yy} \end{bmatrix} \begin{bmatrix} c_x \\ 0 \end{bmatrix} \Rightarrow \begin{cases} h_{xx} = c'_x / c_x \\ h_{yx} = c'_y / c_x \end{cases} \tag{5.6}$$

and using even training sequences as

$$\begin{cases} h_{xy} = c'_x / c_y \\ h_{yy} = c'_y / c_y \end{cases} \tag{5.7}$$

It can be seen from Eq. (5.6) and Eq. (5.7), by using alternative polarization training sequence, the full channel estimation of $\boldsymbol{H}$ can be obtained.

5.3 6.67-Gb/s Single-band Real-time CO-MIMO-OFDM Reception

The first multi-gigabit real-time dual-polarization CO-OFDM receiver with 2×2 MIMO configuration is demonstrated in this section. Four balanced photodiodes, four 1.5-GSa/s high-speed ADCs and one FPGA is employed to achieve real-time signal processing. The 3.33 Gb/s and 6.67 Gb/s net data rates are achieved for 4-QAM and 16-QAM signal, respectively.

5.3.1 Experimental Setup

Figure 5.2 shows the experimental setup incorporating the real-time CO-OFDM receiver for dual polarizations in a 2×2 MIMO-OFDM configuration. The transmitted signal is generated by a MATLAB program originated from 2^{15}-1 PRBS, and then mapped to 4-QAM or 16-QAM data frames. The time domain signal is formed after IFFT operation, and then inserted with CP. The I and Q components of the time-domain OFDM signal is uploaded onto a Tektronix AWG which produces the analog signals at 1.5 GSa/s. Total number of OFDM subcarriers is 64; CP length is 1/8 of observation window; 48 subcarriers out of 64 are filled with data, others are left blank as a LPF transit bank; 4 of filled subcarriers are used as pilot tones for phase estimation; 32 out of 500 OFDM frames are used as training sequences for channel estimation. An optical I/Q modulator comprised of two MZMs with 90 °phase shift. It directly up-converts OFDM baseband signals from the RF domain to the optical domain. The single-polarization optical OFDM signal at the output of the I/Q modulator is then evenly split into two polarization branches via a PBS, with one branch delayed by one OFDM frame period, i.e., 48 ns in this experiment. The two polarization branches are subsequently combined via a PBC, emulating two independent transmitters for each polarization, resulting in a composite raw data rate of 1.92 Gb/s for 4-QAM and 3.83 Gb/s for 16-QAM. The net data rate is 1.67 Gb/s for

4-QAM and 3.33 Gb/s for 16-QAM after excluding the overhead from CP and pilot tones.

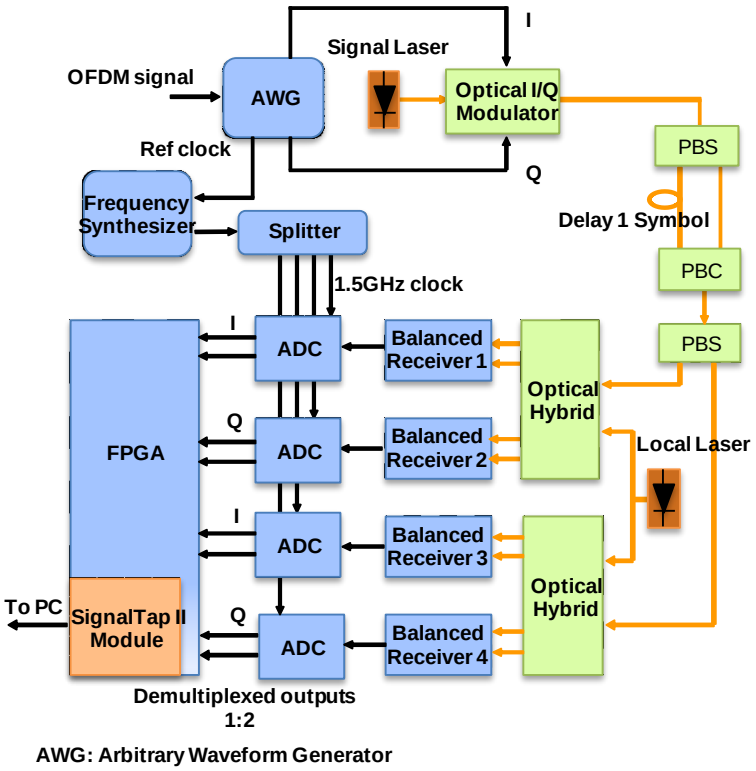

Figure 5.2: Experimental setup for real-time reception of 6.67-Gb/s CO-MIMO-OFDM signals.

At the receiver side, direct optical-to-RF down-conversion is employed. We tune the local laser frequency close to that of the incoming signal. The tolerance of frequency difference between signal laser and local laser is ±2 subcarrier spacings, which is determined by the structure of timing and frequency synchronization training sequence [104]. The optical signal is fed into a PBS for a polarization diversity coherent receiver. Each branch of the splitter is mixed with CW from local laser inside an optical 90 °hybrid, and I and Q ports from the optical 90 °hybrid are used for direct down-conversion. Two balanced receivers at each branch are used to detect I and Q components. The RF signals from the four balanced photo detectors are firstly passed through anti-aliasing LPFs with a bandwidth of 575 MHz, such that only the OFDM signal can be passed through. The detected RF signals are then sampled with four high-speed E2V ADCs at 1.5 GSa/s. Then they are transmitted via LVDS interface

into Altera Stratix III FPGA through 1:2 demultiplexed outputs, where the parallel processing channel is increased to 4 and data rate of each channel is reduced down to 750 MSa/s. Multiple inputs are received and demultiplexed into 8 channels at 187.5 MSa/s in the FPGA for further signal processing. After all the OFDM signal processing, the recovered data are compared with the transmitted ones in FPGA and errors are counted. This error count, together with transmitted OFDM frame numbers, is then sampled by a SignalTap II debugging module and transported via a JTAG cable to PC for BER collection.

5.3.2 Measurement Results and Discussion

The estimated results of matrix *H* are plotted in Figure 5.3(a) and (b). The sinusoidal dependence of the amplitude in Figure 5.3(a) and linear dependence of the phase in Figure 5.3(b) are the result of the slightly timing offset in OFDM frame synchronization. This is also evidenced by the fact the real and imaginary part of the amplitude in Figure 5.3(a) has 90 degree phase shift between each other. The abrupt phase jump in Figure 5.3(b) is due to the 2π phase wrap. The subcarrier index range is 1 to 48 because 48 out of 64 subcarriers are used. By using the inverse of this matrix in Eq. (5.5) and the received data payload frames, the transmitted frames in the two polarizations can be recovered.

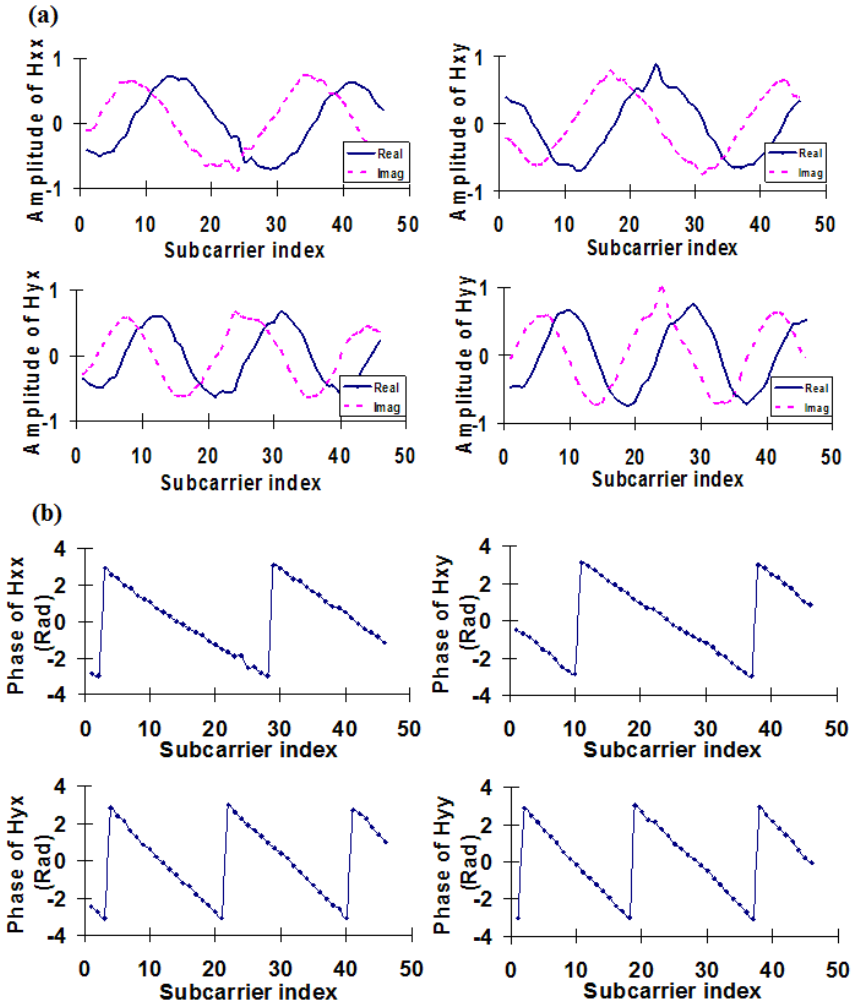

Figure 5.3: (a) Amplitude and (b) phase of estimated channel transfer function matrix elements H_{xx}, H_{xy}, H_{yx} and H_{yy} as a function of subcarrier index.

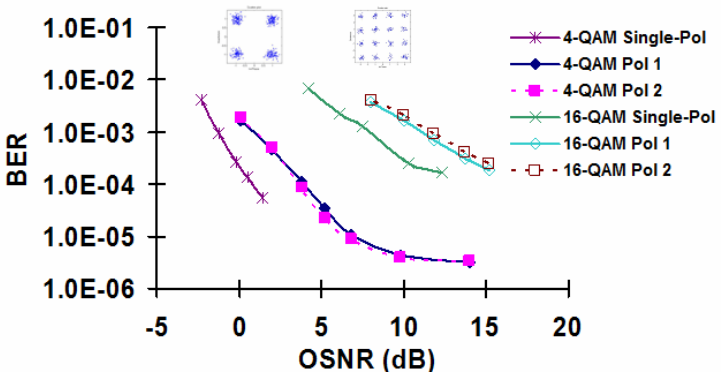

Figure 5.4: Real-time BER performance for CO-MIMO-OFDM signal at back-to-back transmission. Constellations for 4-QAM and 16-QAM are measured at 5-dB and 14.8-dB OSNR, respectively.

This real-time CO-MIMO-OFDM receiver uses a resource of 28 % of LUT, 35% of dedicated registers, 26% of memory and 48% of DSP blocks of the FPGA chip (Altera Stratix III EP3SL340H1152). Figure 5.4 shows the BER performance of 3.33-Gb/s 4-QAM and 6.67-Gb/s 16-QAM coherent optical MIMO-OFDM signals at back-to-back transmission comparing with those of 1.55-Gb/s and 3.1-Gb/s CO-SISO-OFDM reception. Each data point in this figure is an average of 50 OFDM transmission blocks with each containing 288 OFDM data frames. The combined laser linewidth is about 100 kHz. A BER of 10^{-3} can be observed at an OSNR of 0.6 dB (ASE noise bandwidth of 0.1 nm) for 4-QAM signal with the polarization dependence less than 0.3 dB. The OSNR requirement for 4-QAM MIMO transmission increases by 2.7 dB at 10^{-3} BER compared with single polarization, which is close to the theoretical penalty of 3 dB. A BER floor emerges at around $3x10^{-6}$ because the training sequence length is only 64 points, which limits the accuracy of frequency offset estimation. The obtained data rate is limited to 3.33 Gb/s due to the maximum sampling rate of 1.5 GSa/s offered by the ADCs. The choice of only filling 46 subcarriers out of 64 is due to 575-MHz anti-alias LPFs. Accessing a higher sampling rate ADCs can further improve the data rate. We also show the performance of 6.67-Gb/s 16-QAM in Figure 5.4. The OSNR sensitivity for a BER of 10^{-3} is about 11 dB. The relative large penalty compared to the 4-QAM is due to the BER floor at 10^{-4}. This BER floor for 16-QAM is attributed to the limited 7-bit resolution of ADCs, and large phase noise impairment due to long OFDM frame length by using relatively low sampling rate of 1.5 GSa/s. This can be avoided by using ADCs with higher sampling rate.

5.4 110-Gb/s Multi-band Real-time CO-MIMO-OFDM Reception

Multi-band OFDM is proposed to alleviate bandwidth constraint of ADCs. It has been shown that a part of OFDM spectrum can be carved out and detected as a fraction of the overall data rate [46-47]. A multi-band 54-Gb/s real-time CO-OFDM reception has been demonstrated [25]. However it skips carrier frequency compensation which

is indispensable for practical application. In this experiment, a demonstration of FPGA based multi-band real-time CO-MIMO-OFDM receiver at a data rate of 110-Gb/s is provided. The multi-band CO-OFDM signal is successfully received and recovered after 600-km recirculation loop transmission and 400-ps DGD.

5.4.1 Principle of Recirculation Loop

Recirculation loops have been widely used in optical transmission experiments. It can emulate optical signal transmission over thousands of kilometres by recirculating the signal in an optical fibre loop many times. Therefore it provides a highly economic method to investigate various fibre transmission issues [113].

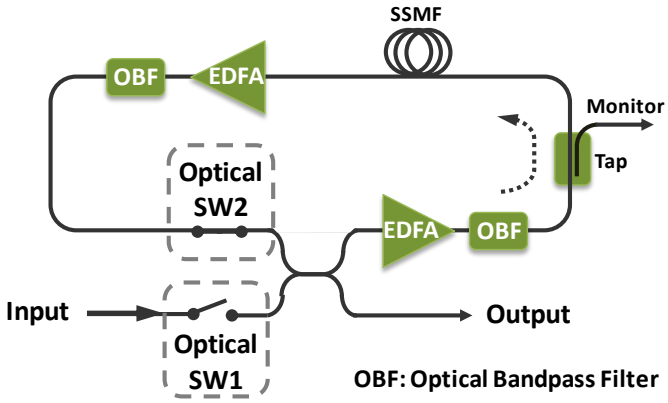

Figure 5.5: Recirculation loop architecture.

Figure 5.5 shows the recirculation loop architecture. SW1 is used to connect signal path in the assigned pulse period while cut off all signal at other time. In the assigned pulse period, the signal is fed into the loop through the 2:2 3-dB coupler. The optical OFDM signal is first amplified by an EDFA and then filtered by an optical band-pass filter to eliminate ASE noise. After the monitor tap, the signal goes into the SSMF then amplified again by the second EDFA with constant output to compensate transmission loss. Then there is a SW2 switch. At the exact same time when SW1 is connected to let signal pass, SW2 will be disconnected. In this way, if the pulse width for SW1 and SW2 is much more than the period in which the optical signal goes through the loop, the signal will first fill all the loop. Once SW1 is disconnected and SW2 is connected, the signal will go through the loop round by round. The signal will be continuous without gap and signal from each round will be coupled out from loop

through the 3 dB coupler. As long as the signal power after both switches is the same, the power level for each round does not change.

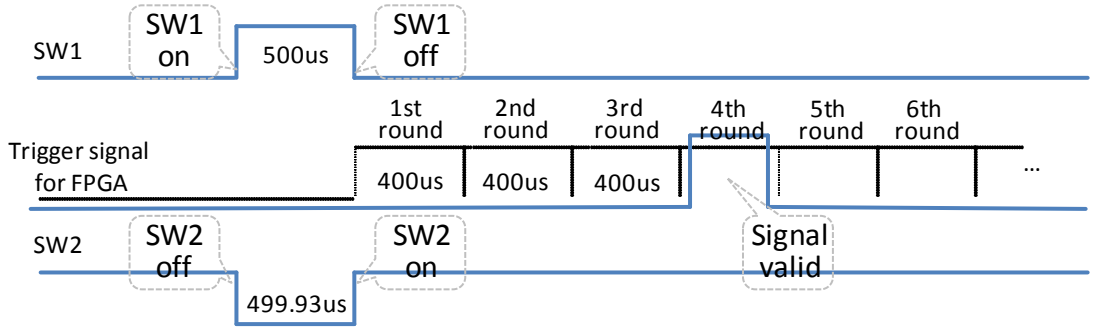

Figure 5.6: Timing for SW1 and SW2 of the recirculation loop.

Figure 5.6 shows the timing relation of three signals which are used to control the two switches and FPGA. In this example 80-km fibre span is used inside the loop. Since the duration for optical signal to traverse 80 km optical fibre is approximately 400 us, the pulse width for both switches is set to around 500 us. The control signals come from the same pulse generator. The trigger signal delay is precisely tuned to trigger the receiver (FPGA) at the correct timing which corresponds to wanted signal. The tiny difference between the pulse widths of two switches is due to the imperfection of the devices. The two pulses have to be perfectly aligned to each other in order to avoid EDFA unwanted overshoots and undershoots.

If the timing characteristics of SW1 and SW2 are well matched, the signal inside the loop will be continuous. Then after amplification by EDFAs as shown in Figure 5.5, the amplified signal will also be continuous. However, if switches have minor timing difference, there will be small gaps between each round. Then EDFA will generate overshoots and undershoots at the gap position which will generate negative impact on the system performance.

5.4.2 Experimental Setup

The experimental setup for multi-tone generation and real-time CO-OFDM reception is shown in Figure 5.7. The transmitted data stream consists of 2^{15}-1 PRBS is first mapped onto three OFDM sub-bands. Each sub-band contains 46 subcarriers with 4-

QAM modulation and 18 unfilled subcarriers. 21 unfilled subcarriers are placed at each side of the central sub-band and 11 unfilled subcarriers are placed at left end of the left sub-band and right end of right sub-band, which allows them to be eventually distributed when patched with other tones. The two side sub-bands are pre-equalized to compensate the frequency roll-off of AWG as shown in Figure 5.7 (see the inset next to AWG). The 3 sub-bands together with 64 unfilled subcarriers are converted to the time domain via IFFT with size of 256. 1/8 of CP ratio is used, resulting in an OFDM frame size of 288. The time domain OFDM signal were converted to analog form by an AWG at 6 GSa/s. Each OFDM block contains 504 OFDM frames. Within each block, the first and third OFDM frame serves as timing and frequency offset estimation sequence and the second and fourth one are left blank. In the next 32 training sequences odd ones are normally modulated with transmitted data while even ones are unfilled to form a pattern of alternative polarization launch after polarization multiplexing emulator. The base-band OFDM signal is then directly up-converted into optical domain through an optical I/Q modulator. At the output of modulator the optical signal is fed into a RFS to generate 11 uncorrelated OFDM bands (see the inset at the output of RFS). The RFS is consisted of a closed fibre loop, an I/Q modulator and EDFAs to compensate the frequency conversion loss. The I/Q modulator is driven with two equal but 90° phase shifted 6-GHz RF tones through I and Q ports to induce a frequency shifting to the input optical signal [111]. The recirculating loop enables replicating multiple copies by one step per circulation if the initial optical OFDM signal is supplied. Because of the extreme large loop delay introduced between the neighbouring bands, each individual band is completely uncorrelated. The net data rate for each sub-band is 3.33 Gb/s, which contributes 10 Gb/s for each band. The total net data rate achieves up to 110-Gb/s after bandwidth expansion. The signal is then coupled into a recirculation loop comprising 100-km standard SSMF and a two-stage EDFA to compensate the loss. It is coupled out from the loop after 6 circles to emulate 600 km optical fibre transmission and fed into a polarization multiplexing emulator to simulate two independent transmitters and a PMD generator to add 400-ps PMD into the signal. The optical spectrum of CO-

OFDM signal after RFS and polarization multiplexing emulator is shown in Figure 5.8.

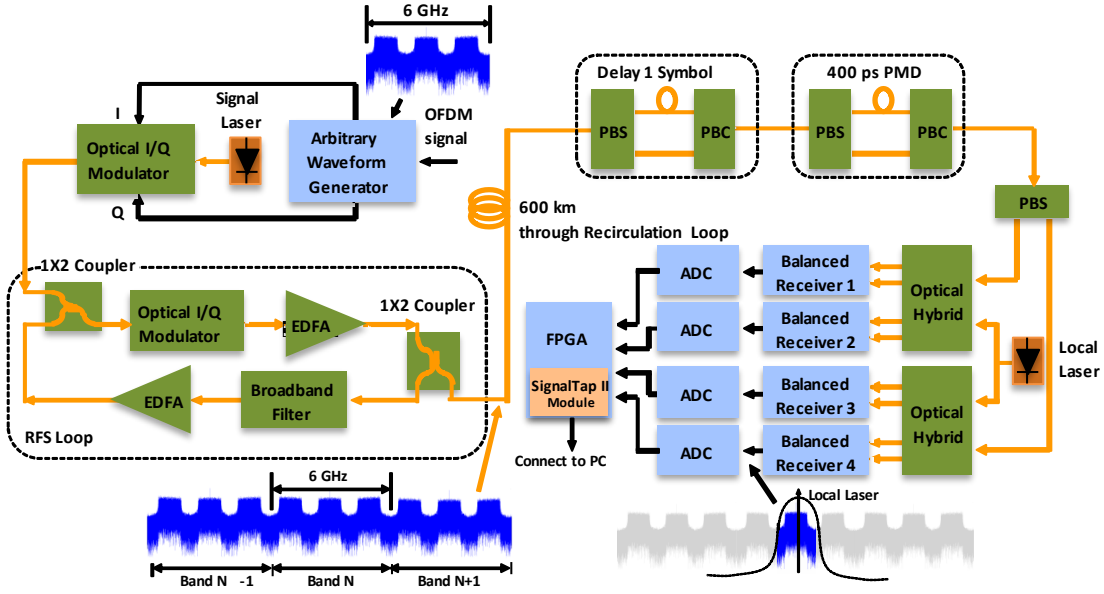

Figure 5.7: Experiment setup for real-time 110-Gb/s CO-MIMO-OFDM reception with 600-km transmission and 400-ps DGD.

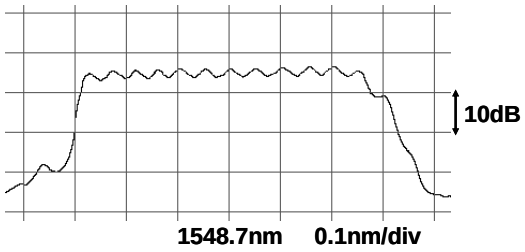

Figure 5.8: Optical spectrum of 110-Gb/s CO-OFDM signal at back-to-back transmission.

At the receiver side, direct optical-to-RF down-conversion is used to detect optical OFDM signal. The principle of signal processing procedures is the same as [114]. At each time only one sub-band is detected and others are filtered out by two 575-MHz anti-alias LPFs before ADCs. The detected RF signals are then sampled with four high-speed ADCs at 1.5 GSa/s with 7-bit resolution. The signal is transmitted via LVDS data cables into FPGA through 1:2 multiplexed outputs, which lowers the rate down to 750 MSa/s. The multiple inputs are received and de-multiplexed into 4 channels at 375 MSa/s in the FPGA for further processing. After all of the OFDM signal processing, the recovered data are compared with transmitted in

FPGA and the errors are counted. This error count, together with transmitted OFDM frame numbers, is sampled by SignalTap II (an embedded logic analyzer from FPGA vendor Altera) debugging module and transported via Joint Test Action Group (JTAG) interface, a common standard for testing integrated circuits and printed circuit boards using boundary scan, to PC for BER collection.

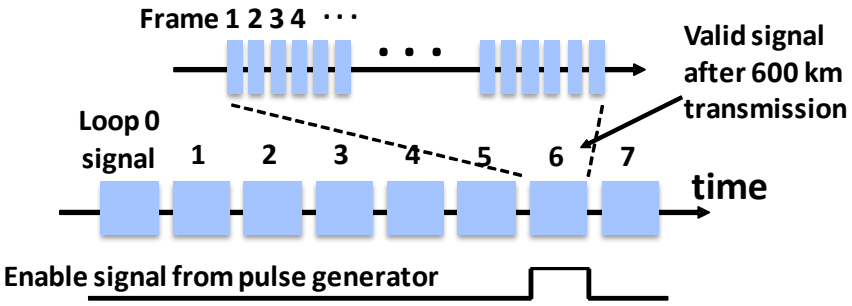

Figure 5.9: Enable signal indicating valid data for 600-km optical fibre transmission in recirculation loop.

In 600-km transmission experiment, an trigger signal from pulse generator is required to indicate valid signal for BER counting due to use of recirculation loop for long-haul transmission emulation, as shown in Figure 5.9. This signal is imported into FPGA chip to enable or disable the timing synchronization module to generate timing signal, which is indispensable for the rest of signal processing modules. When the timing signal is disabled, the BER is not being calculated, namely, only the BER for the OFDM signal after 600-km transmission is collected.

The CO-MIMO-OFDM receiver architecture can be divided into nine stages: (1) OFDM frame synchronization, (2) carrier frequency offset compensation, (3) CP removal, (4) FFT, (5) phase estimation for training sequences, (6) channel estimation, (7) Jones Matrix inversion to recover two polarization signals, (8) phase estimation for payload frames, and (9) symbol decision, error accumulation and BER computation. A time-domain preamble for OFDM frame synchronization that is partitioned into four segments is used [104]. To improve the accuracy of frequency offset estimation two training sequences are used for timing and frequency estimation. The timing metric of real-time data is shown in Figure 5.9(a).

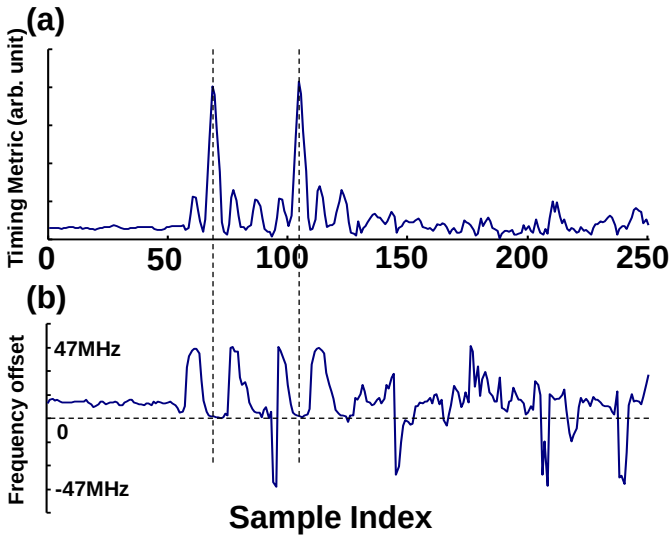

Figure 5.10: (a) Timing metric for one polarization CO-MIMO-OFDM signal; (b) Frequency offset estimate for the CO-MIMO-OFDM signal.

Figure 5.10(b) demonstrates the estimated frequency offset from two training sequences. According to the scheme proposed in [104], at timing estimate points the calculated values are estimated frequency offsets. The data used for frequency offset compensation is an average of these two values to improve accuracy.

5.4.3 Measurement Results and Discussion

The averaged BER performance of 11 bands 4-QAM modulation CO-MIMO-OFDM signal at back-to-back transmission up to 110-Gb/s with and without 400-ps PMD is demonstrated in Figure 5.11. The state of polarization in the system is free-running and no manual polarization control is used during measurement. Each point in these curves is obtained by averaging over 30 OFDM blocks. The combined laser linewidth is about 100 kHz. A BER of 10^{-3} can be observed at 22 dB OSNR for 4-QAM signal. It is noted that the difference of BER performance for two polarization signals at the same OSNR is less than 0.5 dB and OSNR penalty for 400-ps DGD is smaller than 0.5 dB at 10^{-3} BER.

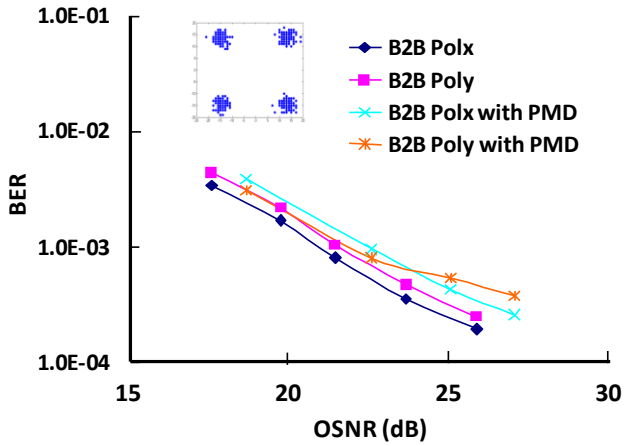

Figure 5.11: Averaged BER performance of 11 bands CO-OFDM signals at back-to-back transmission with and without 400-ps PMD.

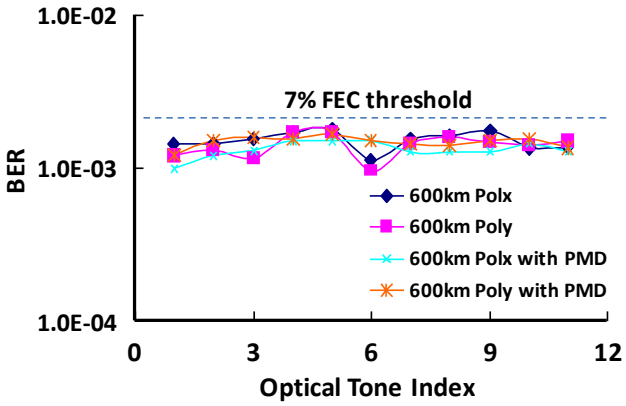

Figure 5.12: BER performance for individual OFDM tones after 600-km transmission.

The receiver performance after 600-km recirculation loop transmission is also measured. The launch power is -10.4 dBm. Figure 5.12 shows the BER performance of the 11 tones each at the reach of 600 km with and without 400-ps DGD. It can be seen that all of the tones can achieve a BER better than the FEC threshold 2×10^{-3}. It is notable that there is no observable BER penalty for 400-ps DGD. The BER performance for this real-time 110-Gb/s CO-MIMO-OFDM transmission is limited by two factors: (1) ASE noise accumulation for the edge bands that have gone through most of the frequency shifting, and (2) the large carrier phase drift due to long OFDM frame length by using relatively low sampling rate of 1.5 GSa/s, which can be avoided by using higher sampling rate ADCs.

5.5 Conclusion

In this chapter, Jones matrix inversion algorithm to recover two polarization signals in MIMO-OFDM transmission is investigated in Section 5.2. This algorithm employs interleaved OFDM training sequences and blank sequences on two polarizations to estimate optical fibre channel matrix.

In Section 5.3, the first 6.67-Gb/s single-band CO-MIMO-OFDM reception is demonstrated. This scheme modulates different data payloads on two polarizations in optical fibre. With this method the throughput of the same fibre is doubled than SISO configuration.

In Section 5.4, 110-Gb/s wideband optical OFDM signal is generated by duplicating a relatively low data rate signal band in a RFS loop 11 times. This expanded signal is then transmitted 600 km in a recirculation loop. At the receiver each band is carved out for real-time reception and BER measurement. After long-haul transmission and DGD interference, the BER values of all 11 bands are still below 7% FEC threshold.

Chapter 6

I/Q Imbalance Compensation for CO-OFDM Systems

6.1 Introduction

OFDM technique has been extensively used in wireless communication systems such as Wireless Local Area Networks (WLAN) and digital broadcasting systems. The Digital Audio Broadcasting (DAB) system and the digital terrestrial TV broadcasting system have also employed this technique. Recently, this technology has been introduced into optical communication by Shieh et al. [13]. It combines the benefits of OFDM and optical transmission to achieve high spectral efficiency, robustness to CD and PMD, and ease for reach long-haul communication. The surging interest in optical OFDM has resulted in research activities that make the transceiver more reliable and less costly in practice. There are majorly two types of OFDM architecture: homodyne and heterodyne [115]. Homodyne is also referred as direct-conversion or zero-IF conversion. Compared to the heterodyne transceivers, the direct-conversion ones have the advantages of low cost, low power consumption and less electrical bandwidth requirement for electrical components, but they suffer more severely from analog domain impairments. Such impairments are caused by the imperfectness of optical I/Q modulator, balanced photo detectors and optical hybrids. These effects are generally modelled as I/Q imbalance. I/Q imbalance is the mismatch in amplitude and phase between the I- and Q-branch. The effects of it in wireless OFDM transmission have been investigated in previous works. Some algorithms have also been proposed for the compensation of wireless I/Q imbalance [26-29], while only a few applications of I/Q imbalance compensation in optical OFDM have been reported [30-32] and real-time I/Q imbalance estimation and calibration has not been studied to the best of our knowledge. In this chapter, a low over-head and training sequence based hybrid (time and frequency)-domain Tx and Rx I/Q imbalance calibration scheme for CO-OFDM

transmission is proposed for both off-line processing and real-time processing. Four training sequences are employed for time domain Rx I/Q imbalance calibration and the following four sequences are used for both frequency domain Tx I/Q compensation and channel estimation. This scheme is effective even in presence of carrier frequency offset.

6.2 10.8-Gb/s Hybrid Domain Tx and Rx I/Q Imbalance Compensation

The 10.8-Gb/s off-line I/Q imbalance compensation experiment is conducted to evaluation the performance of compensation algorithms for real-time implementation. The only difference between off-line and real-time experimental setup is that the high-speed DSO and signal processing software are replaced by high-speed ADCs and a FPGA board.

6.2.1 Experimental Setup

Figure 6.1 shows the experimental setup for 10.8-Gb/s off-line Tx and Rx I/Q imbalance compensation. The transmitted 2^{18}-1 PRBS stream is first mapped onto 16-QAM modulation and then generated by AWG at 5 GSa/s. The OFDM spectrum consists of 256 subcarriers with the central 154 are filled with data. 1/16 of cyclic-prefix ratio is used, resulting in an OFDM frame size of 272. The total number of OFDM frames in each block is 225. The first one is designed for OFDM frame synchronization. The following four training sequences are used for Rx I/Q compensation and the fifth to eighth frames are for channel estimation and Tx I/Q calibration. The base-band RF signal is directly up converted from RF domain to optical domain through an optical I/Q modulator which is comprised of two MZMs with 90^{o} phase shift, that is, each MZM is respectively driven by the real or the imaginary part of transmitted signal from two output ports of AWG.

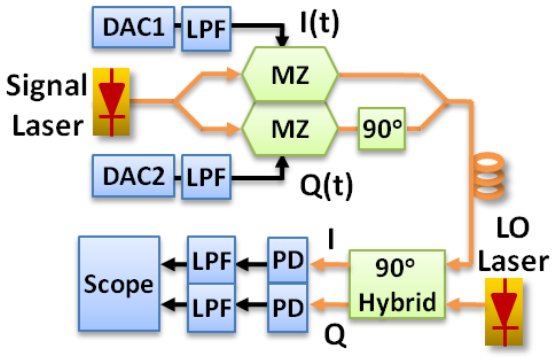

Figure 6.1: Experiment setup for off-line Tx and Rx I/Q imbalance compensation.

At the receiver side, direct optical-to-RF down-conversion is employed. The local laser frequency is tuned to close to the centre of the incoming signal spectrum. Both the signal and local laser are fed into an optical 90 º hybrid. Two balanced photodiodes are used to detect the in-phase and quadrature components. The down-converted I and Q signals go through two 3.8-GHz anti-alias LPFs to reconstruct signal spectrum before sampled by an oscilloscope running at 5 GSa/s. The sampled data from the scope are then transported to a computer where digital signal processing is performed and BER and Q values at different OSNRs are calculated.

Because the I/Q mismatch of experimental setup is relatively small, we intentionally add extra Tx and Rx imbalance by setting I-channel output voltage of AWG to be 0.67-dB higher than Q-channel (change the I-channel output to be 0.6 V while keep Q-channel output at 0.7 V) to induce Tx amplitude imbalance. 10-ps delay is added onto Q channel to induce Tx phase imbalance. At Rx side, I- and Q-channel amplitude mismatch is set to 2 dB by attaching a 2-dB RF attenuator before the I-channel LPF.

6.2.2 Measurement Results and Discussion

The performance of I/Q imbalance compensation algorithms are evaluated by comparing the BER and Q improvements at different OSNRs. Figure 6.2 shows the BER performance of 10.8-Gb/s 16-QAM CO-OFDM signal at optical back-to-back transmission with and without Tx and Rx I/Q imbalance calibration. The two insets are typical constellation diagrams of the detected CO-OFDM signal with (lower inset)

and without (upper inset) I/Q calibration. The combined laser linewidth is around 100 kHz. A BER of $1x10^{-3}$ can be observed at an OSNR of 10.5 dB (ASE noise bandwidth of 0.1 nm). It is noted that the OSNR requirement is reduced by nearly 1 dB at the BER of $1x10^{-3}$. The BER improvement keeps almost the same from 15-dB down to 11-dB OSNR and then shrinks to minimal, which indicates that the algorithms performs better at higher signal quality. This phenomenon is reasonable because the estimated imbalance degrades with the increase of induced ASE noise power comes from EDFAs inside the optical link.

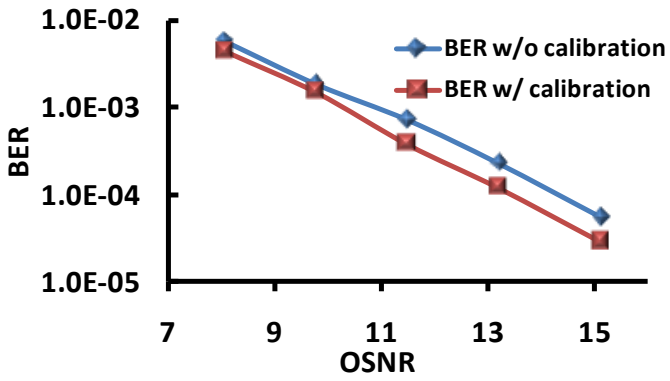

Figure 6.2: BER vs. OSNR for 16-QAM CO-OFDM signal at 10.8 Gb/s data rate with and without Tx and Rx I/Q imbalance.

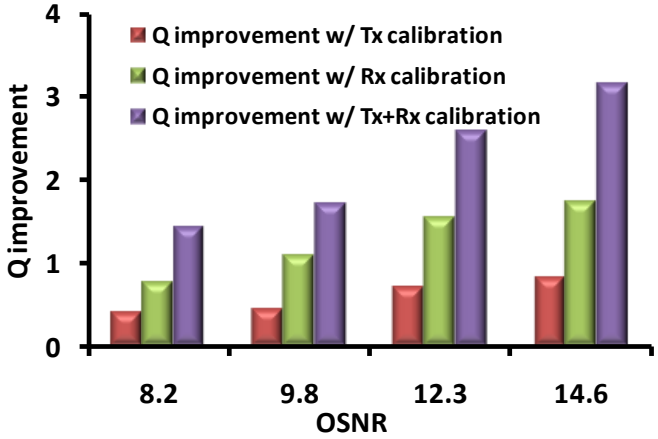

Figure 6.3: Q improvement for various calibration schemes with intentional I/Q mismatch.

The Q improvements of three scenarios are also measured: Tx I/Q imbalance calibration only; Rx I/Q imbalance calibration only and simultaneous Tx+Rx I/Q imbalance calibration. In the three measurements intentional Tx and Rx imbalance are

induced to better evaluate the robustness of compensation algorithms. Testing results are shown in Figure 6.3. When OSNR is as low as 8.2 dB we still get average 0.4-dB Q improvement if the Tx calibration is applied, although in this situation the BER is over $5x10^{-3}$ according to the BER vs. OSNR curve in Figure 6.2. For the Tx+Rx calibration algorithm we attain an better 1.5-dB Q upgrade. The Q improvement rise steadily with the increase of OFDM signal quality for all of the three scenarios. The collected largest upgrade is up to over 3 dB at 14.6-dB OSNR. It is clear that the algorithms can still achieve Q improvement in a poor signal condition, though the improvement is even larger at higher OSNRs.

6.3 10.7-Gb/s Real-time Tx and Rx I/Q Imbalance Compensation

A low over-head and training sequences based real-time hybrid-domain Tx and Rx I/Q imbalance calibration algorithm for CO-OFDM transmission is demonstrated in this experiment. All of signal processing is performed inside one large volume FPGA chip and the experimental results are transported to a computer for data collection.

6.3.1 Experimental Setup

Figure 6.4 shows the experimental setup of real-time I/Q imbalance compensation for CO-OFDM reception. The transmitted data stream is first mapped onto 2 OFDM sub-bands with 16-QAM modulation. The 2 sub-bands were generated by an AWG at the sample rate of 6.8-GSa/s and its spectrum is shown in the inset of Figure 6.4. The central sub-band consists of 112 subcarriers with 16-QAM modulation format and 16 unfilled subcarriers. It is pre-equalized to compensate frequency roll-off of AWG output characteristic as shown in the inset of Figure 6.4. The blank sub-bands with two groups of 64 unfilled subcarriers are placed at two ends of the central sub-band to alleviate roll-off slope requirement of anti-alias LPFs before high-speed ADCs. The 2 sub-bands are converted to the time domain via 256 points IFFT. 1/16 of cyclic-prefix ratio is used, resulting in an OFDM frame size of 272. The total number of OFDM frames in each block is 451. The first one is designed for frame synchronization and

frequency offset compensation. The second to fourth ones are training sequences for Rx I/Q imbalance calibration. The following four sequences are for channel estimation and Tx I/Q imbalance calibration. The base-band RF signal from AWG is then directly up converted to optical domain through the optical I/Q modulator.

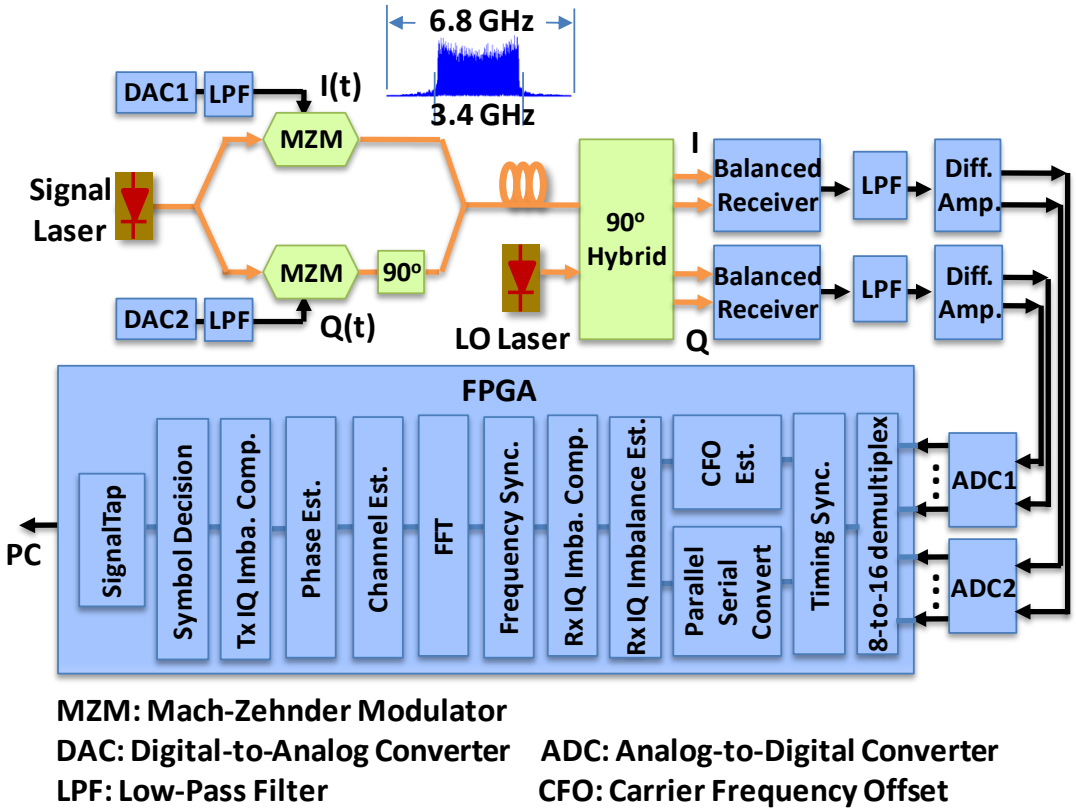

Figure 6.4: Experiment setup for real-time I/Q imbalance compensation.

At the receiver side, direct optical-to-RF down-conversion scheme is employed. The local laser frequency is finely tuned to the centre of the incoming signal spectrum. Both the signal and local laser are fed into an optical 90 °hybrid to linearly convert the I and Q components of the incoming signal to baseband. Two balanced photo detectors are used to detect the down-converted signals. Only the central sub-band is detected and the rest part is filtered by two 3.8-GHz anti-alias LPFs before ADCs. The detected single-end RF signals are then converted to differential to match the input requirement of ADCs by using two high-speed differential amplifiers. The two differential analog signals are sampled by two high-speed ADCs at 3.4-GSa/s with 7-bit resolution. The signal is demultiplexed into 8 channels inside the ADC chips and transmitted through LVDS cables into FPGA evaluation board at the line

rate of 425 MSa/s for each channel. The multiple inputs are received and further de-multiplexed into 16 parallel channels at 212.5 MSa/s inside the FPGA for further processing. The real-time CO-OFDM receiver architecture is divided into eleven stages as shown in Figure 6.4: (i) timing synchronization, (ii) parallel-to-serial conversion and CP removal, (iii) carrier frequency offset estimation, (iv) Rx I/Q imbalance estimation, (v) Rx I/Q imbalance compensation, (vi) frequency synchronization, (vii) FFT, (viii) channel estimation, (ix) phase estimation, (x) Tx I/Q imbalance calibration and (xi) symbol decision and BER calculation. After all of the OFDM signal processing, the recovered data are compared with transmitted data and error bits are counted. This error count is sampled by the SignalTap II debugging module and transported through a JTAG cable to a PC for BER collection.

6.3.2 Measurement Results and Discussion

The Rx I/Q imbalance compensation module only takes up 7.4% of LUTs, 3.6% of registers, 7.8% of memory and 4.8% of DSP blocks and Tx I/Q imbalance compensation module takes up 2.7% of LUTs, 3.1% of registers, 1% of memory and 15% of DSP blocks out of FPGA hardware resource. The hardware cost to implement receiver side I/Q imbalance compensation is relatively low compared with the whole FPGA chip.

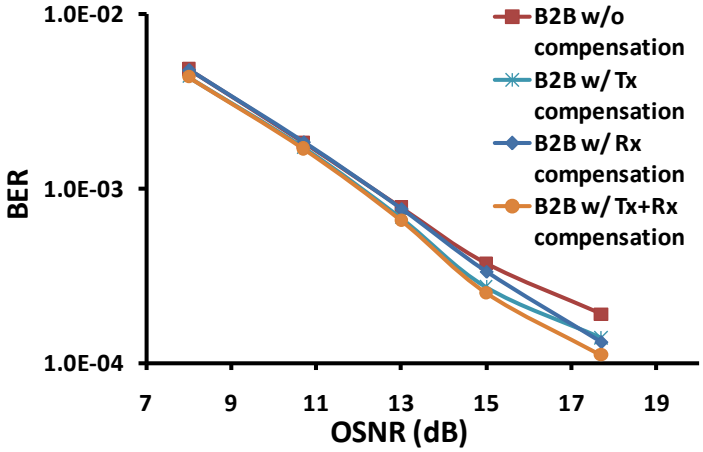

Figure 6.5: BER performance comparison between no compensation, Tx compensation only, Rx compensation only and Tx+Rx compensation.

The BER performance of 10.7-Gb/s 16-QAM CO-OFDM signal at back-to-back transmission with and without I/Q imbalance calibration are shown in Figure 6.5. The combined laser linewidth is around 100 kHz. The light blue, blue and orange curves are the values of optical back-to-back transmission with Tx imbalance calibration, Rx imbalance calibration and Tx+Rx imbalance calibration respectively. The BER decreases obviously at the OSNRs higher than 15 dB and the largest value comes from combined Tx and Rx compensation scheme.

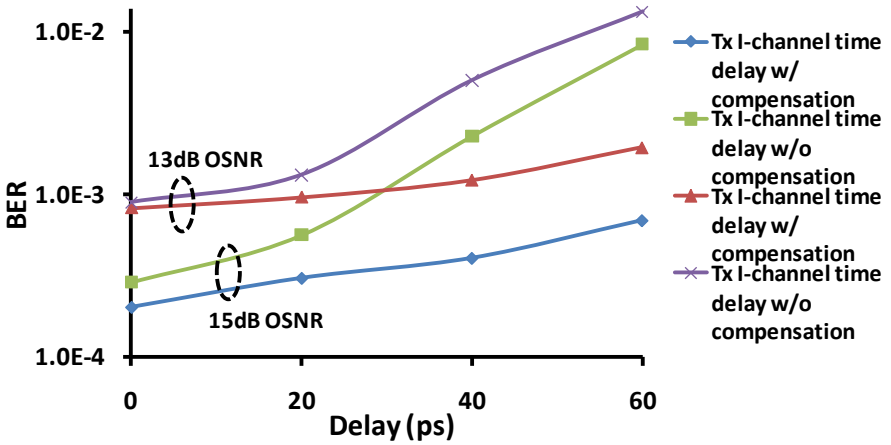

Figure 6.6: BER improvement at 13-dB and 15-dB OSNR with intentional Tx I/Q delay mismatch.

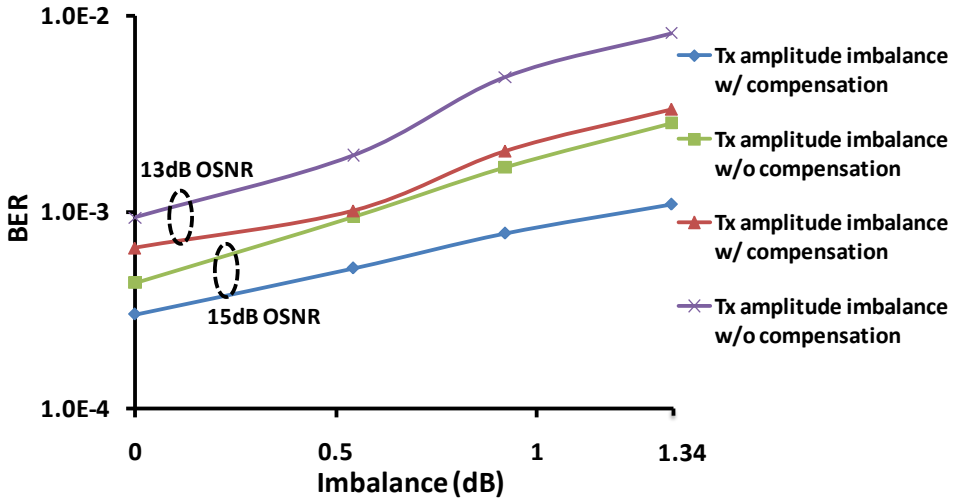

Figure 6.7: BER improvement at 13-dB and 15-dB OSNR with intentional Tx I/Q amplitude mismatch.

To further evaluate the real-time calibration algorithms, intentional I/Q

imbalances at the transmitter and the receiver are added respectively. The transmitter I/Q imbalance is induced by adjusting the I-channel output voltage and delay in AWG. The BER improvements at 13-dB and 15-dB OSNRs are collected in Figure 6.6 (amplitude mismatch) and Figure 6.7 (delay mismatch). The scheme performs best for the delay mismatch calibration. The BER decreases from near $1x10^{-2}$ to around $8x10^{-4}$ at 15-dB OSNR when the timing mismatch is set to 60 ps. A similar case can be found from the 15-dB OSNR curves.

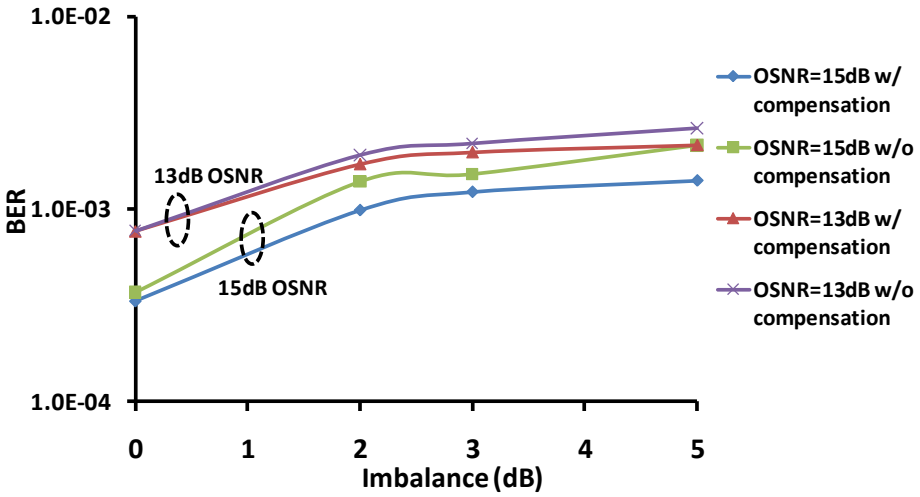

Figure 6.8: BER improvement at 13-dB and 15-dB OSNR with intentional Rx I/Q amplitude mismatch.

Different RF attenuators are attached to the I-branch to induce different Rx I/Q imbalances. The performances are measured at 15-dB and 13-dB OSNR respectively. The BER improvement versus imbalance is shown in Figure 6.8. For 15-dB OSNR signal the BER decrease from around $2x10^{-3}$ to $1x10^{-3}$ after receiver side I/Q calibration when the imbalance is set to 5 dB. The BER improvements decrease if the intentional I/Q imbalance is reduced. Two similar curves can be found for 13-dB OSNR signal but the BER improvement is a bit lower because the accuracy of estimated I/Q imbalance factors decrease with the increase of noise power.

6.4 Conclusion

A hybrid time and frequency domain I/Q imbalance compensation scheme is investigated in this chapter. The Rx I/Q imbalance is estimated and compensated in time domain after OFDM frame synchronization and Tx I/Q imbalance is processed after channel and phase estimation.

An off-line I/Q imbalance calibration experiment for 10.8-Gb/s CO-OFDM transmission is demonstrated in Section 6.2. The OSNR requirement is reduced by 1 dB at the BER of $1x10^{-3}$ for 16-QAM signal with both Tx and Rx calibration.

In Section 6.3, a real-time I/Q imbalance calibration is shown. This compensation scheme takes up 10.1% of FPGA on-chip look-up tables, 6.7% of registers, 8.8% of embedded memories and 19.8% of DSP blocks. BER performances with and without I/Q calibration are compared at 13-dB and 15-dB OSNR, respectively. The transmitter I/Q delay mismatch calibration achieves best improvement.

Chapter 7

Conclusions

7.1 Summary of the Work

In this thesis, real-time CO-OFDM signal processing is investigated in several critical aspects. The real-time single-input single-output CO-OFDM reception is demonstrated with data rates of 3.1 Gb/s and 12.1 Gb/s for single-band OFDM signals and 110 Gb/s for a multi-band signal. The multiple-input multiple-output configuration is also well elaborated. MIMO implementation in real-time reception has reached data rates of 6.67 Gb/s (single-band) and 110 Gb/s (multi-band). In the last part, I/Q imbalance and its compensation techniques with off-line signal processing and real-time processing are investigated.

7.2 Real-time Single-Input Single-Output CO-OFDM Reception

Coherent optical OFDM has become an extensive research subject in fibre communication. However, most of the research works are conducted through off-line processing model. The real-time CO-OFDM reception is imperative for long term evaluation. An analysis on real-time signal processing algorithms is conducted in Section 4.2. The off-line OFDM frame synchronization scheme and carrier frequency offset compensation scheme are replaced to adapt to the hardware architecture. The channel estimation, phase estimation and symbol decision algorithms are simplified for the ease of real-time implementation. In Section 4.3, we demonstrate the first real-time CO-OFDM receiver with data rates of 1.55 Gb/s for 4-QAM and 3.1 Gb/s for 16-QAM modulation formats. In Section 4.4, a 12.1-Gb/s single-band CO-OFDM receiver was shown based on 3.4-GSa/s high speed ADCs. The root causes of a relatively high error floor of the BER curve are thoroughly analysed and solutions are provided. After upgrading the ADC analog input configuration to differential, the

measured SFDR of ADCs has increased from 16 dB to over 30 dB. In Section 4.5, the RFS is introduced to generate multiple orthogonal OFDM signal bands to alleviate bandwidth bottleneck of ADCs. By dividing the whole spectrum into many relatively narrower bands, each one of them can be carved out and detected at a time. Thus, the requirement of sampling rate for ADCs is reduced and start-of-the-art silicon devices are possible to process the OFDM signal beyond 100 Gb/s. By using the RFS, we demonstrate the 110-Gb/s multi-band CO-OFDM reception. The OSNR penalty of real-time reception is 1 dB compared with the 107-Gb/s off-line transmission.

7.3 Real-time Multiple-Input Multiple-Output CO-OFDM Reception

It is well known that single mode fibre can be represented as a two by two channel. The polarization diversity can be employed to increase spectral efficiency. This principle has been introduced into real-time signal processing. In Section 5.2, the MIMO OFDM specific algorithm--Jones matrix inversion is investigated for two polarization signals recovery. We demonstrate the first real-time CO-MIMO-OFDM reception at a data rate of 6.67 Gb/s by using 1.5-GSa/s sampling rate ADCs and polarization diversity processing algorithms. The optical fibre channel matrix is estimated by using 32 training sequences with odd ones filled with normal data while even ones are left blank. The polarization state is free running during measurement. The measured BER curves fit theoretical analysis. In Section 5.3, the principle of recirculation loop is discussed. This setup is used to achieve 600-km fibre transmission by circulating the optical OFDM signal 6 times in the loop. By employing a RFS and a recirculation loop, the 110-Gb/s multi-band CO-MIMO-OFDM reception experiment with 400-ps DGD is demonstrated. After 600-km SSMF transmission, the BER of each band is still below FEC threshold. The OSNR penalty of 400-ps DGD is negligible, which proves the robustness of PMD resistance for optical OFDM.

7.4 I/Q Imbalance Compensation for CO-OFDM Systems

Direct-conversion architecture has the advantages of low cost, low power consumption and less bandwidth requirement for electrical components, but it suffers from analog domain impairments. Such impairments are caused by the imperfectness of optical I/Q modulators, balanced photo detectors and optical hybrids. Their effects have been modelled as I/Q imbalance. Some compensation algorithms have been proposed in the wireless domain while only a few applications in optical OFDM have been reported. In Chapter 6, we apply the proposed compensation algorithms in Section 3.5 for both off-line and real-time I/Q imbalance calibration. In Section 6.2, the transmitter and receiver I/Q imbalance compensations are conducted respectively. The hybrid domain compensation scheme achieves 1 dB OSNR improvement at the BER of $1x10^{-3}$ in the 10.8-Gb/s off-line signal processing experiment. In Section 6.3, the real-time calibration scheme shows a most significant improvement in the transmitter I/Q timing mismatch compensation experiment. The BER data are decreased from near 1×10^{-2} to around 8×10^{-4} at 15-dB OSNR when the intentional timing mismatch is set to 60 ps.

Bibliography

[1] Cisco Inc., "Cisco Visual Networking Index: Forecast and Methodology, 2009-2014," information available at http://www.cisco.com/en/US/solutions/ collateral/ns341/ns525/ns537/ns705/ns827/white_paper_c11-481360_ns827_Networking_Solutions_White_Paper.html.

[2] H. Taub et al., Principles of Communication Systems, 2nd Edition, McGraw-Hill, 1986.

[3] T. Kimura, "Coherent optical fibre transmission," Journal of Lightwave Technology, Vol. 5, No. 4, pp. 414-428, 1987.

[4] R. E. Wagner et al., "Heterodyne lightwave systems: Moving towards commercial use," IEEE Lightwave Communication Syststem Magazine, Vol. 1, No. 4, pp. 28-35, 1990.

[5] G. P. Agrawal, Fibre-Optic Communication Systems, 3rd edition. John Wiley & Sons, 2002.

[6] R. Talbot, "Infinera Announces Coherent 100G DWDM System for 2012 at Cost of 400G PIC Program," Information available at http://www.currentanalysis.com/h/2010/Infinera-coherent-100Gbps.asp

[7] A. Sano et al., "69.1-Tb/s (432×171-Gb/s) C- and Extended L-Band Transmission over 240 Km Using PDM-16-QAM Modulation and Digital Coherent Detection," in proceedings of Optical Fibre Communication Conference and Exposition and The National Fibre Optic Engineers Conference 2010, paper PDPB7.

[8] J. X. Cai et al., "112x112 Gb/s Transmission over 9,360 km with Channel Spacing Set to the Baud Rate (360% Spectral Efficiency)," in proceedings of

European Conference and Exhibition on Optical Communication 2010, paper PD2.1.

[9] S. Hara et al., Multicarrier Techniques for 4G Mobile Communications, Artech House, 2003.

[10] R. W. Chang, "Orthogonal Frequency Division Multiplexing", U.S. Patent 3,488,445, filed 1966, 1970.

[11] S. B. Weinstein et al, "Data Transmission by Frequency-Division Multiplexing Using the Discrete Fourier Transform," IEEE Transactions on Communication Technology, Vol. COM-19, No.5, pp.628-634, 1971.

[12] B. Hirosaki, "An Orthogonal-Multiplexed QAM System Using the Discrete Fourier Transform," IEEE Transactions on Communication Technology, Vol. COM-29, No.7, pp.982-989, 1981.

[13] W. Shieh et al., "Coherent optical orthogonal frequency division multiplexing" Electronics Letters, Vol. 42, pp. 587-589, 2006.

[14] L. Hanzo et al., Quadrature Amplitude Modulation: from basics to adaptive trellis-coded, turbo-equalised and space-time coded OFDM, CDMA and MC-CDMA systems, John Wiley & Sons, 2004.

[15] R. Dischler et al., "Transmission of 1.2 Tb/s continuous waveband PDM-OFDM signal with spectral efficiency of 3.3 bit/s/Hz over 400 km of SSMF," in proceedings of Optical Fibre Communication Conference and Exposition and The National Fibre Optic Engineers Conference 2009, paper PDPC2.

[16] X. Liu et al., "Efficient Digital Coherent Detection of A 1.2-Tb/s 24-Carrier No-Guard-Interval CO-OFDM Signal by Simultaneously Detecting Multiple Carriers Per Sampling," in proceedings of Optical Fibre Communication Conference and Exposition and The National Fibre Optic Engineers Conference 2010, paper OWO2.

[17] P. Schvan, et al, “A 24GS/s 6b ADC in 90nm CMOS,” in proceedings of IEEE International Solid-State Circuits Conference 2008, paper 30.3.

[18] Micram Inc, “VEGA ADC 30 Key Data,” information available at http://www.micram.com/index.php/products/vega?start=2.

[19] Texas Instruments Incorporated, “TMS320C66x DSP generation of devices,” information available at http://focus.ti.com/lit/an/sprt580/sprt580.pdf.

[20] Advanced Micro Devices, Inc., “AMD FireStream™ 9270 GPU Compute Accelerator,” Information available at http://www.amd.com/us/products/workstation/firestream/firestream-9270/pages/firestream-9270.aspx

[21] Altera Inc., “Stratix V FPGAs: Built for Bandwidth,” information available at http://www.altera.com/literature/br/br-stratix-v-hardcopy-v.pdf.

[22] H. Sun et al., “Real-time measurements of a 40 Gb/s coherent system,” Optics Express, Vol. 16, pp. 873-879, 2008.

[23] S. J. Savory et al., “Electronic compensation of chromatic dispersion using a digital coherent receiver,” Optics Express, Vol. 15, pp. 2120-2126, 2007.

[24] W. Shieh et al., "107 Gb/s coherent optical OFDM transmission over 1000-km SSMF Fibre using orthogonal band multiplexing," Optics Express, Vol. 16, pp. 6378-6386, 2008.

[25] Q. Yang et al., “Real-Time Coherent Optical OFDM Receiver at 2.5-GS/s for Receiving a 54-Gb/s Multi-band Signal,” in proceedings of Optical Fibre Communication Conference and Exposition and The National Fibre Optic Engineers Conference 2009, paper PDPC5.

[26] B. Razavi, RF Microelectronics, Prentice-Hall, 1998.

[27] D. Tandur et al., “Joint adaptive compensation of transmitter and receiver IQ imbalance under carrier frequency offset in OFDM-based systems,” IEEE Transactions on Signal Processing, Vol. 55, No. 11, pp. 5246-5252, 2007.

[28] H. Lin et al., “Hybrid domain compensation for analog impairments in OFDM systems,” in proceedings of IEEE Global Telecommunications Conference 2008.

[29] T. C. W. Schenk et al., “Estimation and compensation of frequency selective TX/RX IQ imbalance in MIMO OFDM systems,” In proceedings of International Conference on Communications 2006, pp. 251-256, 2006.

[30] Y. Ma et al., "Bandwidth-Efficient 21.4 Gb/s Coherent Optical 2×2 MIMO OFDM Transmission," in proceedings of Optical Fibre Communication Conference and Exposition and The National Fibre Optic Engineers Conference 2008, JWA59.

[31] W. R. Peng et al., "Compensation for I/Q Imbalances and Bias Deviation of the Mach–Zehnder Modulators in Direct-Detected Optical OFDM Systems," IEEE Photonics Technology Letters, Vol. 21, No. 2, pp. 103-105, 2009.

[32] A. Al Amin et al., "A hybrid IQ imbalance compensation method for optical OFDM transmission," Optics Express, Vol. 18, pp. 4859-4866, 2010.

[33] T. Pollet et al., “BER sensitivity of OFDM systems to carrier frequency offset and wiener phase noise,” IEEE Transactions on Communications, Vol.43, No. 2/3/4, pp. 191-193, 1995.

[34] J. Armstrong, "OFDM for Optical Communications", Journal of Lightwave Technology, Vol. 27, pp. 189-204, 2009.

[35] J. A. C. Bingham, “Multicarrier modulation for data transmission: An idea whose time has come,” IEEE Communications Magazine, Vol. 28, pp. 5-14, 1990.

[36] R. van Nee et al., OFDM for Wireless Multimedia Communications. Artech House, 2000.

[37] W. Y. Zou et al., "COFDM: An overview," IEEE Transactions on Broadcasting, Vol. 41, pp. 1-8, 1995.

[38] J. H. Stott, "The how and why of COFDM," EBU Technical Review, pp. 43-50, 1998.

[39] R. W. Chang, "Synthesis of band-limited orthogonal signals for multi-channel data transmission," Bell Labs Technical Journal, No. 45, pp. 1775-1796, 1966.

[40] R. W. Chang et al., "A theoretical study of performance of an orthogonal multiplexing data transmission scheme," IEEE Transactions on Communication Technology, Vol. 16, pp. 529-540, 1968.

[41] B. R. Saltzberg, "Performance of an efficient parallel data transmission system," IEEE Transactions on Communication Technology, Vol. 15, pp. 805-811, 1967.

[42] S. B. Weinstein et al., "Data transmission by frequency-division multiplexing using the discrete Fourier transform," IEEE Transactions on Communication Technology, Vol. 19, pp. 628-634, 1971.

[43] L. J. Cimini, Jr., "Analysis and simulation of a digital mobile channel using orthogonal frequency division multiplexing," IEEE Transactions on Communications, vol. CM-33, pp. 665-675, 1985.

[44] A. J. Lowery et al., "Orthogonal frequency division multiplexing for adaptive dispersion compensation in long haul WDM systems," in proceedings of Optical Fibre Communication Conference and Exposition and The National Fibre Optic Engineers Conference 2006, paper PDP39.

[45] I. B. Djordjevic et al., "Orthogonal frequency division multiplexing for high-speed optical transmission," Optics Express, Vol. 14, pp. 3767-3775, 2006.

[46] W. Shieh et al., "107 Gb/s coherent optical OFDM transmission over 1000-km SSMF Fibre using orthogonal band multiplexing," Optics Express, Vol. 16, pp. 6378-6386, 2008.

[47] S. L. Jansen et al., "10x121.9-Gb/s PDM-OFDM transmission with 2-b/s/Hz spectral efficiency over 1000 km of SSMF," in proceedings of Optical Fibre Communication Conference and Exposition and The National Fibre Optic Engineers Conference 2008, paper PDP2.

[48] E. Yamada et al., "1Tb/s (111Gb/s/ch × 10ch) no-guard-interval CO-OFDM transmission over 2100 km DSF," in proceedings of Opto-Electronics Communications Conference/Australian Conference on Optical Fibre Technology 2008, paper PDP6.

[49] Y. Ma et al., "1-Tb/s per Channel Coherent Optical OFDM Transmission with Subwavelength Bandwidth Access," in proceedings of Optical Fibre Communication Conference 2009, paper PDPC1.

[50] R. Dischler et al., "Transmission of 1.2 Tb/s Continuous Waveband PDM-OFDM-FDM Signal with Spectral Efficiency of 3.3 bit/s/Hz over 400 km of SSMF," in proceedings of Optical Fibre Communication Conference and Exposition and The National Fibre Optic Engineers Conference 2009, paper PDPC2.

[51] S. Chen et al., "Real-time Reception of Multi-gigabit Coherent Optical MIMO-OFDM Signal," Journal of Lightwave Technology, Vol. 27, pp. 3699-3704, 2009.

[52] Y. Benlachtar et al., "Generation of optical OFDM signals using 21.4 GS/s real time digital signal processing," Optics Express, Vol. 17, pp. 17658-17668, 2009.

[53] F. Buchali et al., "Realisation of a real-time 12.1 Gb/s optical OFDM transmitter and its application in a 109 Gb/s transmission system with coherent reception,"

in proceedings of European Conference and Exhibition on Optical Communication 2009, paper PDP2.1.

[54] X. Q. Jin et al., "Real-time transmission of 3Gb/s 16-QAM encoded optical OFDM signals over 75km SMFs with negative power penalties," Optics Express, Vol. 17, pp. 14574-14585, 2009.

[55] A. J. Lowery et al., "Performance of optical OFDM in ultralong-haul WDM lightwave systems," Journal of Lightwave Technology, Vol. 25, pp. 131-138, 2007.

[56] D. F. Hewitt, "Orthogonal Frequency Division Multiplexing using Baseband Optical Single Sideband for Simpler Adaptive Dispersion Compensation," in proceedings of Optical Fibre Communication Conference and Exposition and The National Fibre Optic Engineers Conference 2007, paper OME7.

[57] J. Ning et al., "Baseband OFDM optical single-sideband transmission with parallel optical SSB modulation for direct detection," in proceedings of IEEE International Conference on Network Infrastructure and Digital Content 2009.

[58] W. Peng et al., "Experimental Demonstration of a Coherently Modulated and Directly Detected Optical OFDM System Using an RF-Tone Insertion," in proceedings of Optical Fibre Communication Conference and Exposition and The National Fibre Optic Engineers Conference 2008, paper OMU2.

[59] W. Peng et al., "Experimental Demonstration of 340 km SSMF Transmission Using a Virtual Single Sideband OFDM Signal that Employs Carrier Suppressed and Iterative Detection Techniques," in proceedings of Optical Fibre Communication Conference and Exposition and The National Fibre Optic Engineers Conference 2008, paper OMU1.

[60] W. Shieh et al., "Transmission experiment of multi-gigabit coherent optical OFDM systems over 1000km SSMF fibre," IEE Electronics Letters, Vol. 43, pp. 183-185, 2007.

[61] S. L. Jansen et al., "20-Gb/s OFDM transmission over 4,160-km SSMF enabled by RF-Pilot tone phase noise compensation," in proceedings of Optical Fibre Communication Conference and Exposition and The National Fibre Optic Engineers Conference 2007, paper PDP15.

[62] L. Xu et al., "Coherent Optical OFDM Systems Using Self Optical Carrier Extraction," in proceedings of Optical Fibre Communication Conference and Exposition and The National Fibre Optic Engineers Conference 2008, paper OMU4.

[63] E. Yamada et al., "1Tb/s (111Gb/s/ch × 10ch) no-guard-interval CO-OFDM transmission over 2100 km DSF," in proceedings of Opto-Electronics Communications Conference/Australian Conference on Optical Fibre Technology 2008, paper PDP6.

[64] X. Liu et al., "Transmission of a 448-Gb/s reduced-guard-interval CO-OFDM signal with a 60-GHz optical bandwidth over 2000 km of ULAF and five 80-GHz-Grid ROADMs," in proceedings of Optical Fibre Communication Conference and Exposition and The National Fibre Optic Engineers Conference 2010, paper OWO2.

[65] H. Louchet et al., "Novel Scheme for High-Bit-Rate Coherent-OFDM Transmission without PLL," in proceedings of European Conference and Exhibition on Optical Communication 2007, paper P087.

[66] S. Adhikari et al., "Experimental Investigation of Self Coherent Optical OFDM Systems Using Fabry-Perot Filters for Carrier Extraction," in proceedings of European Conference and Exhibition on Optical Communication 2010, paper Tu.4.A.1.

[67] P. Poggiolini et al., "Evaluation of the computational effort for chromatic dispersion compensation in coherent optical PM-OFDM and PM-QAM systems," Optics Express, Vol. 17, pp. 1385-1403, 2009.

[68] Altera Corp., “Altera’s 28-nm, Power-Efficient Transceivers,” brochure available at http://www.altera.com/literature/po/ss-28nm-transceivers.pdf

[69] P. Watts et al., “An FPGA-Based Optical Transmitter Design Using Real-Time DSP for Advanced Signal Formats and Electronic Predistortion,” Journal of Lightwave Technology, Vol. 25, pp. 3089-3099, 2007.

[70] T. Pfau et al., “PDL-Tolerant Real-time Polarization-Multiplexed QPSK Transmission with Digital Coherent Polarization Diversity Receiver,” In proceedings of Lasers & Electro-Optics Society Summer Topical Meetings 2007, paper MA3.3.

[71] K. Fukuchi et al., “112Gb/s Optical Transponder with PM-QPSK and Coherent Detection Employing Parallel FPGA-based Real-Time Digital Signal Processing, FEC and 100GbE Ethernet Interface,” in proceedings of European Conference and Exhibition on Optical Communication 2010, paper Tu.5.A.2.

[72] C. Weber et al., “Electronic precompensation of intrachannel nonlinearities at 40 Gb/s,” IEEE Photonics Technology Letters, Vol. 18, No. 16, pp. 1759-1761, 2006.

[73] F. Buchal et al., “Realisation of a real-time 12.1 Gb/s optical OFDM transmitter and its application in a 109 Gb/s transmission system with coherent reception,” in proceedings of European Conference and Exhibition on Optical Communication 2009, paper PD2.1.

[74] R. I. Killey et al., “FPGA-Based Optical Transmitters for Electronic Predistortion and Advanced Signal Format Generation,” in proceedings of Lasers & Electro-Optics Society 2009, paper TuI4.

[75] S. Chen et al., “Multi-gigabit Real-time Coherent Optical OFDM Receiver,” in proceedings of Optical Fibre Communication Conference and Exposition and The National Fibre Optic Engineers Conference 2009, paper OTuO4.

[76] N. Kaneda et al., “Realizing Real-Time Implementation of Coherent Optical OFDM Receiver with FPGAs,” in proceedings of European Conference and Exhibition on Optical Communication 2009, paper 5.4.4.

[77] X. Q. Jin et al., “Real-Time 3Gb/s 16QAM-Encoded Optical OFDM Transmission over 75km MetroCor SMFs with Negative Power Penalties,” in proceedings of Opto-Electronics and Communications Conference 2009, paper ThPD8.

[78] D. Qiang et al., “41.25 Gb/s Real-Time OFDM Receiver for Variable Rate WDM-OFDMA-PON Transmission,” in proceedings of Optical Fibre Communication Conference and Exposition and The National Fibre Optic Engineers Conference 2010, paper PDPD9.

[79] C. Tang et al., “200Gs/s Real-time Optical-Sampling-based Orthogonal Frequency Division Multiplexing System,” in proceedings of Optical Fibre Communication Conference and Exposition and The National Fibre Optic Engineers Conference 2010, paper OWO5.

[80] D. Hillerkuss et al., “Novel Optical Fast Fourier Transform Scheme Enabling Real-Time OFDM Processing at 392 Gbit/s and Beyond,” in proceedings of Optical Fibre Communication Conference and Exposition and The National Fibre Optic Engineers Conference 2010, paper OWW3.

[81] S. Ma et al., “Estimation and Compensation of Frequency-dependent I/Q Imbalances in OFDM Systems over Fading Channels,” in proceedings of the 5th International Conference on Wireless Communications, Networking and Mobile Computing 2009.

[82] L. Lanante et al., “A Simple Estimation Scheme for Joint Estimation of Carrier Frequency Offset and I/Q Imbalance,” in proceedings of IEEE Vehicular Technology Conference 2009.

[83] W. R. Peng et al., “Compensation for I/Q Imbalances and Bias Deviation of the Mach–Zehnder Modulators in Direct-Detected Optical OFDM Systems,” IEEE Photonics Technology Letters, Vol. 21, No. 2, 2009.

[84] Y. Ma et al., “Bandwidth-Efficient 21.4 Gb/s Coherent Optical 2×2 MIMO OFDM Transmission,” in proceedings of Optical Fibre Communication Conference and Exposition and The National Fibre Optic Engineers Conference 2008, JWA 59.

[85] A. Al Amin et al., "A hybrid IQ imbalance compensation method for optical OFDM transmission," Optics Express, Vol. 18, pp. 4859-4866, 2010.

[86] S. Chen et al., “Hybrid Frequency-Time Domain Tx and Rx IQ Imbalance Compensation for Coherent Optical OFDM Transmission,” in proceedings of Asia Communications and Photonics Conference and Exhibition 2010, paper FO6.

[87] M. Windisch et al., “Standard-Independent I/Q Imbalance Compensation in OFDM Direct-Conversion Receivers,” 9th International OFDM Workshop, 2004.

[88] L. Kazovsky, “Multichannel coherent optical communications systems,” Journal of Lightwave Technology, Vol. 5, pp. 1095- 1102, 1987.

[89] T. Okoshi, “Heterodyne and Coherent Optical Fibre Communications: Recent Progress,” IEEE Transactions on Microwave Theory and Techniques, Vol. 82, pp. 1138-1149, 1982.

[90] D. S. Ly-Gagnon et al., “Coherent detection of optical quadrature phase-shift keying signals with carrier phase estimation,” Journal of Lightwave Technology, Vol. 24, pp. 12-21, 2006.

[91] S. J. Savory et al., “Electronic compensation of chromatic dispersion using a digital coherent receiver,” Optics Express, Vol. 15, pp. 2120-2126, 2007.

[92] C. Laperle et al., “Wavelength division multiplexing (WDM) and Polarization Mode Dispersion (PMD) performance of a coherent 40Gbit/s dual-polarization quadrature phase shift keying (DP-QPSK) transceiver,” in proceedings of Optical Fibre Communication Conference and Exposition and The National Fibre Optic Engineers Conference 2007, paper PDP16.

[93] G. Charlet et al., “Efficient mitigation of Fibre impairments in an ultra-long haul transmission of 40Gbit/s Polarization-multiplexed data, by digital processing in a coherent receiver,” in proceedings of Optical Fibre Communication Conference and Exposition and The National Fibre Optic Engineers Conference 2007, paper PDP17.

[94] W. Shieh et al., "Theoretical and experimental study on PMD-supported transmission using polarization diversity in coherent optical OFDM systems," Optics Express, Vol. 15, pp. 9936-9947, 2007.

[95] S. L. Jansen et al., “16×52.5-Gb/s, 50-GHz spaced, POLMUX-CO-OFDM transmission over 4,160 km of SSMF enabled by MIMO processing KDDI R&D Laboratories,” in proceedings of European Conference on Optical Communications 2007, paper PD1.3.

[96] L. Litwin et al., “The principles of OFDM,” RF Design, pp. 30-48, 2001.

[97] S. B. Weinsten et al., “Data transmission by frequency-division multiplexing using the discrete Fourier transform,” IEEE Transactions on Communications, Vol. 19, pp. 628-634, 1971.

[98] A.W.M. van den Enden et al., Discrete-time signal processing: an introduction. Prentice Hall, 1989.

[99] Y. Tang et al., "107 Gb/s CO-OFDM Transmission with Inline Chromatic Dispersion Compensation," in proceedings of Optical Fibre Communication Conference and Exposition and The National Fibre Optic Engineers Conference 2007, paper OWW3.

[100] N. Gisin et al., “Combined effects of polarization mode dispersion and polarization dependent losses in optical Fibres,” Optics Communications, Vol. 142, pp. 119-125, 1997.

[101] T. Schenk et al., RF Imperfections in High-rate Wireless Systems: impact and digital compensation, Springer, Chapter 5, pp. 139-183, 2008.

[102] M. Valkama et al., “Compensation of frequency-selective I/Q imbalances in wideband receivers: Models and algorithms,” in proceedings of Third IEEE Signal Processing Workshop Signal Processing Advanced Wireless Communications, pp. 42-45, 2001.

[103] T. M. Schmidl et al., “Robust frequency and timing synchronization for OFDM,” IEEE Transactions on Communications, Vol. 45, pp. 1613-1621, 1997.

[104] H. Minn et al., “A robust timing and frequency synchronization for OFDM systems,” IEEE Transactions on Wireless Communications, Vol. 2, pp. 822-839, 2003.

[105] W. Shieh et al., "Coherent optical OFDM: has its time come? [Invited]," Journal of Optical Networking, Vol. 7, pp. 234-255, 2008.

[106] R. P. Giddings et al., “Experimental demonstration of a record high 11.25Gb/s real-time optical OFDM transceiver supporting 25km SMF end-to-end transmission in simple IMDD systems,” Optics Express, Vol 18, pp. 5541-5555, 2010.

[107] S. Chen et al., “Demonstration of 12.1-Gb/s Single-band Real-time Coherent Optical OFDM Reception,” in proceedings of OptoElectronics and Communications Conference, paper 8B4-2.

[108] E2V Technologies, EV8AQ160-EB Evaluation Board User Guide, information available at http://www.e2v.com/assets/media/files/documents/broadband-data-converters/doc0834E.pdf.

[109] E2V Technologies, EV8AQ160 Quad ADC Datasheet, information available at http://www.e2v.com/assets/media/files/documents/broadband-data-converters/doc0846I.pdf.

[110] J. Li et al., “Theoretical and experimental study on generation of stable and high-quality multi-carrier source based on re-circulating frequency shifter used for Tb/s optical transmission,” Optics Express, Vol. 19, pp. 848-860, 2011.

[111] T. Kawanishi et al., “Optical frequency comb generator using optical Fibre loops with single-sideband modulation,” IEICE Electronics Express, Vol. 1, No. 8, pp. 217-221, 2004.

[112] X. Yi et al., “Phase Noise Effects on High Spectral Efficiency Coherent Optical OFDM Transmission,” Journal of Lightwave Technology, Vol. 26, pp. 1309-1316, 2008.

[113] Q. Yu et. al., “Loop-Synchronous Polarization Scrambling Technique for Simulating Polarization Effects Using Recirculating Fibre Loops,” Journal of Lightwave Technology, Vol. 21, No. 7, pp. 1593-1600, 2003.

[114] S. Chen et al., "Real-Time Multi-Gigabit Receiver for Coherent Optical MIMO-OFDM Signals," Journal of Lightwave Technology, Vol. 27, pp. 3699-3704, 2009.

[115] B. Razavi, RF Microelectronics. Prentice Hall, 1998.

Appendix

Acronyms	Description
ADC	Analog-to-Digital Converters
AND	AND logic gate
ASE	Amplified Spontaneous Emission
ASIC	Application-Specific Integrated Circuit
AWG	Arbitrary Waveform Generator
B2B	Back-to-Back
BER	Bit Error Ratio
BPSK	Binary Phase-Shift Keying
CD	Chromatic Dispersion
CFO	Carrier Frequency Offset
CFP	A hot-pluggable optical transceiver interface to enable 40-Gb/s and 100-Gb/s applications
CLB	Configurable Logic Block
CMA	Constant Modulus Algorithm
CMOS	Complementary Metal Oxide Semiconductor
CO-FODM	Coherent Optical OFDM
CP	Cyclic Prefix
CPE	Common Phase error
CR	Compensation Ratio
CSR	Carrier-to-Signal Ratio
CW	Continuous Wave
DAB	Digital Audio Broadcasting
DAC	Digital-to-Analog Converter
DBPSK	Differential Binary Phase Shift Keying
DC	Direct Current

DDO-OFDM	Direct-Detection Optical OFDM
DEMUX	De-multiplexer
DFB	Distributed Feed-Back
DFT	Discrete Fourier Transform
DGD	Differential Group Delay
DI	Delay Interferometer
DML	Directly Modulated DFB Laser
DPSK	Differential Phase-Shift Keying
DQPSK	Differential Quadrature Phase-Shift Keying
DSO	Digital Storage Oscilloscope
DSP	Digital Signal Processor
DVB-T	Digital Video Broadcasting-Terrestrial
DWDM	Dense Wavelength Division Multiplexed
EAM	Electro-Absorption Modulator
EDA	Electronic Design Automation
EDC	Electronic Dispersion Compensation
EDFA	Erbium Doped Fibre Amplifier
E/O	Electro-Optic
EPD	Electronic Pre-Distortion
EVM	Error Vector Magnitude
FBG	Fibre Bragg Grating
FDM	Frequency-division multiplexing
FEC	Forward Error Correction
FFT	Fast Fourier Transform
FIR	Finite Impulse Response
FPGA	Field-Programmable Gate Array
GI	Guard Interval
HDL	Hardware Description Language
I	In-phase

IC	Integrated Circuit
ICI	Inter-Carrier Interference
IDFT	Inverse Discrete Fourier Transform
IF	Intermediate Frequency
IFFT	Inverse Fast Fourier Transform
IM	Intensity Modulators
IM/DD	Intensity Modulation/ Direct Detection
IMOD	Intensity Modulator
I/O	Input/Output
IP	Internet Protocol
I/Q	In-phase/Quadrature
ISI	Inter-Symbol Interference
ITU	International Telecommunication Union
JTAG	Joint Test Action Group. It is the common name of the IEEE 1149.1 Standard Test Access Port and Boundary-Scan Architecture
km	Kilometer
LAN	Local Area Networks
LD	Laser Diode
LiNbO3	Lithium-Niobate
LO	Local Oscillator
LPF	Low Pass Filter
LUT	Look-Up Table
LVDS	Low-voltage Differential Signalling
MCM	Multiple-Carrier Techniques Modulation
MIMO	Multiple Input Multiple Output
MOD	Modulator
MSE	Mean Square Error
MUX	Multiplexer

MZM	Mach-Zehnder Modulator
NGI	No-Guard Interval
OA	Optical Amplifier
OBM-OFDM	Orthogonal-Band-Multiplexed OFDM
OBPF	Optical Band Pass Filters
ODI	Optical Delay Interformeters
O/E	Optical-Electrical
OFDM	Orthogonal Frequency-Division Multiplexing
O-OFDM	Optical OFDM
OOK	On-Off Keying
OPLL	Optical Phase Locked Loop
OSNR	Optical Signal Noise Ratio
OTDM	Optical Time Division Multiplexing
OTR	Optical to Radio Frequency
PAPR	Peak to Average Power Ratio
PBC	Polarization Beam Combiner
PBS	Polarization Splitter
PD	Photo Diode/Photo Detector
PDL	Polarization-Dependent loss
PMD	Polarization Mode Dispersion
PRBS	Pseudo-Random Binary Sequence
PSK	Phase Shift Keying
Q	Quadrature
QAM	Quadrature Amplitude Modulation
QPSK	Quadrature Phase-Shift Keying
RF	Radio Frequency
RFS	Recirculating Frequency Shifter
RFT-OFDM	RF Tone-assisted OFDM
RGI-OFDM	Reduced-Guard-Interval OFDM

RMS	Root-Mean-Square
ROM	Read-only Memory
RTO	RF-to-Optical
Rx	Receiver
RZ	Return-to-Zero
SAW	Surface Acoustic Wave
SC-FDE	Single Carrier-Frequency Domain Equalization
SE	Single-End
SFDR	Spurious-Free Dynamic Range
SISO	Single-Input Single-Output
SMF	Single Mode Fibre
SNR	Signal to Noise Ratio
SPM	Self-Phase Modulation
SSB	Single Side Band Se Ratio
SSBI	Signal-Signal Beat Interference
SSMF	Standard Single Mode Fibre
TDM	Time Division Multiplexing
TDS	Time Domain-Sampling Scope
THD	Total Harmonic Distortion
TIA	Trans-Impedance Amplifier
TITO	Two Input two Output
TNR	Tone-to-Noise Ratio
TS	Training Sequence
Tx	Transmitter
VGA	Variable Gain Amplifier
VHDL	VHSIC Hardware Description Language
VSSB-OFDM	Virtual SSB-OFDM
WDM	Wavelength-Division Multiplexing
WiMax	Worldwide interoperability for

	Microwave Access
WLAN	Wireless Local Area Networks
XOR	XOR logic gate